VERLAG DER TECHNISCHEN UNIVERSITÄT GRAZ

Andreas Kvas

Estimation of High-Frequency Mass Variations from Satellite Data in near Real-Time

Implementation of a Technology Demonstrator for near Real-Time GRACE/GRACE-FO Gravity Field Solutions

GEOD 2

MONOGRAPHIC SERIES TU GRAZ
GEODESY

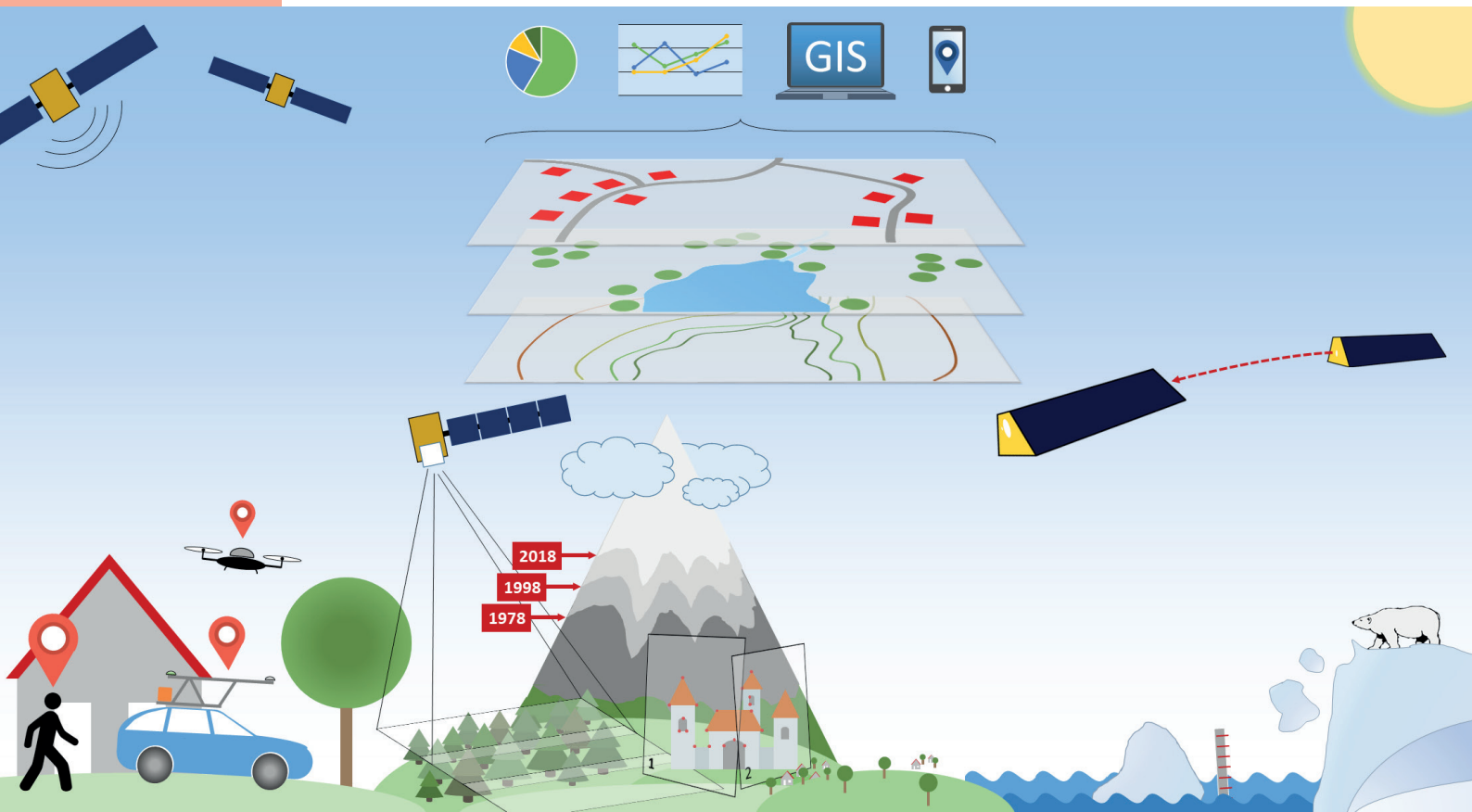

Andreas Kvas

Estimation of High-Frequency Mass Variations from Satellite Data in near Real-Time

Implementation of a Technology Demonstrator for near Real-Time GRACE/GRACE-FO Gravity Field Solutions

Monographic Series TU Graz

Geodesy

Monographic Series TU Graz

Geodesy Volume 2

Andreas Kvas

Estimation of High-Frequency Mass Variations from Satellite Data in near Real-Time

Implementation of a Technology Demonstrator for near Real-Time GRACE/GRACE-FO Gravity Field Solutions

---

This work is based on the dissertation *"Estimation of High-Frequency Mass Variations from Satellite Data in near Real-Time; Implementation of a Technology Demonstrator for near Real-Time GRACE/GRACE-FO Gravity Field Solutions"*, presented at Graz University of Technology; submitted to the Faculty of Mathematics, Physics and Geodesy in November 2019.

Supervision/Assessment:

Torsten Mayer-Gürr (Graz University of Technology)

Annette Eicker (HafenCity Universität Hamburg)

Cover photo	ifG, TU Graz
Cover layout	Verlag der Technischen Universität Graz
Print	DATAFORM Media Ges.m.b.H.

E-Book
ISBN 978-3-85125-771-7
DOI 10.3217/978-3-85125-771-7

Abstract

Earth's time variable gravity field provides invaluable insights into the changing nature of our planet. As it is a proxy to mass variations on Earth's surface, it reflects geophysical processes like continental hydrology, changes in the cryosphere or mass flux in the ocean. Dedicated satellite missions such as the NASA/DLR operated Gravity Recovery and Climate Experiment (GRACE), and its successor GRACE Follow-On (GRACE-FO) continuously monitor these temporal variations of the gravitational attraction with global coverage. Both missions provide monthly snapshots of Earth's gravity field with a latency of about two months. While these data sets have fundamentally improved the knowledge of the temporal evolution of the geophysical interactions which compose the global climate system, there are a variety of processes happening on sub-monthly time scales. For example, short-lived events such as floods, which occur on the time frame of hours to weeks, require low latency monitoring of high-frequency mass variations in order to be properly resolved.

This thesis provides the theoretical foundation, implementation, and a review of an operational test run of a near real-time (NRT) processing scheme for spaceborne gravity observations. Building on the already well established Kalman filter approach for GRACE/GRACE-FO data, a robust, fully autonomous tech demonstrator for daily gravity field solutions with a latency of one day based on GRACE quicklook (Q/L) data was implemented. Even though the operational test run of the NRT processing scheme coincided with the last months of the GRACE mission, where deteriorating health of the on-board instrumentation resulted in a challenging environment, high-quality gravity field solutions were obtained. This was confirmed by a reanalysis of the observation data, where post-processing techniques could be applied. Due to the unique nature of gravity observations which, in contrast to other remote sensing techniques, provide information about the whole water column including ground water, this complementary NRT data set has the potential to contribute to and improve flood forecasting in the future.

Contents

1. Introduction

Knowledge of Earth's time variable gravity field is key for understanding the state and change of our planet's dynamic system. Changes in the mass distribution on Earth's surface and in its interior, for example, caused by the melting of ice sheets or the continental water cycle, also change Earth's potential field. Many of these underlying geophysical - but also anthropogenic processes - play a key role in our global climate system and directly impact our everyday life. Observations of gravity field variations can provide insights into how these processes evolve and therefore provide benefits to society as a whole.

Satellite gravimetry is especially useful in this context as it provides a global picture of gravity field changes. In the last decades, dedicated satellite missions to observe Earth's gravity field, such as the Challenging Minisatellite Payload (CHAMP), Gravity field and steady-state Ocean Circulation Explorer (GOCE), Gravity Recovery and Climate Experiment (GRACE), and GRACE Follow-On (GRACE-FO) have been realized. Within this group GRACE and GRACE-FO hold a special status. Their unique measurement principle, which relies on highly accurate distance measurements between a leading and a trailing satellite, is especially sensitive to temporal variations in Earth's gravity field. After accumulating approximately one month of measurements, a global data coverage is reached. This is the prerequisite for a stable gravity field estimate with homogeneous accuracy. Since the launch of GRACE in 2002 and the launch of its successor GRACE-FO in 2018, a nearly continuous record of monthly gravity field snapshots has been obtained. This provides an invaluable data set for Earth and climate research and allows for consistent long-term investigations of changes on our planet.

Certain geophysical processes however occur on time scales much shorter than a single month. For example, floods are highly dynamic events, which may only take hours to days to develop and drain. To observe such events, the monthly sampling of standard GRACE/GRACE-FO solutions is much too coarse. An obvious way to overcome this deficiency is to reduce the accumulation period from one month to, for example, one day. However, with such a drastically reduced data coverage, a globally homogeneous gravity field estimate can no longer be obtained from the satellite observations alone. Thus, tailored processing approaches are required in order to mitigate the drawback of the increased sampling rate.

To fully exploit the benefit of satellite gravimetry for short-lived events such as floods, (near) real-time (NRT) observations are required. This allows for the monitoring and potentially the prediction of these extreme events rather than confirmation and evaluation after-the-fact. The transition towards NRT is therefore not only useful for the scientific community but also provides societal benefits.

1.1. Earth's time variable gravity field

Changes in Earth's potential are caused by a variety of processes happening on all spatial and temporal time scales. The following paragraphs give a rough overview over the most prominent signals which cause changes in surface mass. While these processes are listed here as individual geophysical subsystems, in reality most of them interconnected, for example, through the global water cycle. Satellite gravimetry does not discriminate between different sources of mass change, thus it is a prime candidate for the integrated monitoring of the dynamic system Earth.

Tidal effects The primary cause of mass redistribution in the Earth system are tidal effects of sun, moon and to a lesser extent of the other bodies in the solar system. The gravitational attraction of these celestial bodies causes a deformation of the solid earth of a few decimeters and redistribution of water masses in the ocean. In coastal areas, localized sea level variations of a few meters are not uncommon. Next to the solid Earth and the ocean, the atmosphere also responds to tidal effects. Atmospheric tides are however not only caused by the gravitational pull of the celestial bodies but also through large scale latent heat release. Changes in the gravitational field are also induced by the motion of Earth's rotational axis with respect to its solid body. This effect called polar motion, causes mass flux due to centrifugal forces acting on both the solid Earth and the water masses of the ocean. While it is not strictly a direct consequence of tidal effects, it is often referred to as "pole tide" (Carton & Wahr, 1986; Petit & Luzum, 2010; Wahr, Nerem, & Bettadpur, 2015).

Continental hydrology The interplay of precipitation, evapotranspiration, infiltration, subsurface flow, and runoff of water is another major driver of mass redistribution in the Earth system. Seasonal variations in groundwater level, secular changes during drought periods but also short lived events such as major floods have already been studied through the resulting potential changes (e.g., Gouweleeuw et al., 2018). Furthermore, anthropogenic variations in water storage as a result of excessive irrigation or reservoirs can also be detected through satellite gravimetry.

Non-tidal ocean mass flux Next to tidal effects, the ocean also exhibits non-tidal mass variations caused by eddy generation in the confluence zones, through the influx of freshwater from continental runoff, or through mass transport caused by major currents such as the gulf stream. Apart from these regional mass fluxes, the global mass change of the ocean is also of utmost importance, as it provides a way to infer sea level rise.

Cryospheric mass variations Variations in the cryosphere, either through snow accumulation, melting of ice sheets or glacier systems result in primarily seasonal and secular variations. Prominent signals are mass loss in the ice sheets of Greenland and Antarctica, and glacier systems in, e.g., Iceland, Svalbard and Alaska (e.g., Wouters, Gardner, & Moholdt, 2019).

Atmospheric mass flux Changes in the gravitational potential are also caused by density changes in the atmosphere through winds, temperature variations or varying specific humidity.

Solid earth processes Mass changes in the solid earth are primarily caused by glacial isostatic adjustment (GIA) and seismic activities. GIA describes the adjustment process of the earth to an equilibrium state as a result of retreating polar and continental ice sheets after the last ice age. The reduced load causes the crust to rebound, thus allowing mantle material to flow back under previously glaciated areas, resulting in a regional density change. Larger GIA signals can be observed in Antarctica, Canada, Fennoscandia and Greenland. Next to the secular GIA process, mass changes occur during major earthquakes. These co-seismic events have already been studied using satellite gravimetry (Han, Jekeli, & Shum, 2004; Panet, Bonvalot, Narteau, Remy, & Lemoine, 2018) and can be extremely well resolved when long time series of observation data is available (Kvas, Brockmann, et al., 2019). Earthquakes are typically followed by a post-seismic relaxation phase, where the affected regions exhibit a continuing mass change on the time scales of months to years.

The gravitational potential in the Earth's exterior is given through Newton's law of universal gravitation, which states that two mass particles attract each other with a force directly proportional to the product of their mass and inversely proportional to the square of their distance along the line intersecting the particles. A different interpretation of this statement is that a mass particle m_Q at position $\mathbf{r}_Q$ creates a vector field $\mathbf{g}(\mathbf{r})$, with

$$\mathbf{g}(\mathbf{r}) = -Gm_Q \frac{\mathbf{r} - \mathbf{r}_Q}{\|\mathbf{r} - \mathbf{r}_Q\|^3}, \tag{1.1}$$

where G is the gravitational constant, which represents the gravitational acceleration generated by this point mass. If the density distribution of a solid body can be described through a continuous function $\rho(\mathbf{r}_Q, t)$, the gravitational acceleration of the whole body can be obtained through the superposition principle by integrating over the body's volume Σ:

$$\mathbf{g}(\mathbf{r}, t) = -G \iiint_\Sigma \frac{\mathbf{r} - \mathbf{r}_Q}{\|\mathbf{r} - \mathbf{r}_Q\|^3} \, \rho(\mathbf{r}_Q, t) \, d\Sigma. \tag{1.2}$$

In (1.2), the time dependency of the gravitational acceleration due to changes in the density distribution of the body is explicitly added. Due to this gravitational field being conservative, there consequently exists a potential field

$$V(\mathbf{r}, t) = G \iiint_\Sigma \frac{\rho(\mathbf{r}_Q, t)}{\|\mathbf{r} - \mathbf{r}_Q\|} \, d\Sigma, \tag{1.3}$$

which satisfies $\mathbf{g}(\mathbf{r}, t) = \nabla V(\mathbf{r}, t)$. In the body's exterior, this gravitational potential can be expanded into a series of spherical harmonics (e.g., Heiskanen & Moritz, 1967). For this representation it is convenient to introduce spherical coordinates, which consist of the radius r, the spherical colatitude ϑ, and the longitude λ. They are connected to the position vector $\mathbf{r}$ through $\mathbf{r} = r \cdot [\sin\vartheta\cos\lambda, \sin\vartheta\sin\lambda, \cos\vartheta]^T$. The potential in terms of spherical harmonics is then given by

$$V(\mathbf{r}, t) = \frac{GM}{R} \sum_{n=0}^{\infty} \left(\frac{R}{r}\right)^{n+1} \sum_{m=-n}^{n} a_{nm}(t) Y_{nm}(\mathbf{r}), \tag{1.4}$$

where M is the Earth's mass, R is the mean equatorial radius, $a_{nm}(t)$ are time variable potential coefficients, and Y_{nm} are surface spherical harmonics. The surface spherical harmonics can be further decomposed into

$$Y_{nm}(\mathbf{r}) = P_{n|m|}(\cos\vartheta) \begin{cases} \cos m\lambda \text{ if } m \geq 0 \\ \sin m\lambda \text{ if } m < 0 \end{cases}, \tag{1.5}$$

where $P_{n|m|}$ is the associated Legendre function of degree n and order m. As in this thesis the temporal changes of the potential are of primary interest, typically only differences to a long-term mean field are considered. This can be reflected in (1.4) by substituting the spherical harmonic coefficients a_{nm} with $\Delta a_{nm}(t) = a_{nm}(t) - \bar{a}_{nm}$, where $\bar{a}_{nm}$ is the static or average part of the corresponding coefficient.

While (1.4) provides a strict mathematical description of Earth's time variable gravity field, it is often useful to provide more intuitive representations of potential changes. Especially for applications where potential changes are used to study geophysical processes, e.g., the global water cycle, it suggests itself to express these changes through the mass redistribution which cause them. The caveat with this approach is that, while a specific mass distribution has a unique potential field, the inverse does not hold. However, this problem can be overcome by reducing the solution space to a thin layer on Earth's surface. Given that short-term variations in Earth's gravity field are primarily governed by mass flux in the ocean, on Earth's surface, and in lower atmospheric layers, this assumption is certainly justified (Wahr, Molenaar, & Bryan, 1998). A widely used gravity field representation which is based on this thin layer approximation is equivalent water height (EWH), where

$$EWH(\mathbf{r}, t) = \frac{M}{4\pi R^2 \rho_w} \sum_{n=0}^{\infty} \frac{2n+1}{1+k'_n} \sum_{m=-n}^{n} \Delta a_{nm}(t) Y_{nm}(\mathbf{r}). \tag{1.6}$$

This quantity describes the amount and distribution of water with density ρ_w on Earth's surface which generates the potential change represented by $\Delta a_{nm}(t)$. In (1.6) the load Love numbers k'_n account for the indirect effect caused by the deformation of the solid Earth due to the mass of the water layer.

1.2. The satellite missions GRACE and GRACE Follow-On

The Gravity Recovery And Climate Experiment (GRACE, Tapley, Bettadpur, Watkins, & Reigber, 2004) satellite mission was in orbit for over 15 years and provided an invaluable data record for climate and Earth system sciences. Its primary data product was a time series of monthly gravity field snapshots - a proxy for mass distribution in the Earth system. These time-variable gravity field observations have been used to study a variety of geophysical processes, such as ice mass loss, continental hydrology, or sea level rise (e.g., Chambers, 2006; Chen, Wilson, & Tapley, 2010; Velicogna, 2009).

GRACE was implemented and operated as a cooperation between the National Aeronautics and Space Administration (NASA) in the United States of America and the German

Aerospace Center (DLR). It was a joint proposal by the Center of Space Research at the University of Texas (CSR), the German Research Centre for Geosciences (GFZ), the Jet Propulsion Laboratory (JPL), Space Systems/Loral (SSL), DLR and Astrium to NASA's Earth System Science Pathfinder (ESSP) program.

The measurement principle of GRACE relies on extremely precise ranging measurements between a leading and a trailing satellite in the same orbit. Both satellites can be viewed as proof masses in Earth's gravitational field, thus knowledge about the absolute and relative positions and their rate of change can be used to infer information about the mass distribution causing the gravitational pull. The twin-satellites were launched aboard a Rokot/Briz-KM launch vehicle from Plesetsk, Russia on March 17, 2002. Both spacecraft were placed in a near-circular, polar orbit at an initial height of about 500 km with a separation of about 220 km. Following a battery failure in September 2017, science operations were terminated in October 2017. Both satellites were subsequently decommissioned and re-entered the atmosphere on December 24, 2017 (GRACE-B) and March 10, 2018 (GRACE-A) respectively.

The primary science objectives of GRACE were to continuously monitor Earth's time-variable gravity field and to provide atmosphere profiles through radio occultation. To achieve these goals, both satellites were equipped with an identical payload designed to measure the absolute position and orientation in space, the relative distance between both spacecraft, and the forces acting on the satellite bodies. The satellites' position is tracked using a Global Positioning System (GPS) receiver, which also provides the time system all other instruments are aligned to. For gravity field recovery, the most important sensor is the K-band ranging instrument (KBR), which continuously measures the distance between the satellites. A star camera assembly (SCA), consisting of two heads located in the side panels of the satellite body provides attitude information. In order to distinguish between gravitational and non-gravitational forces acting on the satellite, an accelerometer (ACC) in each satellite's center of mass measures non-conservative accelerations acting on the satellite body.

The GRACE successor, GRACE Follow-On (GRACE-FO) was successfully launched on May 22, 2018 from Vandenberg Air Force Base aboard a SpaceX Falcon 9 rocket. GRACE-FO was implemented and is operated under a German/US partnership, as was GRACE. The instrumentation of GRACE-FO is an evolution compared to its predecessor, driven by technical advancements and lessons learned from the GRACE mission. Key differences include a third star camera head and improved mounting of the camera assembly for better attitude determination, an updated accelerometer and improvements to the IMU, the GPS receiver, and the K-band ranging instrument. GRACE-FO is also a technical demonstrator for a laser ranging interferometer (LRI), which has provided the first ever optical interferometry between two satellites. The In-Orbit-Checkout phase for the mission successfully ended in January 2019, which means that science data has been available since June 2019.

While the instrumentation aboard GRACE-FO is a clear evolution compared to GRACE, the design parameters such a orbit height, inclination, and eccentricity are identical for both missions. This means that the spatio-temporal sampling characteristics of GRACE

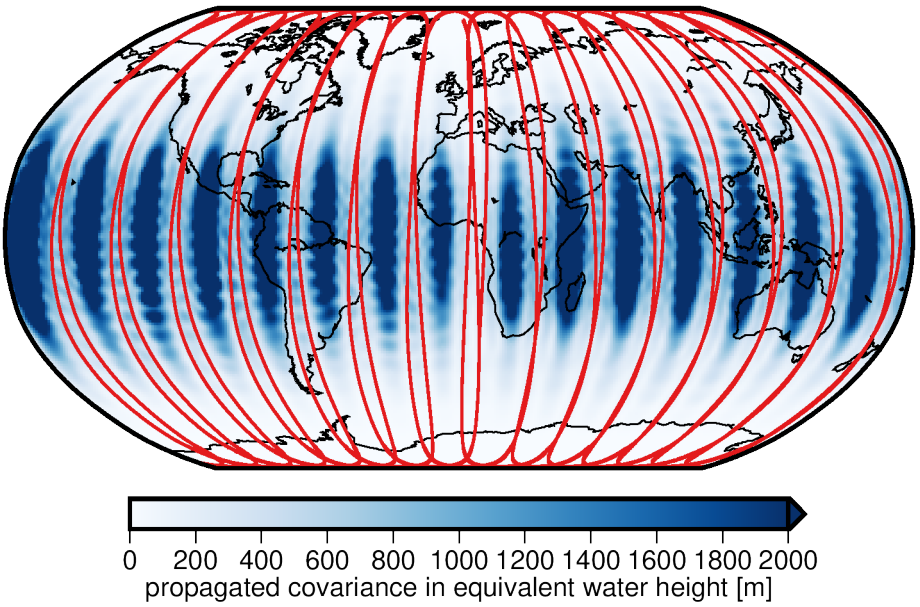

Figure 1.1.: Accuracy of an unconstrained daily GRACE solution propagated to space domain. The red line shows the ground track of the satellites for the given day.

can be directly applied to GRACE-FO as well. While the North-South sampling determined by the sampling rate of the measurement system due to the polar orbit of the satellites, the East-West sampling is determined by the unique equator crossing within a given time span. In a typical, i.e. non-repeat, orbit cycle the GRACE/GRACE-FO satellites perform 15 full revolutions per day. Weigelt, Sneeuw, Schrama, and Visser (2013) have shown that this is only sufficient to resolve the global gravity field up to spherical harmonic order 15. In the spatial domain this means that the information gain from the satellite missions is concentrated in areas next to ground tracks, while little to no information is gained for regions between ground tracks. This effect is shown in figure 1.1, by examining the accuracy of an unconstrained daily GRACE solution. As can be seen, the gravity field in regions between ground-tracks cannot reasonably be determined as they exhibit uncertainties in the order of a few kilometers of equivalent water height, while the expected signal lies in the centimeter range. A homogeneous observation distribution, which is a requirement for a stable determination of the global gravity field, is only reached after approximately one month. This is also the sampling of the primary GRACE/GRACE-FO data products, as provided by the official GRACE processing centers.

There are however geophysical processes which occur on sub-monthly time scales. Floods, for example, may only take hours to days to build up and drain. To mitigate the deficiencies in the spatio-temporal sampling of GRACE which are a direct result of the reduced accumulation period, different approaches have been developed. The most prominent one is the so called Kalman filter approach introduced by Kurtenbach, Mayer-Gürr, and Eicker (2009) and later refined by Kurtenbach et al. (2012). This method has already been successfully used in a variety of gravity field solutions (Mayer-Gürr et

al., 2016, 2018; Mayer-Gürr, Kurtenbach, & Eicker, 2010; Mayer-Gürr, Zehentner, Klinger, & Kvas, 2014). The key characteristic of this approach is the use of stochastic information about Earth's gravity field in order to stabilize daily solutions in a two-step prediction-correction scheme. Since in principle, this approach only requires information from the past, it provides a natural starting point for near real-time applications. Another approach which aims at providing high-frequency gravity field variations is the sliding-window approach presented in Sakumura, Bettadpur, Save, and McCullough (2016). Here regularized solutions are produced by forming a weighted average over a longer time span. The weighted average is designed in a way that observations of the central, reference epoch have the largest contribution, while the weights of epochs further in the past and future slowly decrease. These sub-monthly gravity field solutions have been used to study a variety of geophysical processes, for example, ocean variations (Zenner et al., 2014) or large flood events (e.g., Gouweleeuw et al., 2018). Flood early-warning and forecasting systems additionally require information in near-real time (NRT) to estimate probabilistic flood risk with typical lead times of a few days for larger river basins. Thus, total water storage anomalies (TWSA) derived from temporal variations of the Earth's gravity field with not only an increased temporal sampling, but also with low-latency are key to observe such dynamic events. One prerequisite for such a unique data product is a sophisticated processing chain for the satellite measurements. In order to fully exploit the information content of the observations, systematic and random errors have to be understood and treated properly. Secondly, to mitigate the sparse data coverage, prior information has to be introduced appropriately. It is key to find a balance between inhibiting noise and overconstraining the solution. Further challenges arise when these concepts are applied in NRT. The availability and quality of observations and auxiliary data lead to compromises in the processing chain. Furthermore, the lack of information from the future requires a tailored scheme to combine observations and prior information.

This thesis presents an approach which tackles these challenges and enables the operational processing of gravity field observations to derive daily snapshots of Earth's gravity field. The method was tested in a three-month long test run based on GRACE mission data, where a maximum latency of 5 days was required. The performance of the approach is evaluated by a comparison of the operational solutions with a reanalysis time series, and a post-processing solution.

1.3. Outline of the thesis

Chapter 2 provides an overview how sub-monthly mass variations in the Earth system can be inferred from GRACE/GRACE-FO. The basic concepts of gravity field recovery using least-squares adjustment are introduced. This includes the formulation of observation equations, the elimination non-gravity field parameters from the adjustment problem, and the introduction of prior information. After the general framework of constraint gravity field solutions is presented, the special case where sub-monthly gravity field variations are modeled as stationary process is investigated. By introducing vector autoregressive models, a highly efficient approach of how these pseudo-observations can be introduced

into the gravity field recovery process is described. The Kalman filter is derived through the formulation of appropriate observation equations and an equivalent adjustment problem to the Kalman smoother is presented. This is the basis for a generalization of the approach of Kurtenbach et al. (2012) to vector autoregressive models of arbitrary order.

In chapter 3, concepts and requirements for operational near real-time processing of GRACE/GRACE-FO data are outlined. As a first step, a thorough review of all required data products, the interdependency between each data set and a detailed processing chain is given. All required tasks from raw data processing to the derivation of gridded mass anomalies are described and the corresponding scheduling is presented. Key steps, in this process are the computation of kinematic satellite orbits, establishment of the functional and stochastic observation model, and the determination of an appropriate observation weighting. Next to the daily processing schedule, necessary auxiliary tasks which are performed in irregular intervals are presented. Finally, contingency plans for possible failures during the processing are discussed.

Chapter 4, introduces the European Gravity Service for Improved Emergency Management (EGSIEM) near real-time (NRT) service and shows the performance of the developed processing chain in an operational test run. Firstly, pre-operational simulations concerning the expected data characteristics during the later stages of the GRACE mission are presented. Then results of the three-month operational test run, where daily GRACE solutions were computed in a fully automated fashion are presented. Focus is given here to the changing data characteristics and the challenges during the last months of the GRACE science operations.

A reanalysis of the operational gravity field solutions produced during the NRT Service test run is presented in chapter 5. This reprocessing serves as basis for a quantitative evaluation of the operational solutions and the identification of areas for improvement for future NRT applications.

Finally, in Chapter 6, the findings are summarized and an outlook on the application of the developed NRT processing chain for future satellite missions is given.

2. High-frequency mass variations from GRACE/GRACE-FO

2.1. Gravity field recovery from GRACE/GRACE-FO

In order to recover Earth's gravity field from satellite data in a least squares sense the acquired observation vector $\mathbf{l}$ has to be related to the sought-after gravity field parameters $\mathbf{x}$ through a functional model of the form

$$\mathbf{l} = f(\mathbf{x}, \ldots). \tag{2.1}$$

The approach chosen in this thesis makes use of kinematic orbit positions $\mathbf{r}_\mathrm{A}$ and $\mathbf{r}_\mathrm{B}$ of the satellites and inter-satellite range-rates $\dot{\rho}_\mathrm{AB}$. Therefore, the observation vector has the structure

$$\mathbf{l} = \begin{bmatrix} \mathbf{r}_\mathrm{A} \\ \mathbf{r}_\mathrm{B} \\ \dot{\rho}_\mathrm{AB} \end{bmatrix}, \tag{2.2}$$

where each of the vectors $\mathbf{r}_A$ and $\mathbf{r}_B$, are time series of kinematic orbit positions for satellite A and B respectively, and $\dot{\rho}_\mathrm{AB}$ are range-rate observations between the satellites. The range-rate observations are connected to the satellites' positions and velocities through

$$\dot{\rho}_\mathrm{AB} = \mathbf{e}_\mathrm{AB} \cdot (\dot{\mathbf{r}}_\mathrm{B} - \dot{\mathbf{r}}_\mathrm{A}), \tag{2.3}$$

where $\mathbf{e}_\mathrm{AB} = \frac{1}{\|\mathbf{r}_B - \mathbf{r}_A\|}(\mathbf{r}_B - \mathbf{r}_A)$ is a unit vector in line-of-sight (LOS) direction between the satellites. By combining the satellite's position and velocity to the satellite state $\mathbf{y} = [\dot{\mathbf{r}}^T, \mathbf{r}^T]^T$, the observation vector $\mathbf{l}$ can be expressed as a function of both satellites' states, with

$$\mathbf{l} = f(\mathbf{y}_A, \mathbf{y}_B). \tag{2.4}$$

The connection between the satellite state and the sought-after gravity field parameters is established through Newton's second law of motion. This axiom states that the change of momentum acting on a body is proportional to the forces applied. Assuming constant mass of the body in motion, this can be expressed through

$$\mathbf{F} = m\ddot{\mathbf{r}}, \tag{2.5}$$

where $\mathbf{F}$ is the sum of all forces acting on the body, m is the body's mass and $\ddot{\mathbf{r}}$ is its acceleration. To utilize (2.5) as function model, it first has to be rearranged to

$$\ddot{\mathbf{r}} = \frac{1}{m}\mathbf{F}. \tag{2.6}$$

By integrating (2.6) twice, the inhomogeneous system of differential equations

$$\begin{aligned} \dot{\mathbf{r}}(t) &= \dot{\mathbf{r}}_0 + \frac{1}{m}\int_{t_0}^{t} \mathbf{F}(t')dt' \\ \mathbf{r}(t) &= \mathbf{r}_0 + \dot{\mathbf{r}}_0(t-t_0) + \frac{1}{m}\int_{t_0}^{t}\int_{t_0}^{t'} \mathbf{F}(t'')dt''dt' \end{aligned} \tag{2.7}$$

is obtained. The solution to this system of equations, the satellite state $\mathbf{y}(t)$, can be determined in a variety of ways. Two popular approaches include the integral equation approach (e.g., Mayer-Gürr, 2006), or the variational equation approach (e.g., Beutler & Mervart, 2010; Montenbruck & Gill, 2000). A detailed review of the variational equation approach and its application to GRACE/GRACE-FO can be found in Ellmer (2018). Once the solution to (2.7) is available, the satellite state can be written as a function of the initial state $\mathbf{y}_0$ and the forces acting on the satellite, with

$$\mathbf{y} = \mathbf{y}(\mathbf{y}_0, \mathbf{F}(\mathbf{x}, \ldots)) = \mathbf{y}(\mathbf{x}, \mathbf{y}_0, \ldots). \tag{2.8}$$

In (2.8) it is explicitly stated, that $\mathbf{F}$ not only depends on Earth's gravity field but is a combination of a variety of forces, including, for example, atmospheric drag, solar radiation pressure and the gravitational attraction of other bodies in the solar system. A comprehensive list of all components of $\mathbf{F}$ and corresponding geophysical models used in gravity field recovery can be found in table 3.3. Substituting the solution (2.7) into (2.4) then establishes the relation between the observations and the unknown parameters

$$\mathbf{l} = f(\mathbf{x}, \mathbf{y}_{0,A}, \mathbf{y}_{0,B}, \ldots). \tag{2.9}$$

In practice, $\mathbf{F}$ will be evaluated using fixed model output, resulting in a functional model f_m only depending on Earth's gravity field. However, for GRACE and GRACE-FO, non-conservative accelerations acting on the satellites are measured by the onboard accelerometers which suffer from biases and drifts. These sensor imperfections are notoriously difficult to model beforehand and are therefore also introduced as unknowns in the adjustment process (e.g., Klinger & Mayer-Gürr, 2016). For brevity, all non-gravity field parameters, including initial states and instrument calibration parameters are combined in the vector $\mathbf{z}$, which leads to the, generally non-linear, observation model

$$\mathbf{l} = f_m(\mathbf{x}, \mathbf{z}). \tag{2.10}$$

In order to estimate the unknown parameters $(\mathbf{x}, \mathbf{z})$ from the functional model (2.1) in a least squares sense, f_m is expanded into a Taylor series with respect to $(\mathbf{x}, \mathbf{z})$ at $(\mathbf{x}_0, \mathbf{z}_0)$,

following the standard procedure for a non-linear least squares adjustment (e.g., Koch, 2004). The resulting power series

$$\mathbf{l} = f_m(\mathbf{x}_0, \mathbf{z}_0) + \left.\frac{\partial f_m}{\partial \mathbf{x}}\right|_{(\mathbf{x}_0,\mathbf{z}_0)} (\mathbf{x} - \mathbf{x}_0) + \left.\frac{\partial f_m}{\partial \mathbf{z}}\right|_{(\mathbf{x}_0,\mathbf{z}_0)} (\mathbf{z} - \mathbf{z}_0) + \cdots \tag{2.11}$$

is then truncated after the linear term. For clarity, the design matrices $\mathbf{A}$ and $\mathbf{B}$, which are the Jacobian of f_m with respect to $\mathbf{x}$ and $\mathbf{z}$, evaluated at $(\mathbf{x}_0, \mathbf{z}_0)$ and the parameter corrections $\Delta\mathbf{x}$ and $\Delta\mathbf{z}$ defined as $\mathbf{x} - \mathbf{x}_0$ and $\mathbf{z} - \mathbf{z}_0$ are introduced. Moving the zero-order term of the power series to the left hand side yields

$$\Delta\mathbf{l} = \mathbf{l} - f_m(\mathbf{x}_0, \mathbf{z}_0) = \mathbf{A}\Delta\mathbf{x} + \mathbf{B}\Delta\mathbf{z} + \mathbf{e}, \tag{2.12}$$

which relates the reduced observations $\Delta\mathbf{l}$ to the parameter corrections. The residual vector $\mathbf{e}$ is added to the right hand side of (2.12) because the system of observation equations will generally be inconsistent due to measurement errors in $\mathbf{l}$ and model imperfections.

The residuals are assumed to be correlated, hence a metric $\mathbf{P}$ has to be defined in order to appropriately minimize the norm of $\mathbf{e}$. In the case at hand, the metric is given by the inverse of the covariance matrix of the residuals $\mathbf{\Sigma_e}$, that is $\mathbf{P} \equiv \mathbf{\Sigma_e}^{-1}$. To obtain the metric, covariance propagation is applied to (2.12) which yields

$$\mathbf{\Sigma_e} = \mathbf{\Sigma_l}, \tag{2.13}$$

where $\mathbf{\Sigma_l}$ is the covariance matrix of the observations $\mathbf{l}$. The determination of $\mathbf{\Sigma_l}$ is key for a statistically optimal estimate of $\mathbf{x}$. For a comprehensive description of a method which determines the covariance matrix of observations iteratively during the adjustment process, the reader is referred to Ellmer (2018). Computing the system of normal equations from (2.12) leads to

$$\begin{bmatrix} \mathbf{A}^T\mathbf{P}\mathbf{A} & \mathbf{A}^T\mathbf{P}\mathbf{B} \\ \mathbf{B}^T\mathbf{P}\mathbf{A} & \mathbf{B}^T\mathbf{P}\mathbf{B} \end{bmatrix} \begin{bmatrix} \Delta\hat{\mathbf{x}} \\ \Delta\hat{\mathbf{z}} \end{bmatrix} = \begin{bmatrix} \mathbf{A}^T\mathbf{P}\Delta\mathbf{l} \\ \mathbf{B}^T\mathbf{P}\Delta\mathbf{l} \end{bmatrix}, \tag{2.14}$$

or

$$\begin{bmatrix} \mathbf{N_{xx}} & \mathbf{N_{xz}} \\ \mathbf{N_{xz}}^T & \mathbf{N_{zz}} \end{bmatrix} \begin{bmatrix} \Delta\hat{\mathbf{x}} \\ \Delta\hat{\mathbf{z}} \end{bmatrix} = \begin{bmatrix} \mathbf{n_x} \\ \mathbf{n_z} \end{bmatrix}, \tag{2.15}$$

which can be solved for the estimates $\Delta\hat{\mathbf{x}}$ and $\Delta\hat{\mathbf{z}}$.

In this thesis the unknown gravity field parameters are of primary interest, hence an adjustment problem which only explicitly contains $\Delta\mathbf{x}$ is preferred. This can be achieved by performing parameter elimination (e.g., Koch, 2004). By applying the orthogonal projector $\Pi_{\mathbf{B}}^{\perp} = \mathbf{I} - \mathbf{B}(\mathbf{B}^T\mathbf{P}\mathbf{B})^{-1}\mathbf{B}^T\mathbf{P}$ to (2.12), the system of observation equations is mapped into the orthogonal space of $\mathbf{B}$, resulting in

$$\underbrace{\Pi_{\mathbf{B}}^{\perp}\Delta\mathbf{l}}_{\Delta\bar{\mathbf{l}}} = \underbrace{\Pi_{\mathbf{B}}^{\perp}\mathbf{A}}_{=\bar{\mathbf{A}}}\Delta\mathbf{x} + \underbrace{\Pi_{\mathbf{B}}^{\perp}\mathbf{B}}_{=\mathbf{0}}\Delta\mathbf{z} + \underbrace{\Pi_{\mathbf{B}}^{\perp}\mathbf{e}}_{=\bar{\mathbf{e}}}. \tag{2.16}$$

Since the residuals are now subject to a linear transformation, their covariance matrix has to be consequently propagated through

$$\boldsymbol{\Sigma}_{\bar{\mathbf{e}}} = \Pi_{\mathbf{B}}^{\perp} \boldsymbol{\Sigma}_{\mathbf{e}} \Pi_{\mathbf{B}}^{\perp^T}. \tag{2.17}$$

After substituting (2.13) this can be rearranged to

$$\begin{aligned}
\boldsymbol{\Sigma}_{\bar{\mathbf{e}}} &= \Pi_{\mathbf{B}}^{\perp} \boldsymbol{\Sigma}_{\mathbf{l}} \Pi_{\mathbf{B}}^{\perp^T} \\
&= \Pi_{\mathbf{B}}^{\perp} [\Pi_{\mathbf{B}}^{\perp} \boldsymbol{\Sigma}_{\mathbf{l}}]^T \\
&= \Pi_{\mathbf{B}}^{\perp} [\boldsymbol{\Sigma}_{\mathbf{l}} - \mathbf{B}(\mathbf{B}^T\mathbf{P}\mathbf{B})^{-1}\mathbf{B}^T]^T \\
&= \Pi_{\mathbf{B}}^{\perp} [\boldsymbol{\Sigma}_{\mathbf{l}} - \mathbf{B}(\mathbf{B}^T\mathbf{P}\mathbf{B})^{-1}\mathbf{B}^T] \\
&= \Pi_{\mathbf{B}}^{\perp} \boldsymbol{\Sigma}_{\mathbf{l}} - \underbrace{\Pi_{\mathbf{B}}^{\perp}\mathbf{B}}_{=\mathbf{0}}(\mathbf{B}^T\mathbf{P}\mathbf{B})^{-1}\mathbf{B}^T,
\end{aligned} \tag{2.18}$$

from which follows

$$\boldsymbol{\Sigma}_{\mathbf{l}}^{-1} = \boldsymbol{\Sigma}_{\bar{\mathbf{e}}}^{-1} \Pi_{\mathbf{B}}^{\perp}. \tag{2.19}$$

To obtain a least squares solution from the system of equations (2.16), the weighted square sum of the projected residuals

$$q_{\bar{\mathbf{e}}} = \bar{\mathbf{e}}^T \boldsymbol{\Sigma}_{\bar{\mathbf{e}}}^{-1} \bar{\mathbf{e}} \tag{2.20}$$

has to be minimized. By exploiting the idempotence of orthogonal projectors (Roman, 2007), (2.19) can be substituted into (2.20):

$$q_{\bar{\mathbf{e}}} = \bar{\mathbf{e}}^T \boldsymbol{\Sigma}_{\bar{\mathbf{e}}}^{-1} \bar{\mathbf{e}} = \bar{\mathbf{e}}^T \boldsymbol{\Sigma}_{\bar{\mathbf{e}}}^{-1} (\Pi_{\mathbf{B}}^{\perp} \bar{\mathbf{e}}) = \bar{\mathbf{e}}^T (\boldsymbol{\Sigma}_{\bar{\mathbf{e}}}^{-1} \Pi_{\mathbf{B}}^{\perp}) \bar{\mathbf{e}} = \bar{\mathbf{e}}^T \boldsymbol{\Sigma}_{\mathbf{l}}^{-1} \bar{\mathbf{e}}. \tag{2.21}$$

Thus, the least squares solution to (2.16) can be obtained by using the original metric $\mathbf{P} \equiv \boldsymbol{\Sigma}_{\mathbf{l}}^{-1}$. The final overdetermined system of observation equations therefore reads

$$\Delta\bar{\mathbf{l}} = \bar{\mathbf{A}}\Delta\mathbf{x} + \bar{\mathbf{e}}. \tag{2.22}$$

Parameter elimination can also be performed on a normal equation level. This can easily be shown by computing and expanding the system normal equations corresponding to the least squares adjustment (2.22). Starting with the normal equations coefficient matrix, it is found that

$$\begin{aligned}
\bar{\mathbf{A}}^T\mathbf{P}\bar{\mathbf{A}} &= \mathbf{A}^T \Pi_{\mathbf{B}}^{\perp^T} \mathbf{P} \Pi_{\mathbf{B}}^{\perp} \mathbf{A} \\
&= \mathbf{A}^T (\mathbf{I} - \mathbf{B}(\mathbf{B}^T\mathbf{P}\mathbf{B})^{-1}\mathbf{B}^T\mathbf{P})^T \mathbf{P} \Pi_{\mathbf{B}}^{\perp} \mathbf{A} \\
&= \mathbf{A}^T (\mathbf{I} - \mathbf{P}\mathbf{B}(\mathbf{B}^T\mathbf{P}\mathbf{B})^{-1}\mathbf{B}^T) \mathbf{P} \Pi_{\mathbf{B}}^{\perp} \mathbf{A} \\
&= \mathbf{A}^T (\mathbf{P} - \mathbf{P}\mathbf{B}(\mathbf{B}^T\mathbf{P}\mathbf{B})^{-1}\mathbf{B}^T\mathbf{P}) \Pi_{\mathbf{B}}^{\perp} \mathbf{A} \\
&= \mathbf{A}^T \mathbf{P} (\mathbf{I} - \mathbf{B}(\mathbf{B}^T\mathbf{P}\mathbf{B})^{-1}\mathbf{B}^T\mathbf{P}) \Pi_{\mathbf{B}}^{\perp} \mathbf{A} \\
&= \mathbf{A}^T \mathbf{P} \Pi_{\mathbf{B}}^{\perp} \Pi_{\mathbf{B}}^{\perp} \mathbf{A} = \mathbf{A}^T (\mathbf{P} \Pi_{\mathbf{B}}^{\perp}) \mathbf{A} \\
&= \mathbf{A}^T (\mathbf{P} - \mathbf{P}\mathbf{B}(\mathbf{B}^T\mathbf{P}\mathbf{B})^{-1}\mathbf{B}^T\mathbf{P}) \mathbf{A} \\
&= \underbrace{\mathbf{A}^T\mathbf{P}\mathbf{A}}_{=\mathbf{N}_{xx}} - \underbrace{\mathbf{A}^T\mathbf{P}\mathbf{B}}_{=\mathbf{N}_{xz}} (\underbrace{\mathbf{B}^T\mathbf{P}\mathbf{B}}_{=\mathbf{N}_{zz}})^{-1} \underbrace{\mathbf{B}^T\mathbf{P}\mathbf{A}}_{=\mathbf{N}_{xz}^T}.
\end{aligned} \tag{2.23}$$

Performing the same operations for the right hand side leads to

$$\bar{\mathbf{A}}^T\mathbf{P}\Delta\bar{\mathbf{l}} = \underbrace{\mathbf{A}^T\mathbf{P}\Delta\mathbf{l}}_{=\mathbf{n_x}} - \mathbf{A}^T\mathbf{P}\mathbf{B}(\mathbf{B}^T\mathbf{P}\mathbf{B})^{-1}\underbrace{\mathbf{B}^T\mathbf{P}\Delta\mathbf{l}}_{=\mathbf{n_z}}. \tag{2.24}$$

Combining both the expressions for the coefficient matrix and right hand side finally yields a system of normal equations which only has $\Delta\hat{\mathbf{x}}$ as explicit unknowns:

$$(\mathbf{N_{xx}} - \mathbf{N_{xz}}\mathbf{N_{zz}}^{-1}\mathbf{N_{xz}}^T)\Delta\hat{\mathbf{x}} = (\mathbf{n_x} - \mathbf{N_{xz}}\mathbf{N_{zz}}^{-1}\mathbf{n_z}). \tag{2.25}$$

This relates the system of observation equations (2.16) where $\mathbf{z}$ is eliminated, to the full system of normal equations arising from (2.12), through the matrices $\mathbf{N_{xx}}, \mathbf{N_{xz}}$, and $\mathbf{N_{zz}}$ as well as the right hand side vectors $\mathbf{n_x}$ and $\mathbf{n_z}$.

For some applications, not only the parameters, but also the post-fit residuals $\hat{\mathbf{e}}$ are of interest. After the parameter subset $\Delta\mathbf{z}$ is eliminated, the estimates $\Delta\hat{\mathbf{z}}$ are not explicitly available, thus $\hat{\mathbf{e}} = \Delta\mathbf{l} - \mathbf{A}\Delta\hat{\mathbf{x}} - \mathbf{B}\Delta\hat{\mathbf{z}}$ can no longer be directly evaluated. However, it can easily be shown that $\hat{\bar{\mathbf{e}}} = \Delta\bar{\mathbf{l}} - \bar{\mathbf{A}}\Delta\hat{\mathbf{x}} = \hat{\mathbf{e}}$. Simply factoring out the orthogonal projector from the expression $\Delta\bar{\mathbf{l}} - \bar{\mathbf{A}}\Delta\hat{\mathbf{x}}$ yields

$$\hat{\bar{\mathbf{e}}} = \Delta\bar{\mathbf{l}} - \bar{\mathbf{A}}\Delta\hat{\mathbf{x}} = \Pi^{\perp}_{\mathbf{B}}(\Delta\mathbf{l} - \mathbf{A}\Delta\hat{\mathbf{x}} - \mathbf{B}\Delta\hat{\mathbf{z}}) = \Pi^{\perp}_{\mathbf{B}}\hat{\mathbf{e}}. \tag{2.26}$$

By further expanding the right hand side of this equation

$$\Pi^{\perp}_{\mathbf{B}}\hat{\mathbf{e}} = \hat{\mathbf{e}} - \mathbf{B}(\mathbf{B}^T\mathbf{P}\mathbf{B})^{-1}\mathbf{B}^T\mathbf{P}\hat{\mathbf{e}} \tag{2.27}$$

is obtained. For $\hat{\bar{\mathbf{e}}} = \hat{\mathbf{e}}$ to hold true, it is sufficient to show that $\mathbf{B}^T\mathbf{P}\hat{\mathbf{e}} = \mathbf{0}$. By substituting $\hat{\mathbf{e}}$ this expression can be related to the full system of normal equations (2.14) as

$$\mathbf{B}^T\mathbf{P}\hat{\mathbf{e}} = \mathbf{B}^T\mathbf{P}\Delta\mathbf{l} - \mathbf{B}^T\mathbf{P}\mathbf{A}\Delta\hat{\mathbf{x}} - \mathbf{B}^T\mathbf{P}\mathbf{B}\Delta\hat{\mathbf{z}} = \mathbf{n_z} - \mathbf{N_{xz}}^T\Delta\hat{\mathbf{x}} - \mathbf{N_{zz}}\Delta\hat{\mathbf{z}}. \tag{2.28}$$

This expression can easily be verified to yield $\mathbf{0}$ by examining the second block row of (2.14), thus $\hat{\mathbf{e}} = \hat{\bar{\mathbf{e}}} = \Delta\bar{\mathbf{l}} - \bar{\mathbf{A}}\Delta\hat{\mathbf{x}}$.

In the following, the bar denoting reduced observations, design matrix, and residual vector after parameter elimination is dropped for brevity. It is however assumed that there are non-gravity field parameters eliminated in the discussed least squares adjustments.

2.2. Incorporation of prior information

As outlined in section 1.2 global, sub-monthly gravity field variations cannot be determined from GRACE/GRACE-FO alone, but require prior information. One way to introduce said prior information is by extending the least-squares adjustment (2.12) with pseudo-observations $\mathbf{l}_p$ of the form

$$\mathbf{l}_p = \mathbf{F}\mathbf{x} + \mathbf{v}, \qquad \mathbf{v} \sim \mathcal{N}(\mathbf{0}, \mathbf{\Sigma_v}), \tag{2.29}$$

(e.g. Koch & Kusche, 2002). These pseudo-observations are not the result of a measurement process, but are generally a linear combination of information about the

parameters, for example, derived from a physical law. To be consistent with the actual GRACE/GRACE-FO observations, the Taylor series expansion point has to be reduced in the same fashion, leading to the reduced pseudo-observations $\Delta\mathbf{l}_p = \mathbf{l}_p - \mathbf{F}\mathbf{x}_0$. For simplicity it is assumed that $\Delta\mathbf{l}_p = \mathbf{0}$ and $\mathbf{F} = \mathbf{I}$, with $\mathbf{I}$ being a unit matrix of appropriate dimensions. The resulting observation equations

$$\mathbf{0} = \mathbf{I}\Delta\mathbf{x} + \mathbf{v}, \quad \mathbf{v} \sim \mathcal{N}(\mathbf{0}, \boldsymbol{\Sigma}_\mathbf{v}), \tag{2.30}$$

can be interpreted as conditions for the sub-monthly gravity field variations which do not have to be strictly fulfilled (Caspary & Wichmann, 1994). Specifically, (2.30) states that the parameters are close to the background models represented by $\mathbf{x}_0$, where "close" is determined by the covariance matrix $\boldsymbol{\Sigma}_\mathbf{v}$. Combining (2.22) and (2.30) then leads to the blocked system of observation equations

$$\begin{bmatrix}\Delta\mathbf{l}\\ \mathbf{0}\end{bmatrix} = \begin{bmatrix}\mathbf{A}\\ \mathbf{I}\end{bmatrix}\Delta\mathbf{x} + \begin{bmatrix}\mathbf{e}\\ \mathbf{v}\end{bmatrix}, \quad \begin{bmatrix}\mathbf{e}\\ \mathbf{v}\end{bmatrix} \sim \mathcal{N}\left(\begin{bmatrix}\mathbf{0}\\ \mathbf{0}\end{bmatrix}, \begin{bmatrix}\boldsymbol{\Sigma}_\mathbf{l} & \\ & \boldsymbol{\Sigma}_\mathbf{v}\end{bmatrix}\right). \tag{2.31}$$

The block diagonal structure of the combined covariance matrix implies that observations and prior information are uncorrelated. This assumption is certainly justified, as the pseudo-observations are not produced by a measurement process, but rather from external information about the gravity field. The system of normal equations arising from (2.31) takes the form

$$(\mathbf{A}^T\boldsymbol{\Sigma}_\mathbf{l}^{-1}\mathbf{A} + {\boldsymbol{\Sigma}_\mathbf{v}}^{-1})\Delta\hat{\mathbf{x}} = \mathbf{A}^T\boldsymbol{\Sigma}_\mathbf{l}^{-1}\Delta\bar{\mathbf{l}}, \tag{2.32}$$

which can be abbreviated to $(\mathbf{N} + {\boldsymbol{\Sigma}_\mathbf{v}}^{-1})\Delta\hat{\mathbf{x}} = \mathbf{n}$ by introducing the normal equation coefficient matrix $\mathbf{N}$ and the corresponding right-hand-side $\mathbf{n}$.

Up to now, no restrictions except for positive definiteness, have been imposed onto $\boldsymbol{\Sigma}_\mathbf{v}$. However, given the application discussed in this thesis, a few further assumptions about the characteristics of the sought-after high frequency gravity field solutions can be made. Given that only corrections $\Delta\mathbf{x}$ are estimated, it can be assumed that the expectancy, variances and covariances of the underlying process do not vary with time, if all secular and seasonal gravity signals are properly modeled in $\mathbf{x}_0$ (Kurtenbach et al., 2012). If this is the case, the process is wide-sense stationary (e.g., Lütkepohl, 2005) which is extremely beneficial for practical applications. Furthermore, given a high-quality a priori gravity field, the time series of high-frequency gravity field estimates can also be assumed to be centered, which is already implied in (2.31).

A key feature of stationary stochastic processes is that their covariance matrix is block Toeplitz (Akaike, 1973). This means that if the vector of unknown parameters contains each epoch $\Delta\mathbf{x}_i$ with $i \in \{0, \ldots, N-1\}$, ascending in time with $\Delta\mathbf{x} = [\Delta\mathbf{x}_0^T, \ldots, \Delta\mathbf{x}_{N-1}^T]^T$, the corresponding covariance matrix can be simply expressed as

$$(\boldsymbol{\Sigma}_\mathbf{v})_{ij} = \begin{cases}\boldsymbol{\Sigma}_\mathbf{v}(|j-i|) & \text{for } i \leq j\\ \boldsymbol{\Sigma}_\mathbf{v}(|j-i|)^T & \text{otherwise}\end{cases} \tag{2.33}$$

or more explicitly as

$$\boldsymbol{\Sigma}_{\mathbf{v}} = \begin{bmatrix} \boldsymbol{\Sigma}_{\mathbf{v}}(0) & \boldsymbol{\Sigma}_{\mathbf{v}}(1) & \boldsymbol{\Sigma}_{\mathbf{v}}(2) & \dots \\ \boldsymbol{\Sigma}_{\mathbf{v}}(1)^T & \boldsymbol{\Sigma}_{\mathbf{v}}(0) & \boldsymbol{\Sigma}_{\mathbf{v}}(1) & \dots \\ \boldsymbol{\Sigma}_{\mathbf{v}}(2)^T & \boldsymbol{\Sigma}_{\mathbf{v}}(1)^T & \boldsymbol{\Sigma}_{\mathbf{v}}(0) & \dots \\ \vdots & \vdots & \vdots & \ddots \end{bmatrix}, \tag{2.34}$$

where $\boldsymbol{\Sigma}_{\mathbf{v}}(h)$ is the covariance matrix between two epochs spaced h time steps apart.

In practice, the true spatio-temporal covariance function of the stochastic process is not known, hence it has to be approximated by an empirical estimate. One way to obtain such an empirical estimate is to apply the unbiased estimator

$$\tilde{\boldsymbol{\Sigma}}_{\mathbf{v}}(h) = \frac{1}{M-h} \sum_{j=h}^{M-1} \tilde{\mathbf{v}}_{j-h} \tilde{\mathbf{v}}_j^T, \tag{2.35}$$

to a realization $\tilde{\mathbf{v}}_j \in \mathbb{R}^{mx1}$ with $j \in \{0, \dots, M-1\}$ of the underlying process (Brockwell & Davis, 2010). For the application at hand, such a realization can be obtained from long time series of geophysical model output as discussed in Kurtenbach et al. (2012). The drawback of directly composing (2.34) is that the covariance matrices for all lags $h = \{0, \dots, N-1\}$ need to be estimated for $\boldsymbol{\Sigma}_{\mathbf{v}}$ to be fully determined. This is difficult to achieve as the number of epochs M in the process realization must exceed the length of the covariance function drastically to yield a robust estimate (e.g., Fan, Liao, & Liu, 2016), and the available geophysical models are scarce.

A more practical approach is to use a parametric method to estimate the spatio-temporal correlations of $\tilde{\mathbf{v}}$. The principle difference between parametric and non-parametric methods for spectral estimation is that non-parametric methods do not make assumptions about the underlying process except for stationarity. In contrast, parametric estimators assume that the process satisfies a generating model with known form, but unknown model parameters. To derive spatio-temporal correlations through a parametric estimator, first the model parameters have to be determined. Then the covariance function of the process can be computed based on the now known model coefficients. In cases where the chosen model is close to reality, parametric methods provide a more accurate representation of the spectrum due to the potentially increased redundancy of the estimate (Stoica & Moses, 2005). To exploit this fact, the process which describes the spatial and temporal correlations of the sought after gravity field snapshots, is represented as a finite, stable vector-autoregressive (VAR) model in the form of

$$\mathbf{v}_i = \sum_{k=1}^{p} \boldsymbol{\Phi}_k^{(p)} \mathbf{v}_{i-k} + \mathbf{w}_i, \qquad \mathbf{w}_i \sim \mathcal{N}(\mathbf{0}, \boldsymbol{\Sigma}_{\mathbf{w}}^{(p)}), \tag{2.36}$$

(e.g., Lütkepohl, 2005). In (2.36), $\boldsymbol{\Phi}_k^{(p)} \in \mathbb{R}^{mxm}$ are the VAR model coefficients and $\mathbf{w}_i \in \mathbb{R}^{mx1}$ is a white noise sequence with the covariance structure

$$E\{\mathbf{w}_i \mathbf{w}_j^T\} = \begin{cases} \boldsymbol{\Sigma}_{\mathbf{w}}^{(p)} & \text{if } i = j \\ \mathbf{0} & \text{if } i \neq j \end{cases}. \tag{2.37}$$

The superscript p of $\mathbf{\Phi}_k^{(p)}$ and $\mathbf{\Sigma}_{\mathbf{w}}^{(p)}$ denotes that these quantities are part of a VAR(p) model, where p is the model order. To derive the unknown model coefficients and the white noise covariance matrix, again the sample $\tilde{\mathbf{v}}_i$ can be used. There exist a number of methods to derive these quantities, such as the Yule-Walker (YW) equations and maximum likelihood estimators (e.g., Lütkepohl, 2005), or least squares approaches (Neumaier & Schneider, 2001). A method specifically tailored to the derivation of VAR models from geophysical model output is presented in section 2.4.

Once the model parameters and white noise covariance are determined, the spatio-temporal correlations of the process for all lags h and consequently (2.34) can be computed. From a computational perspective it is however beneficial to avoid assembling (2.34) directly, if either the number of epochs N is large or the dimension m is high. Then, the VAR equation can be used to transform the pseudo-observation equations in (2.31). By separating $\mathbf{v}$ and $\mathbf{w}$ in (2.36) to the left- and right-hand side respectively,

$$\mathbf{w}_i = \mathbf{v}_i - \sum_{k=1}^{p} \mathbf{\Phi}_k^{(p)} \mathbf{v}_{i-k} \tag{2.38}$$

is obtained. When assembled in ascending chronological order for all epochs $i \in \{0, \dots, N-1\}$, (2.38) yields a linear mapping $\bar{\mathbf{\Phi}}$ relating the full time series of process realizations $\mathbf{v}$ to the white noise sequence $\mathbf{w}$ through

$$\mathbf{w} = \bar{\mathbf{\Phi}}\mathbf{v}. \tag{2.39}$$

To evaluate (2.38) for epochs of the white noise sequence with $i < p$, epochs of $\mathbf{v}$ with $i < 0$ are required. These epochs are assumed to be unknown, so warm-up effects are introduced to (2.39). To mitigate this undesired behavior, shorter VAR models can be estimated and placed in the corresponding block rows of $\bar{\mathbf{\Phi}}$. Assuming a maximum model order of $p_{\max} = 3$, the structure of $\bar{\mathbf{\Phi}}$ is then given by

$$\bar{\mathbf{\Phi}} = \begin{bmatrix} \mathbf{I} & & & & & \\ -\mathbf{\Phi}_1^{(1)} & \mathbf{I} & & & & \\ -\mathbf{\Phi}_2^{(2)} & -\mathbf{\Phi}_1^{(2)} & \mathbf{I} & & & \\ -\mathbf{\Phi}_3^{(3)} & -\mathbf{\Phi}_2^{(3)} & -\mathbf{\Phi}_1^{(3)} & \mathbf{I} & & \\ & -\mathbf{\Phi}_3^{(3)} & -\mathbf{\Phi}_2^{(3)} & -\mathbf{\Phi}_1^{(3)} & \mathbf{I} & \\ & & \ddots & \ddots & \ddots & \ddots \end{bmatrix}. \tag{2.40}$$

Here, the first block row corresponds to a VAR(0) model, the second block row corresponds to a VAR(1) model and so on. By applying (2.40) to the pseudo-observations in (2.31), the transformed system of observation equations

$$\mathbf{0} = \bar{\mathbf{\Phi}}\Delta\mathbf{x} + \mathbf{w}, \qquad \mathbf{w} \sim \mathcal{N}(\mathbf{0}, \bar{\mathbf{\Sigma}}_{\mathbf{w}}), \tag{2.41}$$

with

$$\bar{\boldsymbol{\Sigma}}_{\mathbf{w}} = \begin{bmatrix} \boldsymbol{\Sigma}_{\mathbf{w}}^{(0)} & & & & & & \\ & \boldsymbol{\Sigma}_{\mathbf{w}}^{(1)} & & & & & \\ & & \boldsymbol{\Sigma}_{\mathbf{w}}^{(2)} & & & & \\ & & & \boldsymbol{\Sigma}_{\mathbf{w}}^{(3)} & & & \\ & & & & \boldsymbol{\Sigma}_{\mathbf{w}}^{(3)} & & \\ & & & & & \ddots & \end{bmatrix} \tag{2.42}$$

is obtained. It is briefly noted that the equality $\bar{\boldsymbol{\Sigma}}_{\mathbf{w}} = \bar{\boldsymbol{\Phi}}\boldsymbol{\Sigma}_{\mathbf{v}}\bar{\boldsymbol{\Phi}}^T$ only holds if $\mathbf{v}$ is a VAR($p_{\max}$) process, otherwise, if the process order is higher than $p_{\max}$, it is an approximation. From a computational perspective, the VAR model representation of $\boldsymbol{\Sigma}_{\mathbf{v}}$ has the advantage that the normal equation coefficients matrix

$$\mathbf{R} = \bar{\boldsymbol{\Phi}}^T\bar{\boldsymbol{\Sigma}}_{\mathbf{w}}^{-1}\bar{\boldsymbol{\Phi}} \tag{2.43}$$

arising from (2.41), is block banded with a bandwidth of $p_{\max}$. When deriving daily gravity field snapshots for the whole GRACE time-span from 2002-04 to 2017-06, this results in a reduction of required in-core memory by 99.86% for $p_{\max} = 3$, if sparsity of the normal equation matrix is considered. Furthermore, through the inclusion of the shorter AR models with $p = \{0, \dots, p_{\max} - 1\}$ the inverse of (2.43) is also block Toeplitz, thus satisfying the assumption of a stationary process. The combined system of normal equations using (2.41) as pseudo-observations is then given by

$$(\mathbf{N} + \bar{\boldsymbol{\Phi}}^T\bar{\boldsymbol{\Sigma}}_{\mathbf{w}}^{-1}\bar{\boldsymbol{\Phi}})\Delta\hat{\mathbf{x}} = \mathbf{n}. \tag{2.44}$$

When processing the satellite observations required for the assembly of $\mathbf{N}$ and $\mathbf{n}$, each observation taken will have to be identified with an epoch. For example, when daily gravity field estimates are of interest, the natural choice will be to assign all measurements taken in interval [00:00, 24:00) to the corresponding epoch with reference time at 12:00. By neglecting temporal correlations of the observations across interval boundaries, the observation equations for each epoch i

$$\Delta\mathbf{l}_i = \mathbf{A}_i\Delta\mathbf{x}_i + \mathbf{e}_i, \qquad \mathbf{e}_i \sim \mathcal{N}(\mathbf{0}, \boldsymbol{\Sigma}_{\mathbf{l}_i}). \tag{2.45}$$

may then be computed independently. When assembling these epoch-wise observation equations for all epochs $i = \{0, \dots, N-1\}$ ascending in time, the result is a block diagonal normal equation matrix $\mathbf{N}$, with the diagonal blocks $\mathbf{N}_i = \mathbf{A}_i^T\boldsymbol{\Sigma}_{\mathbf{l}_i}^{-1}\mathbf{A}_i$. It is briefly noted that for epochs where no satellite observations are available, the corresponding diagonal block will be zero, as the introduced pseudo-observations require a constant sampling. This implies that in practical applications, where data gaps occur, $\mathbf{N}$ must be assumed positive semi-definite and thus not invertible.

As previously mentioned, the normal equation matrix of the prior information $\mathbf{R}$ is block banded with bandwidth $p_{\max}$. This follows from the structure of (2.40). Since $\bar{\boldsymbol{\Phi}}$ is a lower triangular matrix in which only the first $p_{\max}$ subdiagonal blocks are non-zero, the sparsity structure of $\bar{\boldsymbol{\Phi}}$ is given by

$$\bar{\boldsymbol{\Phi}}_{mn} \neq \mathbf{0} \iff m \in \{n, \dots, n + p_{\max}\}. \tag{2.46}$$

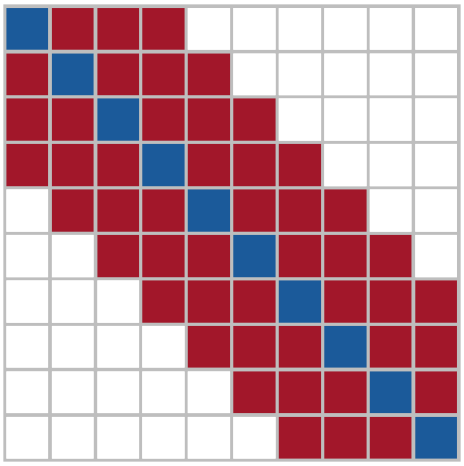

Figure 2.1.: Sparsity structure of the combined system of normal equations for $N = 10$ and $p_{\max} = 3$. Red squares indicate blocks only non-zero in $\mathbf{R}$, while blue squares indicate blocks which are non-zero in both $\mathbf{N}$ and $\mathbf{R}$.

For the regularization matrix $\mathbf{R}$, this means that its blocks

$$\mathbf{R}_{ij} = \sum_{k=j}^{\min\{j+p_{\max},N-1\}} \bar{\mathbf{\Phi}}_{ki}^T \bar{\mathbf{\Sigma}}_{\mathbf{w}_{kk}}^{-1} \bar{\mathbf{\Phi}}_{kj} \tag{2.47}$$

are only non-zero for $|j - i| \leq p_{\max}$. This structure is retained after the combination with observation information, because the daily normal equation coefficient matrices $\mathbf{N}_i$ are only added to the main diagonal.

The solution to (2.44) will in practice be computed through an in-place Cholesky decomposition, followed by forward and back substitution. This means that the system of equations is solved in three steps. First, the coefficient matrix is decomposed into its upper triangular Cholesky factor $\mathbf{W}$ with

$$(\mathbf{N} + \bar{\mathbf{\Phi}}^T \bar{\mathbf{\Sigma}}_{\mathbf{w}}^{-1} \bar{\mathbf{\Phi}}) = \mathbf{W}^T \mathbf{W}. \tag{2.48}$$

Then, an intermediate solution $\mathbf{r}$ is computed by solving the triangular system of equations

$$\mathbf{W}^T \mathbf{r} = \mathbf{n} \tag{2.49}$$

through forward substitution. Finally, the estimated parameters are computed by solving

$$\mathbf{W} \Delta\hat{\mathbf{x}} = \mathbf{r}, \tag{2.50}$$

through back substitution. Analogous steps are performed if the lower triangular Cholesky factor $\mathbf{L}$ is computed. These operations do not change the sparsity structure of the matrix, thus no additional in-core memory is required. However, if in addition to the estimated gravity field variations $\Delta\hat{\mathbf{x}}$, the covariance matrix of the estimated parameters $\hat{\mathbf{\Sigma}}_{\Delta\hat{\mathbf{x}}}$ is of interest, the normal equation matrix needs to be inverted. Due to the

Toeplitz-structure of the prior information covariance matrix, the result of this operation will be dense, which leads to excessive additional memory requirements. Therefore, an incomplete inverse, which retains the sparsity structure of the original matrix is desired. Fortunately, there exist efficient recursive algorithms to compute the inverse of block banded, symmetric matrices based on its Cholesky factor (e.g., Asif & Moura, 2005, cf. Appendix B), which operate in-place.

2.3. Relation between least-squares adjustment and Kalman smoother

In this section, the relation of the least-squares adjustment (2.31) to the Kalman smoother approach introduced by Kurtenbach et al. (2012) will be outlined. Since the Kalman smoother approach formulates the determination of high-frequency gravity field variations as a discrete state estimation problem, some fundamental concepts and notations will be outlined first.

While the least-squares adjustment representation of the smoothing problem allows for an arbitrary VAR model order, the fixed interval smoother considers only correlations between consecutive epochs. Thus, the linear dynamic system

$$\begin{aligned} \mathbf{l}_i &= \mathbf{A}_i\mathbf{x}_i + \mathbf{e}_i & \mathbf{e}_i &\sim \mathcal{N}(\mathbf{0}, \boldsymbol{\Sigma}_{\mathbf{l}_i}) \\ \mathbf{x}_i &= \mathbf{B}\mathbf{x}_{i-1} + \mathbf{w}_i & \mathbf{w}_i &\sim \mathcal{N}(\mathbf{0}, \mathbf{Q}) \end{aligned} \tag{2.51}$$

is considered. In (2.51), the VAR(1) model coefficient $\mathbf{B} = \boldsymbol{\Phi}_1^{(1)}$ and the corresponding white noise covariance $\mathbf{Q} = \boldsymbol{\Sigma}_{\mathbf{w}}^{(1)}$ is introduced, to match the notation of Kurtenbach et al. (2012). The sought after state in the application at hand is the gravity field correction $\Delta\mathbf{x}_i$ at a certain epoch i. For brevity's sake, Δ has been omitted for both state and observations in (2.51) and the following derivations, however still only parameter corrections are considered, except where explicitly stated otherwise.

Depending on whether observations $\mathbf{l}_j$ from the past ($j < i$), past and present ($j \leq i$) or the future ($j > i$) are used to determine $\mathbf{x}_i$, state estimation can be classified as:

Prediction A state estimate for epoch i is called predicted if only observation information from epochs $j < i$, i.e. the past, is used. Predicted values will be indicated with a "$-$" superscript, e.g., $\mathbf{x}_i^-$.

Filtering In a filtered state estimate for epoch i, all observations of epoch $j \leq i$ are incorporated in the estimation process, thus knowledge of past and present is required. Filtered values will be indicated with a "$+$" superscript, e.g. $\mathbf{x}_i^+$.

Smoothing Smoothing additionally incorporates measurement information from epochs $j > i$ for the state estimate of epoch i. Smoothed values will be indicated by an "s" superscript, e.g., $\mathbf{x}_i^s$. While the requirement for measurements from the future does in principle exclude smoothing algorithms from real-time applications, the additional information improves state estimates in post-processing or offline applications.

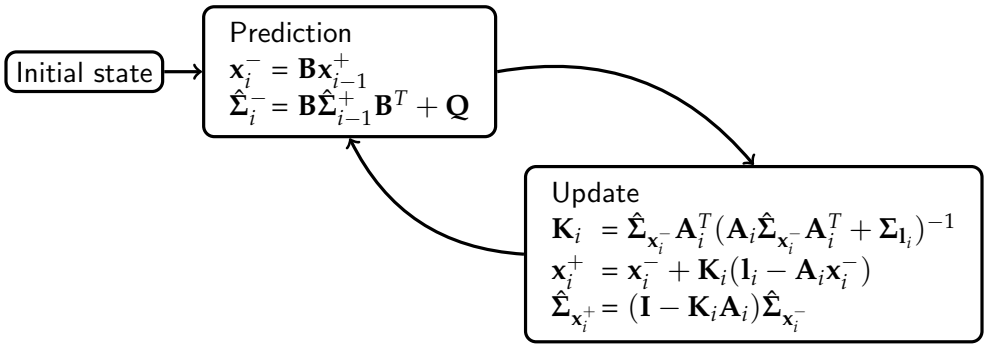

Figure 2.2.: Schematic principle of the two-step Kalman filter procedure.

The concepts of prediction and filtering naturally go hand-in-hand and are most prominently realized in the Kalman filter (Kalman, 1960). There, prediction constitutes the time update which propagates the current state estimate and its covariance to the next epoch. Filtering is then performed by improving the predicted state and its covariance matrix using the observations taken the current epoch during the measurement update. This two-step procedure has to be initialized with the so-called initial state $\mathbf{x}_{-1}^+$ and the initial state covariance $\mathbf{\Sigma}_{-1}^+$, from which the first prediction is made. A schematic of the prediction-update procedure can be found in Figure 2.2. During the prediction step, which is given by

$$\begin{aligned} \mathbf{x}_i^- &= \mathbf{B}\mathbf{x}_{i-1}^+ \\ \hat{\mathbf{\Sigma}}_{\mathbf{x}_i^-} &= \mathbf{B}\hat{\mathbf{\Sigma}}_{\mathbf{x}_{i-1}^+}\mathbf{B}^T + \mathbf{Q} \end{aligned} \tag{2.52}$$

the state transition matrix $\mathbf{B}$ is used to propagate the updated state from the previous epoch. Concurrently, the covariance matrix of the predicted state is computed through variance propagation. The update step

$$\begin{aligned} \mathbf{K}_i &= \hat{\mathbf{\Sigma}}_{\mathbf{x}_i^-}\mathbf{A}_i^T(\mathbf{A}_i\hat{\mathbf{\Sigma}}_{\mathbf{x}_i^-}\mathbf{A}_i^T + \mathbf{\Sigma}_{\mathbf{l}_i})^{-1} \\ \mathbf{x}_i^+ &= \mathbf{x}_i^- + \mathbf{K}_i(\mathbf{l}_i - \mathbf{A}_i\mathbf{x}_i^-) \\ \hat{\mathbf{\Sigma}}_{\mathbf{x}_i^+} &= (\mathbf{I} - \mathbf{K}_i\mathbf{A}_i)\hat{\mathbf{\Sigma}}_{\mathbf{x}_i^-} \end{aligned} \tag{2.53}$$

starts with the computation of the Kalman gain matrix $\mathbf{K}_i$. This matrix determines the amount the innovation vector $\mathbf{d}_i = \mathbf{l}_i - \mathbf{A}_i\mathbf{x}_i^-$ corrects the predicted state. Then, the predicted state is corrected to yield the updated state for this epoch. Finally, the covariance matrix of the updated state is computed (e.g., Gelb, 1974).

Smoothing can further be subdivided into whether a single epoch, an epoch with a fixed time lag or all epochs in a specified interval are improved with epochs from the future. Fixed-point smoothing aims at improving the state estimate of a single epoch with newly available observations. Fixed-lag smoothing improves the state estimate of epochs h time steps in the past. This method can be useful in operational application where a higher latency is acceptable. Finally, fixed-interval smoothing improves the state estimates of all epochs in a certain interval with all observations available. In principle, this aligns with the minimum-variance property of the least-squares adjustment, which

in fact yields identical state estimates if the initial state is chosen appropriately. A popular implementation of a fixed-interval smoothing is the Rauch-Tung-Striebel (RTS) smoother (Rauch, Striebel, & Tung, 1965), which operates on the Kalman filter output and recursively improves the state estimates from the last to the first epoch. According to Simon (2006), the smoothed state for epoch i and its covariance matrix is given by

$$\begin{aligned} \mathbf{x}_i^s &= \mathbf{x}_i^+ + \mathbf{W}_i(\mathbf{x}_{i+1}^s - \mathbf{x}_{i+1}^-) \\ \hat{\mathbf{\Sigma}}_{\mathbf{x}_i^s} &= \hat{\mathbf{\Sigma}}_{\mathbf{x}_i^+} - \mathbf{W}_i(\hat{\mathbf{\Sigma}}_{\mathbf{x}_{i+1}^-} - \hat{\mathbf{\Sigma}}_{\mathbf{x}_{i+1}^s})\mathbf{W}_i^T \end{aligned} \tag{2.54}$$

with

$$\mathbf{W}_i = \hat{\mathbf{\Sigma}}_{\mathbf{x}_i^+}\mathbf{B}^T(\mathbf{Q} + \mathbf{B}\hat{\mathbf{\Sigma}}_{\mathbf{x}_i^+}\mathbf{B}^T)^{-1}. \tag{2.55}$$

To show the equivalence of the fixed interval smoother with the least squares estimate (2.31), it is beneficial to first represent the filtering problem as a least squares adjustment.

The Kalman filter aims at providing the optimal state estimate $\mathbf{x}_i^+$ using observations $\mathbf{l}_i$ taken at the same epoch and the estimate $\mathbf{x}_{i-1}^+$ of the previous epoch, while incorporating the process model $\mathbf{B}$. These three components can be used to formulate the least squares adjustment

$$\begin{bmatrix} \mathbf{l}_i \\ \mathbf{0} \\ \mathbf{x}_{i-1}^+ \end{bmatrix} = \begin{bmatrix} & \mathbf{A}_i \\ \mathbf{B} & -\mathbf{I} \\ \mathbf{I} & \end{bmatrix} \begin{bmatrix} \mathbf{x}_{i-1} \\ \mathbf{x}_i \end{bmatrix} + \begin{bmatrix} \mathbf{e}_i \\ \mathbf{w}_i \\ \mathbf{s}_{i-1} \end{bmatrix}, \qquad \begin{bmatrix} \mathbf{e}_i \\ \mathbf{w}_i \\ \mathbf{s}_{i-1} \end{bmatrix} \sim \mathcal{N}\left(\begin{bmatrix} \mathbf{0} \\ \mathbf{0} \\ \mathbf{0} \end{bmatrix}, \begin{bmatrix} \mathbf{\Sigma}_{\mathbf{l}_i} & & \\ & \mathbf{Q} & \\ & & \hat{\mathbf{\Sigma}}_{\mathbf{x}_{i-1}^+} \end{bmatrix} \right), \tag{2.56}$$

where the observation residual $\mathbf{e}_i$, the prediction error $\mathbf{w}_i$ and the estimation error of the previous epoch $\mathbf{s}_{i-1}$ are minimized (Saltzmann, 1993). Forming the system of normal equations from (2.56) yields

$$\begin{bmatrix} \mathbf{B}^T\mathbf{Q}^{-1}\mathbf{B} + \hat{\mathbf{\Sigma}}_{\mathbf{x}_{i-1}^+}^{-1} & -\mathbf{B}^T\mathbf{Q}^{-1} \\ -\mathbf{Q}^{-1}\mathbf{B} & \mathbf{N}_i + \mathbf{Q}^{-1} \end{bmatrix} \begin{bmatrix} \mathbf{x}_{i-1}^s \\ \mathbf{x}_i^+ \end{bmatrix} = \begin{bmatrix} \hat{\mathbf{\Sigma}}_{\mathbf{x}_{i-1}^+}^{-1}\mathbf{x}_{i-1}^+ \\ \mathbf{n}_i \end{bmatrix}. \tag{2.57}$$

Analogous to a standard least squares adjustment, the solution to this system of normal equations is an estimate $\mathbf{x}_{i-1}^s$, $\mathbf{x}_i^+$ of the true values $\mathbf{x}_{i-1}$ and $\mathbf{x}_i$. The state estimate for epoch i is denoted as "filtered" because no observations $\mathbf{l}_j$ with $j > i$ are used in its determination. Consequently, the state estimate for epoch $i-1$ is donated as "smoothed" because it also depends on $\mathbf{l}_i$. Since in the filtering problem only the current epoch is of interest, the parameters corresponding to epoch $i-1$ are eliminated on the normal equation level following (2.25):

$$\begin{aligned} &[\mathbf{N}_i + \mathbf{Q}^{-1} - \mathbf{Q}^{-1}\mathbf{B}(\mathbf{B}^T\mathbf{Q}^{-1}\mathbf{B} + \hat{\mathbf{\Sigma}}_{\mathbf{x}_{i-1}^+}^{-1})^{-1}\mathbf{B}^T\mathbf{Q}^{-1}]\mathbf{x}_i^+ \\ &\qquad = \mathbf{n}_i - \mathbf{Q}^{-1}\mathbf{B}(\mathbf{B}^T\mathbf{Q}^{-1}\mathbf{B} + \hat{\mathbf{\Sigma}}_{\mathbf{x}_{i-1}^+}^{-1})^{-1}\hat{\mathbf{\Sigma}}_{\mathbf{x}_{i-1}^+}^{-1}\mathbf{x}_{i-1}^+. \end{aligned} \tag{2.58}$$

This expression can be simplified by applying the matrix inversion identities (A.11) and (A.12) to the left- and right hand side respectively. The resulting system of normal equations

$$[\mathbf{N}_i + (\mathbf{Q} + \mathbf{B}\hat{\mathbf{\Sigma}}_{\mathbf{x}_{i-1}^+}\mathbf{B}^T)^{-1}]\mathbf{x}_i^+ = \mathbf{n}_i + (\mathbf{Q} + \mathbf{B}\hat{\mathbf{\Sigma}}_{\mathbf{x}_{i-1}^+}\mathbf{B}^T)^{-1}\mathbf{B}\mathbf{x}_{i-1}^+, \tag{2.59}$$

then serves as basis for the derivation of both, the Kalman filter prediction- and update steps. It is briefly noted that this representation is closely related to the information form of the Kalman filter (Verhaegen & Van Dooren, 1986). Considering the case where state $\mathbf{x}_i$ is solely determined through information from the previous epoch, either during the prediction step of the time update, before observation information will be incorporated, or if no observations are available, the estimated state will be a prediction. This can equivalently be interpreted as using observations with zero weight in (2.59), where consequently both $\mathbf{N}_i$ and $\mathbf{n}_i$ vanish. The predicted state $\mathbf{x}_i^-$ and its covariance matrix $\hat{\mathbf{\Sigma}}_{\mathbf{x}_i^-}$ are then given by

$$\mathbf{x}_i^- = \mathbf{B}\mathbf{x}_{i-1}^+, \quad \hat{\mathbf{\Sigma}}_{\mathbf{x}_i^-} = \mathbf{Q} + \mathbf{B}\hat{\mathbf{\Sigma}}_{\mathbf{x}_{i-1}^+}\mathbf{B}^T. \tag{2.60}$$

Once observations for epoch i are available, (2.59) constitutes the measurement update of the Kalman filter, which yields the updated state $\mathbf{x}_i^+$. By substituting the predicted quantities from (2.60) and expanding $\mathbf{N}_i$ and $\mathbf{n}_i$, an abbreviated form

$$[\mathbf{A}_i^T\mathbf{\Sigma}_{\mathbf{l}_i}^{-1}\mathbf{A}_i + \hat{\mathbf{\Sigma}}_{\mathbf{x}_i^-}^{-1}]\mathbf{x}_i^+ = \mathbf{A}_i^T\mathbf{\Sigma}_{\mathbf{l}_i}^{-1}\mathbf{l}_i + \hat{\mathbf{\Sigma}}_{\mathbf{x}_i^-}^{-1}\mathbf{x}_i^- \tag{2.61}$$

of (2.59) is obtained. The solution to this system of equations is given by

$$\mathbf{x}_i^+ = [\mathbf{A}_i^T\mathbf{\Sigma}_{\mathbf{l}_i}^{-1}\mathbf{A}_i + \hat{\mathbf{\Sigma}}_{\mathbf{x}_i^-}^{-1}]^{-1}\mathbf{A}_i^T\mathbf{\Sigma}_{\mathbf{l}_i}^{-1}\mathbf{l}_i + [\mathbf{A}_i^T\mathbf{\Sigma}_{\mathbf{l}_i}^{-1}\mathbf{A}_i + \hat{\mathbf{\Sigma}}_{\mathbf{x}_i^-}^{-1}]^{-1}\hat{\mathbf{\Sigma}}_{\mathbf{x}_i^-}^{-1}\mathbf{x}_i^-. \tag{2.62}$$

Applying the matrix identities (A.12) and (A.11) to the first and second right-hand-side term in (2.62) respectively, yields the well-known expression of the measurement update

$$\mathbf{x}_i^+ = \mathbf{x}_i^- + \underbrace{\hat{\mathbf{\Sigma}}_{\mathbf{x}_i^-}\mathbf{A}_i^T[\mathbf{A}_i\hat{\mathbf{\Sigma}}_{\mathbf{x}_i^-}\mathbf{A}_i^T + \mathbf{\Sigma}_{\mathbf{l}_i}]^{-1}}_{=\mathbf{K}_i}(\mathbf{l}_i - \mathbf{A}_i\mathbf{x}_i^-), \tag{2.63}$$

where $\mathbf{K}_i$ is the so-called Kalman gain matrix and $\mathbf{l}_i - \mathbf{A}_i\mathbf{x}_i^-$ is the Kalman innovation for epoch i. It is briefly noted that condensed observation equations

$$\begin{bmatrix}\mathbf{l}_i\\ \mathbf{x}_i^-\end{bmatrix} = \begin{bmatrix}\mathbf{A}_i\\ \mathbf{I}_i\end{bmatrix}\mathbf{x}_i + \begin{bmatrix}\mathbf{e}_i\\ \mathbf{u}_i\end{bmatrix}, \quad \begin{bmatrix}\mathbf{e}_i\\ \mathbf{u}_i\end{bmatrix} \sim \mathcal{N}(\begin{bmatrix}\mathbf{0}\\ \mathbf{0}\end{bmatrix}, \begin{bmatrix}\mathbf{\Sigma}_{\mathbf{l}_i} & \\ & \hat{\mathbf{\Sigma}}_{\mathbf{x}_i^-}\end{bmatrix}) \tag{2.64}$$

also leads to the system of normal equations (2.57), which can easily be verified.

While the state of the preceding epoch was eliminated for the derivation of the Kalman filter, retaining and possibly expanding the number of previous epochs in (2.56) allows the derivation of the smoother equations. Since all epochs are connected through the process model $\mathbf{x}_i = \mathbf{B}\mathbf{x}_{i-1} + \mathbf{w}_i$, any new information represented by additional observations can be used to improve estimates from the past. By extending (2.56) to epochs $j < i$, the estimation error of these epochs is also minimized. The Rauch-Tung-Striebel (RTS, Rauch et al., 1965) smoother used by Kurtenbach et al. (2012) can be derived by extending (2.57) to also include the epoch $i-2$. The first line of the resulting system of normal equations

$$\begin{bmatrix}\mathbf{B}^T\mathbf{Q}^{-1}\mathbf{B} + \hat{\mathbf{\Sigma}}_{\mathbf{x}_{i-2}^+}^{-1} & -\mathbf{B}^T\mathbf{Q}^{-1} & \\ -\mathbf{Q}^{-1}\mathbf{B} & \mathbf{B}^T\mathbf{Q}^{-1}\mathbf{B} + \hat{\mathbf{\Sigma}}_{\mathbf{x}_{i-1}^+}^{-1} & -\mathbf{B}^T\mathbf{Q}^{-1}\\ & -\mathbf{Q}^{-1}\mathbf{B} & \mathbf{N}_i + \mathbf{Q}^{-1}\end{bmatrix}\begin{bmatrix}\mathbf{x}_{i-2}^s\\ \mathbf{x}_{i-1}^s\\ \mathbf{x}_i^+\end{bmatrix} = \begin{bmatrix}\hat{\mathbf{\Sigma}}_{\mathbf{x}_{i-2}^+}^{-1}\mathbf{x}_{i-2}^+\\ \hat{\mathbf{\Sigma}}_{\mathbf{x}_{i-1}^+}^{-1}\mathbf{x}_{i-1}^+\\ \mathbf{n}_i\end{bmatrix}, \tag{2.65}$$

will be the starting point of this derivation. Multiplying the state estimates with the first line of the system of equations leads to

$$(\mathbf{B}^T\mathbf{Q}^{-1}\mathbf{B} + \hat{\mathbf{\Sigma}}^{-1}_{\mathbf{x}^+_{i-2}})\mathbf{x}^s_{i-2} - \mathbf{B}^T\mathbf{Q}^{-1}\mathbf{x}^s_{i-1} = \hat{\mathbf{\Sigma}}^{-1}_{\mathbf{x}^+_{i-2}}\mathbf{x}^+_{i-2}. \tag{2.66}$$

Then, after multiplying the equation with $(\mathbf{B}^T\mathbf{Q}^{-1}\mathbf{B} + \hat{\mathbf{\Sigma}}^{-1}_{\mathbf{x}^+_{i-2}})^{-1}$,

$$\mathbf{x}^s_{i-2} = (\mathbf{B}^T\mathbf{Q}^{-1}\mathbf{B} + \hat{\mathbf{\Sigma}}^{-1}_{\mathbf{x}^+_{i-2}})^{-1}\mathbf{B}^T\mathbf{Q}^{-1}\mathbf{x}^s_{i-1} + (\mathbf{B}^T\mathbf{Q}^{-1}\mathbf{B} + \hat{\mathbf{\Sigma}}^{-1}_{\mathbf{x}^+_{i-2}})^{-1}\hat{\mathbf{\Sigma}}^{-1}_{\mathbf{x}^+_{i-2}}\mathbf{x}^+_{i-2} \tag{2.67}$$

is obtained. The first term on the right-hand side of (2.67) can be rewritten as

$$\hat{\mathbf{\Sigma}}_{\mathbf{x}^+_{i-2}}\mathbf{B}^T(\mathbf{Q} + \mathbf{B}\hat{\mathbf{\Sigma}}_{\mathbf{x}^+_{i-2}}\mathbf{B}^T)^{-1}\mathbf{x}^s_{i-1} = \mathbf{W}_{i-2}\mathbf{x}^s_{i-1}, \tag{2.68}$$

by applying the matrix identity (A.12). Likewise, by applying (A.11), the second term can be expressed as

$$[\hat{\mathbf{\Sigma}}_{\mathbf{x}^+_{i-2}} - \hat{\mathbf{\Sigma}}_{\mathbf{x}^+_{i-2}}\mathbf{B}^T(\mathbf{Q} + \mathbf{B}\hat{\mathbf{\Sigma}}_{\mathbf{x}^+_{i-2}}\mathbf{B}^T)^{-1}\mathbf{B}\hat{\mathbf{\Sigma}}_{\mathbf{x}^+_{i-2}}]\hat{\mathbf{\Sigma}}^{-1}_{\mathbf{x}^+_{i-2}}\mathbf{x}^+_{i-2} \tag{2.69}$$

which reduces to

$$\mathbf{x}^+_{i-2} - \mathbf{W}_{i-2}\mathbf{x}^-_{i-1}. \tag{2.70}$$

Combining (2.68) and (2.70), finally yields the smoothed state at epoch $i-2$ as a function of the smoothed and predicted state of the previous epoch, and the filtered state of the current epoch

$$\mathbf{x}^s_{i-2} = \mathbf{x}^+_{i-2} + \mathbf{W}_{i-2}(\mathbf{x}^s_{i-1} - \mathbf{x}^-_{i-1}), \tag{2.71}$$

which is exactly the RTS formulation of the smoothing problem (cf. Rauch et al., 1965). This recursive algorithm acts as a backward pass through the time series of (forward) filtered states, starting at the last epoch $N-1$. The smoother is initialized with the Kalman filter solution at $N-1$, thus $\mathbf{x}^s_{N-1} = \mathbf{x}^+_{N-1}$ (cf. also Gelb, 1974). Hence, the computationally very efficient Kalman filter algorithm is sufficient for operational applications if only the last epoch is of interest.

To show that the least squares adjustment (2.44) is equivalent to the Kalman smoother, it is verified that the smoothed state $\mathbf{x}^s_i$ is a solution to the system of normal equations for all epochs i. The reasoning behind this approach is that since the normal equation matrix is required to be positive definite and therefore invertible, the system of normal equations has a unique solution. Thus, any vector that satisfies (2.44) is the least squares solution to the constrained adjustment problem. As a preliminary step, the structure of the normal equation coefficient matrix in (2.44) is explicitly derived for a $p_{\max} = 1$. If only a VAR(1) model is considered, the matrices $\bar{\mathbf{\Phi}}$ and $\bar{\mathbf{\Sigma}}_{\mathbf{w}}$ simplify to

$$\bar{\mathbf{\Phi}} = \begin{bmatrix} \mathbf{I} & & & & \\ -\mathbf{B} & \mathbf{I} & & & \\ & -\mathbf{B} & \mathbf{I} & & \\ & & \ddots & \ddots & \\ & & & -\mathbf{B} & \mathbf{I} \end{bmatrix} \quad \text{and} \quad \bar{\mathbf{\Sigma}}_{\mathbf{w}} = \begin{bmatrix} \mathbf{\Sigma}^{(0)}_{\mathbf{w}} & & & & \\ & \mathbf{Q} & & & \\ & & \mathbf{Q} & & \\ & & & \ddots & \\ & & & & \mathbf{Q} \end{bmatrix}. \tag{2.72}$$

This sparsity structure of $\bar{\mathbf{\Phi}}$ means that $\mathbf{R}$ matrix will be block tridiagonal. For an arbitrary row $i \in 1, \ldots, N-2$ only the blocks $\mathbf{R}_{i,i-1}$, $\mathbf{R}_{i,i}$, and $\mathbf{R}_{i,i+1}$ will therefore be non-zero. Evaluating the general expression of the blocks of $\mathbf{R}$ for $p_{\max} = 1$,

$$\mathbf{R}_{ij} = \bar{\mathbf{\Phi}}_{ji}^T \bar{\mathbf{\Sigma}}_{\mathbf{w}_{jj}}^{-1} \bar{\mathbf{\Phi}}_{jj} + \bar{\mathbf{\Phi}}_{j+1,i}^T \bar{\mathbf{\Sigma}}_{\mathbf{w}_{j+1,j+1}}^{-1} \bar{\mathbf{\Phi}}_{j+1,j} \tag{2.73}$$

for $j \in \{i-1, i, i+1\}$ leads to

$$\mathbf{R}_{i,i-1} = -\mathbf{Q}^{-1}\mathbf{B}, \quad \mathbf{R}_{ii} = \mathbf{B}^T\mathbf{Q}^{-1}\mathbf{B} + \mathbf{Q}^{-1}, \quad \text{and} \quad \mathbf{R}_{i,i+1} = -\mathbf{B}^T\mathbf{Q}^{-1}. \tag{2.74}$$

Completing the system of normal equations with the normal equations of the satellite observations and the estimated parameter vector

$$\mathbf{N} = \begin{bmatrix} \mathbf{N}_0 & & & \\ & \mathbf{N}_1 & & \\ & & \ddots & \\ & & & \mathbf{N}_{N-1} \end{bmatrix}, \quad \mathbf{n} = \begin{bmatrix} \mathbf{n}_0 \\ \mathbf{n}_1 \\ \vdots \\ \mathbf{n}_{N-1} \end{bmatrix}, \quad \text{and} \quad \Delta\hat{\mathbf{x}} = \begin{bmatrix} \mathbf{x}_0^s \\ \mathbf{x}_1^s \\ \vdots \\ \mathbf{x}_{N-1}^+ \end{bmatrix} \tag{2.75}$$

yields the expression for a single block row i with

$$-\mathbf{Q}^{-1}\mathbf{B}\mathbf{x}_{i-1}^s + (\mathbf{B}^T\mathbf{Q}^{-1}\mathbf{B} + \mathbf{Q}^{-1} + \mathbf{N}_i)\mathbf{x}_i^s - \mathbf{B}^T\mathbf{Q}^{-1}\mathbf{x}_{i+1}^s = \mathbf{n}_i. \tag{2.76}$$

Then, $\mathbf{x}_{i-1}^s$ is substituted with the RTS solution for epoch $i-1$ in (2.76). and all terms containing $\mathbf{x}_i^s$, $\mathbf{x}_{i+1}^s$, $\mathbf{x}_i^-$, and $\mathbf{x}_i^+$ are combined, which leads to

$$\begin{aligned} &-(\mathbf{Q}^{-1} - \mathbf{Q}^{-1}\mathbf{B}\mathbf{W}_{i-1})\mathbf{x}_i^- + \\ &(\mathbf{B}^T\mathbf{Q}^{-1}\mathbf{B} + \mathbf{N}_i + \mathbf{Q}^{-1} - \mathbf{Q}^{-1}\mathbf{B}\mathbf{W}_{i-1})\mathbf{x}_i^s + \\ &\qquad -\mathbf{B}^T\mathbf{Q}^{-1}\mathbf{x}_{i+1}^s = \mathbf{n}_i. \end{aligned} \tag{2.77}$$

This expression can be further simplified by using (A.12) and (A.11), since

$$\begin{aligned} \mathbf{Q}^{-1} - \mathbf{Q}^{-1}\mathbf{B}\mathbf{W}_{i-1} &= \mathbf{Q}^{-1} - \mathbf{Q}^{-1}\mathbf{B}[\hat{\mathbf{\Sigma}}_{\mathbf{x}_{i-1}^+}\mathbf{B}^T(\mathbf{Q} + \mathbf{B}\hat{\mathbf{\Sigma}}_{\mathbf{x}_{i-1}^+}\mathbf{B}^T)^{-1}] \\ &= \mathbf{Q}^{-1} - \mathbf{Q}^{-1}\mathbf{B}(\hat{\mathbf{\Sigma}}_{\mathbf{x}_{i-1}^+}^{-1} + \mathbf{B}^T\mathbf{Q}^{-1}\mathbf{B})^{-1}\mathbf{B}^T\mathbf{Q}^{-1} \\ &= (\mathbf{Q} + \mathbf{B}\hat{\mathbf{\Sigma}}_{\mathbf{x}_{i-1}^+}\mathbf{B}^T)^{-1} = \hat{\mathbf{\Sigma}}_{\mathbf{x}_i^-}^{-1}. \end{aligned} \tag{2.78}$$

From (2.59) it is found that $\mathbf{N}_i = \hat{\mathbf{\Sigma}}_{\mathbf{x}_i^+}^{-1} - \hat{\mathbf{\Sigma}}_{\mathbf{x}_i^-}^{-1}$ and $\mathbf{n}_i = \hat{\mathbf{\Sigma}}_{\mathbf{x}_i^+}^{-1}\mathbf{x}_i^+ - \hat{\mathbf{\Sigma}}_{\mathbf{x}_i^-}^{-1}\mathbf{x}_i^-$. Substituting this into (2.77) then yields

$$\begin{aligned} &-\hat{\mathbf{\Sigma}}_{\mathbf{x}_i^-}^{-1}\mathbf{x}_i^- + (\mathbf{B}^T\mathbf{Q}^{-1}\mathbf{B} + \hat{\mathbf{\Sigma}}_{\mathbf{x}_i^+}^{-1})\mathbf{x}_i^s + \\ &\qquad -\mathbf{B}^T\mathbf{Q}^{-1}\mathbf{x}_{i+1}^s = \hat{\mathbf{\Sigma}}_{\mathbf{x}_i^+}^{-1}\mathbf{x}_i^+ - \hat{\mathbf{\Sigma}}_{\mathbf{x}_i^-}^{-1}\mathbf{x}_i^-. \end{aligned} \tag{2.79}$$

In the next step, through substitution of $\mathbf{x}_i^s$ with the RTS solution (2.71) for the corresponding epoch i,

$$\begin{aligned} &-\hat{\mathbf{\Sigma}}_{\mathbf{x}_i^-}^{-1}\mathbf{x}_i^- + (\mathbf{B}^T\mathbf{Q}^{-1}\mathbf{B} + \hat{\mathbf{\Sigma}}_{\mathbf{x}_i^+}^{-1})\mathbf{x}_i^+ - \mathbf{B}^T\mathbf{Q}^{-1}\mathbf{x}_{i+1}^- + \\ &\qquad +\mathbf{B}^T\mathbf{Q}^{-1}\mathbf{x}_{i+1}^s - \mathbf{B}^T\mathbf{Q}^{-1}\mathbf{x}_{i+1}^s = \hat{\mathbf{\Sigma}}_{\mathbf{x}_i^+}^{-1}\mathbf{x}_i^+ - \hat{\mathbf{\Sigma}}_{\mathbf{x}_i^-}^{-1}\mathbf{x}_i^- \end{aligned} \tag{2.80}$$

is obtained. As can be seen the terms containing $\mathbf{x}_{i+1}^s$ cancel out. Expanding $(\mathbf{B}^T\mathbf{Q}^{-1}\mathbf{B} + \hat{\mathbf{\Sigma}}_{\mathbf{x}_i^+}^{-1})\mathbf{x}_i^+ - \mathbf{B}^T\mathbf{Q}^{-1}\mathbf{x}_{i+1}^-$ and using the definition of the predicted state, leaves

$$-\hat{\mathbf{\Sigma}}_{\mathbf{x}_i^-}^{-1}\mathbf{x}_i^- + \mathbf{B}^T\mathbf{Q}^{-1}\mathbf{x}_{i+1}^- + \hat{\mathbf{\Sigma}}_{\mathbf{x}_i^+}^{-1}\mathbf{x}_i^+ - \mathbf{B}^T\mathbf{Q}^{-1}\mathbf{x}_{i+1}^- = \hat{\mathbf{\Sigma}}_{\mathbf{x}_i^+}^{-1}\mathbf{x}_i^+ - \hat{\mathbf{\Sigma}}_{\mathbf{x}_i^-}^{-1}\mathbf{x}_i^-, \tag{2.81}$$

which further reduces to

$$-\hat{\mathbf{\Sigma}}_{\mathbf{x}_i^-}^{-1}\mathbf{x}_i^- + \hat{\mathbf{\Sigma}}_{\mathbf{x}_i^+}^{-1}\mathbf{x}_i^+ = \hat{\mathbf{\Sigma}}_{\mathbf{x}_i^+}^{-1}\mathbf{x}_i^+ - \hat{\mathbf{\Sigma}}_{\mathbf{x}_i^-}^{-1}\mathbf{x}_i^-, \tag{2.82}$$

as all terms containing $\mathbf{B}$ and $\mathbf{Q}$ cancel. This shows that for epochs $i \in \{1, \ldots, N-2\}$, the Kalman smoother is a solution to the system of normal equations.

Due to the block tridiagonal structure of (2.44), the first and last epoch have to be treated differently. First, the expression for the normal equation block row of the last epoch $i = N-1$,

$$-\mathbf{Q}^{-1}\mathbf{B}\mathbf{x}_{N-2}^s + (\mathbf{N}_{N-1} + \mathbf{Q}^{-1})\mathbf{x}_{N-1}^+ = \mathbf{n}_{N-1} \tag{2.83}$$

is derived from (2.73). In (2.83), the property that the last smoothed state is identical to the filtered state, $\mathbf{x}_{N-1}^s = \mathbf{x}_{N-1}^+$ is used (cf. Gelb, 1974). Substituting (2.71) for the smoothed state at epoch $N-2$ yields

$$-\mathbf{Q}^{-1}\mathbf{x}_{N-1}^- - \mathbf{Q}^{-1}\mathbf{B}\mathbf{W}_{N-2}\mathbf{x}_{N-1}^+ + \mathbf{Q}^{-1}\mathbf{B}\mathbf{W}_{N-2}\mathbf{x}_{N-1}^- + (\mathbf{N}_{N-1} + \mathbf{Q}^{-1})\mathbf{x}_{N-1}^+ = \mathbf{n}_{N-1}. \tag{2.84}$$

Through combining terms with $\mathbf{x}_{N-1}^-$ and $\mathbf{x}_{N-1}^+$

$$-(\mathbf{Q}^{-1} - \mathbf{Q}^{-1}\mathbf{B}\mathbf{W}_{N-2})\mathbf{x}_{N-1}^- + (\mathbf{Q}^{-1} - \mathbf{Q}^{-1}\mathbf{B}\mathbf{W}_{N-2})\mathbf{x}_{N-1}^+ + \mathbf{N}_{N-1}\mathbf{x}_{N-1}^+ = \mathbf{n}_{N-1} \tag{2.85}$$

is obtained. Considering that $(\mathbf{Q}^{-1} - \mathbf{Q}^{-1}\mathbf{B}\mathbf{W}_{N-2}) = \hat{\mathbf{\Sigma}}_{\mathbf{x}_{N-1}^-}^{-1}$, this can be further simplified to

$$-\hat{\mathbf{\Sigma}}_{\mathbf{x}_{N-1}^-}^{-1}\mathbf{x}_{N-1}^- + \hat{\mathbf{\Sigma}}_{\mathbf{x}_{N-1}^-}^{-1}\mathbf{x}_{N-1}^+ + \mathbf{N}_{N-1}\mathbf{x}_{N-1}^+ = \mathbf{n}_{N-1}. \tag{2.86}$$

By substituting $\mathbf{N}_i = \hat{\mathbf{\Sigma}}_{\mathbf{x}_i^+}^{-1} - \hat{\mathbf{\Sigma}}_{\mathbf{x}_i^-}^{-1}$ and $\mathbf{n}_i = \hat{\mathbf{\Sigma}}_{\mathbf{x}_i^+}^{-1}\mathbf{x}_i^+ - \hat{\mathbf{\Sigma}}_{\mathbf{x}_i^-}^{-1}\mathbf{x}_i^-$ from (2.59), we again find that

$$-\hat{\mathbf{\Sigma}}_{\mathbf{x}_{N-1}^-}^{-1}\mathbf{x}_{N-1}^- + \hat{\mathbf{\Sigma}}_{\mathbf{x}_{N-1}^+}^{-1}\mathbf{x}_{N-1}^+ = \hat{\mathbf{\Sigma}}_{\mathbf{x}_{N-1}^+}^{-1}\mathbf{x}_{N-1}^+ - \hat{\mathbf{\Sigma}}_{\mathbf{x}_{N-1}^-}^{-1}\mathbf{x}_{N-1}^-. \tag{2.87}$$

Which shows that also the last epoch satisfies the assumption that the RTS smoother is a solution to (2.44). Finally, the first epoch of the least squares adjustment is treated. This epoch is of special interest, as it implicitly depends on the initial state of the Kalman filter $\mathbf{x}_{-1}^+$ and its covariance matrix $\mathbf{\Sigma}_{\mathbf{x}_{-1}^+}$. Evaluating (2.73) for $i = 0$ yields

$$(\mathbf{B}^T\mathbf{Q}^{-1}\mathbf{B} + \mathbf{\Sigma}_{\mathbf{w}}^{(0)^{-1}} + \mathbf{N}_0)\mathbf{x}_0^s - \mathbf{B}^T\mathbf{Q}^{-1}\mathbf{x}_1^s = \mathbf{n}_0. \tag{2.88}$$

After substituting the RTS smoother solution (2.71) for epochs 0 and 1 and some tedious matrix algebra it is found that

$$\mathbf{\Sigma}_{\mathbf{w}}^{(0)^{-1}}\mathbf{x}_0^s - \hat{\mathbf{\Sigma}}_{\mathbf{x}_0^-}^{-1}\mathbf{x}_0^s = \hat{\mathbf{\Sigma}}_{\mathbf{x}_0^-}^{-1}\mathbf{x}_0^-, \tag{2.89}$$

which can also be expressed as

$$[\hat{\mathbf{\Sigma}}_{\mathbf{x}_0^-}\mathbf{\Sigma}_{\mathbf{w}}^{(0)^{-1}} - \mathbf{I}]\mathbf{x}_0^s = \mathbf{x}_0^- = \mathbf{B}\mathbf{x}_{-1}^+. \tag{2.90}$$

It can be clearly seen that this equation is satisfied if $\hat{\mathbf{\Sigma}}_{\mathbf{x}_0^-} = \mathbf{\Sigma}_{\mathbf{w}}^{(0)}$ and $\mathbf{x}_0^- = \mathbf{0}$. The covariance matrix of the predicted state at epoch 0 is defined as $\mathbf{Q} + \mathbf{B}\mathbf{\Sigma}_{\mathbf{x}_{-1}^+}\mathbf{B}^T$. From the covariance structure of a VAR(1) process, it follows that

$$\mathbf{Q} = \mathbf{\Sigma}_{\mathbf{w}}^{(0)} - \mathbf{B}\mathbf{\Sigma}_{\mathbf{w}}^{(0)}\mathbf{B}^T, \tag{2.91}$$

(e.g., Lütkepohl, 2005). When substituted into the definition of the predicted state covariance matrix, this leads to

$$\hat{\mathbf{\Sigma}}_{\mathbf{x}_0^-} = \mathbf{\Sigma}_{\mathbf{w}}^{(0)} - \mathbf{B}\mathbf{\Sigma}_{\mathbf{w}}^{(0)}\mathbf{B}^T + \mathbf{B}\mathbf{\Sigma}_{\mathbf{x}_{-1}^+}\mathbf{B}^T \overset{!}{=} \mathbf{\Sigma}_{\mathbf{w}}^{(0)}. \tag{2.92}$$

Obviously, this equation is satisfied when the terms containing $\mathbf{B}$ vanish, which is the case when $\mathbf{\Sigma}_{\mathbf{x}_{-1}^+} = \mathbf{\Sigma}_{\mathbf{w}}^{(0)}$, which is the auto-covariance matrix of the process. This means that (2.44) can either be solved directly, or through a forward Kalman filter sweep followed by the application of the RTS smoothing algorithm, if the initial state and its covariance matrix is chosen as $\mathbf{x}_{-1}^+ = \mathbf{0}$ and $\mathbf{\Sigma}_{\mathbf{x}_{-1}^+} = \mathbf{\Sigma}_{\mathbf{w}}^{(0)}$ respectively. This choice of initial state is a quite natural one, as it is based on the properties of the process. As the process is required to be centered and wide-sense stationary, thus $\mathbf{x}_i \sim \mathcal{N}(\mathbf{0}, \mathbf{\Sigma}_{\mathbf{w}}^{(0)})$ holds true for all epochs i.

This equivalence of the optimal smoother and the least squares adjustment in (2.31) can also be seen from an algorithmic point of view. Since both approaches yield identical results, the forward-backward algorithm acts as an alternative solver for a symmetric, positive-definite, block tridiagonal system of equations.

2.3.1. Extension of the Kalman filter to VAR models of arbitrary order

As shown in Lütkepohl (2005), every VAR(p) model can be expressed as a VAR(1) model by extending the state vector. Thus, for each VAR(p) an equivalent VAR(1) model $\tilde{\mathbf{x}}_i = \tilde{\mathbf{B}}\tilde{\mathbf{x}}_{i-1} + \tilde{\mathbf{w}}_i$, with

$$\underbrace{\begin{bmatrix} \mathbf{x}_i \\ \mathbf{x}_{i-1} \\ \vdots \\ \mathbf{x}_{i-p+2} \\ \mathbf{x}_{i-p+1} \end{bmatrix}}_{=\tilde{\mathbf{x}}_i} = \underbrace{\begin{bmatrix} \mathbf{\Phi}_1^{(p)} & \mathbf{\Phi}_2^{(p)} & \cdots & \mathbf{\Phi}_{p-1}^{(p)} & \mathbf{\Phi}_p^{(p)} \\ \mathbf{I} & & \cdots & & \\ & \mathbf{I} & \cdots & & \\ & & \ddots & & \\ & & & \mathbf{I} & \end{bmatrix}}_{=\tilde{\mathbf{B}}} \underbrace{\begin{bmatrix} \mathbf{x}_{i-1} \\ \mathbf{x}_{i-2} \\ \vdots \\ \mathbf{x}_{i-p+1} \\ \mathbf{x}_{i-p} \end{bmatrix}}_{=\tilde{\mathbf{x}}_{i-1}} + \underbrace{\begin{bmatrix} \mathbf{w}_i \\ \mathbf{0} \\ \vdots \\ \mathbf{0} \\ \mathbf{0} \end{bmatrix}}_{=\tilde{\mathbf{w}}_i} \tag{2.93}$$

can be found. The key difference to an ordinary VAR(1) model is that the white noise vector $\tilde{\mathbf{w}}_i$ contains entries that are known to be zero, therefore it follows the distribution

$$\tilde{\mathbf{w}}_i \sim \mathcal{N}(\mathbf{0}, \tilde{\mathbf{Q}}), \tag{2.94}$$

with

$$\tilde{\mathbf{Q}} = \begin{bmatrix} \boldsymbol{\Sigma}_{\mathbf{w}}^{(p)} & \mathbf{0} & \cdots & \mathbf{0} & \mathbf{0} \\ \mathbf{0} & \mathbf{0} & \cdots & \mathbf{0} & \mathbf{0} \\ \vdots & \vdots & \ddots & \vdots & \vdots \\ \mathbf{0} & \mathbf{0} & \cdots & \mathbf{0} & \mathbf{0} \\ \mathbf{0} & \mathbf{0} & \cdots & \mathbf{0} & \mathbf{0} \end{bmatrix}. \tag{2.95}$$

This implies that the covariance matrix $\tilde{\mathbf{Q}}$ of the augmented white noise vector $\tilde{\mathbf{w}}_i$ is positive semidefinite and therefore not invertible. The observation equations corresponding to the augmented process model are

$$\mathbf{l}_i = \begin{bmatrix} \mathbf{A}_i & \mathbf{0} & \cdots & \mathbf{0} & \mathbf{0} \end{bmatrix} \begin{bmatrix} \mathbf{x}_i \\ \mathbf{x}_{i-1} \\ \vdots \\ \mathbf{x}_{i-p+2} \\ \mathbf{x}_{i-p+1} \end{bmatrix} + \mathbf{e}_i, \qquad \mathbf{e}_i \sim \mathcal{N}(\mathbf{0}, \boldsymbol{\Sigma}_{\mathbf{l}_i}), \tag{2.96}$$

or more concise $\mathbf{l}_i = \tilde{\mathbf{A}}_i \tilde{\mathbf{x}}_i + \mathbf{e}_i$. Similarly to the white noise covariance, the normal equation matrix computed from (2.96) will be positive semidefinite. From a practical point of view, the augmented linear dynamic system

$$\begin{aligned} \mathbf{l}_i &= \tilde{\mathbf{A}}_i \tilde{\mathbf{x}}_i + \mathbf{e}_i & \mathbf{e}_i &\sim \mathcal{N}(\mathbf{0}, \boldsymbol{\Sigma}_{\mathbf{l}_i}) \\ \tilde{\mathbf{x}}_i &= \tilde{\mathbf{B}} \tilde{\mathbf{x}}_{i-1} + \tilde{\mathbf{w}}_i & \tilde{\mathbf{w}}_i &\sim \mathcal{N}(\mathbf{0}, \tilde{\mathbf{Q}}) \end{aligned} \tag{2.97}$$

can be readily used in the Kalman filter and Kalman smoother equations. To obtain a state estimate identical to the solution of the system of normal equations (2.44) when using a VAR model of order $p_{\max}$, an appropriate choice of initial state as well as a special treatment of the first $p_{\max} - 1$ epochs is however necessary. Similar to the treatment of warmup effects in the pseudo-observations (2.40), VAR models of order $p \in \{1, \ldots, p_{\max} - 1\}$ are used to predict the first epochs. For example, the augmented VAR model used to predict $\tilde{\mathbf{x}}_0^-$ and $\hat{\boldsymbol{\Sigma}}_{\tilde{\mathbf{x}}_0^-}$ has the structure

$$\begin{bmatrix} \boldsymbol{\Phi}_1^{(1)} & \mathbf{0} & \cdots & \mathbf{0} & \mathbf{0} \\ \mathbf{I} & & \cdots & & \\ & \mathbf{I} & \cdots & & \\ & & \ddots & & \\ & & & \mathbf{I} & \end{bmatrix}, \begin{bmatrix} \boldsymbol{\Sigma}_{\mathbf{w}}^{(1)} & \mathbf{0} & \cdots & \mathbf{0} & \mathbf{0} \\ \mathbf{0} & \mathbf{0} & \cdots & \mathbf{0} & \mathbf{0} \\ \vdots & \vdots & \ddots & \vdots & \vdots \\ \mathbf{0} & \mathbf{0} & \cdots & \mathbf{0} & \mathbf{0} \\ \mathbf{0} & \mathbf{0} & \cdots & \mathbf{0} & \mathbf{0} \end{bmatrix}. \tag{2.98}$$

As can be seen, the first block row of this augmented VAR model contains a VAR(1) model, while the dimension corresponds to a VAR($p_{\max}$) model. For epoch $i = 1$, a VAR(2) model is placed in the first block row and the augmented white noise covariance is changed accordingly:

$$\begin{bmatrix} \boldsymbol{\Phi}_1^{(2)} & \boldsymbol{\Phi}_2^{(2)} & \cdots & \mathbf{0} & \mathbf{0} \\ \mathbf{I} & & \cdots & & \\ & \mathbf{I} & \cdots & & \\ & & \ddots & & \\ & & & \mathbf{I} & \end{bmatrix}, \begin{bmatrix} \boldsymbol{\Sigma}_{\mathbf{w}}^{(2)} & \mathbf{0} & \cdots & \mathbf{0} & \mathbf{0} \\ \mathbf{0} & \mathbf{0} & \cdots & \mathbf{0} & \mathbf{0} \\ \vdots & \vdots & \ddots & \vdots & \vdots \\ \mathbf{0} & \mathbf{0} & \cdots & \mathbf{0} & \mathbf{0} \\ \mathbf{0} & \mathbf{0} & \cdots & \mathbf{0} & \mathbf{0} \end{bmatrix}. \tag{2.99}$$

This augmented VAR structure can be abbreviated with the notation $\tilde{\mathbf{B}}(p, p_{\max})$, where the first argument corresponds to the order of the model placed in the first block row, while the second argument describes the maximum order and correspondingly the augmented state dimension. It is evident that $p \in \{1, \ldots, p_{\max}\}$. Since now both state transition matrix and white noise covariance depend on the epoch i, every component of the linear dynamic system is time variable. This means that

$$\begin{aligned} \mathbf{l}_i &= \tilde{\mathbf{A}}_i \tilde{\mathbf{x}}_i + \mathbf{e}_i & \mathbf{e}_i &\sim \mathcal{N}(\mathbf{0}, \boldsymbol{\Sigma}_{\mathbf{l}_i}) \\ \tilde{\mathbf{x}}_i &= \tilde{\mathbf{B}}_i \tilde{\mathbf{x}}_{i-1} + \tilde{\mathbf{w}}_i & \tilde{\mathbf{w}}_i &\sim \mathcal{N}(\mathbf{0}, \tilde{\mathbf{Q}}_i) \end{aligned} \tag{2.100}$$

with

$$\tilde{\mathbf{B}}_i = \begin{cases} \tilde{\mathbf{B}}(i+1, p_{\max}) & \text{for } i \in \{0, \ldots, p_{\max} - 1\} \\ \tilde{\mathbf{B}}(p_{\max}, p_{\max}) & \text{otherwise} \end{cases} \tag{2.101}$$

and

$$\tilde{\mathbf{Q}}_i = \begin{bmatrix} \boldsymbol{\Sigma}_{\mathbf{w}}^{(\min\{i+1, p_{\max}\})} & \mathbf{0} & \cdots & \mathbf{0} & \mathbf{0} \\ \mathbf{0} & \mathbf{0} & \cdots & \mathbf{0} & \mathbf{0} \\ \vdots & \vdots & \ddots & \vdots & \vdots \\ \mathbf{0} & \mathbf{0} & \cdots & \mathbf{0} & \mathbf{0} \\ \mathbf{0} & \mathbf{0} & \cdots & \mathbf{0} & \mathbf{0} \end{bmatrix}. \tag{2.102}$$

If both the initial state and the prediction is handled in the way presented here, the smoothed state estimates based on the augmented linear dynamic system (2.97) are identical to the least squares solution to (2.44) even for higher order VAR models. This implies that the least squares adjustment proposed in (2.44), is a generalization of the approach by Kurtenbach et al. (2012) from a VAR(1) model to VAR models of arbitrary order, which can be verified numerically.

2.3.2. Smoothing vs. filtering — practical considerations

From a statistical point of view, a smoothed state estimate will always have a smaller or equal variance compared to a filtered estimate. However, there are some practical applications where a higher variance of the state estimate has to be accepted. For example, in (near) real-time applications, smoothing does not provide any advantages. There, one operates on the edge of the smoothing interval where no information from the future is available. Thus, filtered and smoothed state estimates are identical (Gelb, 1974). A second consideration is the phase conservation property of the smoother. Since the Kalman smoother is equivalent to a forward and backward filter sweep, it conserves the phase of the input data. This behavior is exemplified with the GRACE Kalman filter/smoother used throughout this thesis.

On the basis of the normal equations used as input for the Kalman filter in (2.59) and the Kalman smoother (or the equivalent least squares adjustment) a set of synthetic observations can be constructed. The goal of this exercise is to investigate the response of

both filter and smoother to a sudden shock. This can then be interpreted as the impulse response of filter and smoother. To construct the impulse response, the epoch-wise system of normal equations $\mathbf{N}_i\hat{\mathbf{x}}_i = \mathbf{n}_i$ is used. Substituting the unconstrained estimates $\hat{\mathbf{x}}_i$ with a sequence of synthetic state vectors $\tilde{\mathbf{x}}_i$ yields right hand sides $\tilde{\mathbf{n}}_i$ which only contain the impulse response, rather than the original observations. The sequence $\tilde{\mathbf{x}}_i$ is given by

$$\tilde{\mathbf{x}}_i = \begin{cases} \mathbf{d} & \text{if } i = D \\ \mathbf{0} & \text{otherwise} \end{cases}, \tag{2.103}$$

where $\mathbf{d}$ is a non-zero column vector and D denotes the epoch where the impulse is introduced into the system. The values of $\mathbf{d}$, are derived from the auto-covariance matrix of the process $\mathbf{\Sigma}_{\mathbf{w}}^{(0)}$. Since $\mathbf{\Sigma}_{\mathbf{w}}^{(0)}$ is symmetric and positive definite it can be decomposed into

$$\mathbf{\Sigma}_{\mathbf{w}}^{(0)} = \mathbf{U}\mathbf{\Lambda}\mathbf{U}^T, \tag{2.104}$$

where $\mathbf{U}$ is an orthogonal matrix and $\mathbf{\Lambda}$ is a diagonal matrix which contains the Eigenvalues λ_k on the main diagonal (Golub & Loan, 1996). A reasonable choice for an impulse vector $\mathbf{d}$ is then given by

$$\mathbf{d} = \sum_{k=0}^{m-1} \mathbf{u}^{(k)} \sqrt{\lambda_k}, \tag{2.105}$$

$\mathbf{u}^{(k)}$ being the k-th column of $\mathbf{U}$. The expression for $\mathbf{d}$ is closely related to principal component analysis (PCA, Pearson, 1901). The set of Eigenvectors $\mathbf{U}$ represent a new orthogonal basis for the state vector and the Eigenvalues λ_k describe the expected variance along each of the new basis vectors. This means the vector $\mathbf{d}$ is an impulse of magnitude $\sqrt{\lambda_k}$ along each principal axis. The resulting normal equations with the synthetic right hand sides

$$\tilde{\mathbf{n}}_i = \begin{cases} \mathbf{N}_i\mathbf{d} & \text{if } i = D \\ \mathbf{0} & \text{otherwise} \end{cases}, \tag{2.106}$$

are then used to estimate both filtered and smoothed states over a certain time interval. The norm of the obtained smoothed and filtered state estimates $\|\mathbf{x}_i^s\|$ and $\|\mathbf{x}_i^+\|$ can be seen in Figure 2.3. As can be observed, the impulse response of the Kalman smoother decays symmetrically around the epoch where the impulse was introduced. The Kalman filter on the other hand remains zero for epochs $i < 0$, is excited at epoch $i = 0$ and then tends towards zero in later epochs.

For certain applications, for example, the investigation of flood dynamics, a symmetric impulse response is not desired, as the smoother already "knows" of any extreme events prior to their actual onset. Here, a purely filtered solution is preferred even in offline applications although it is suboptimal in a statistical sense.

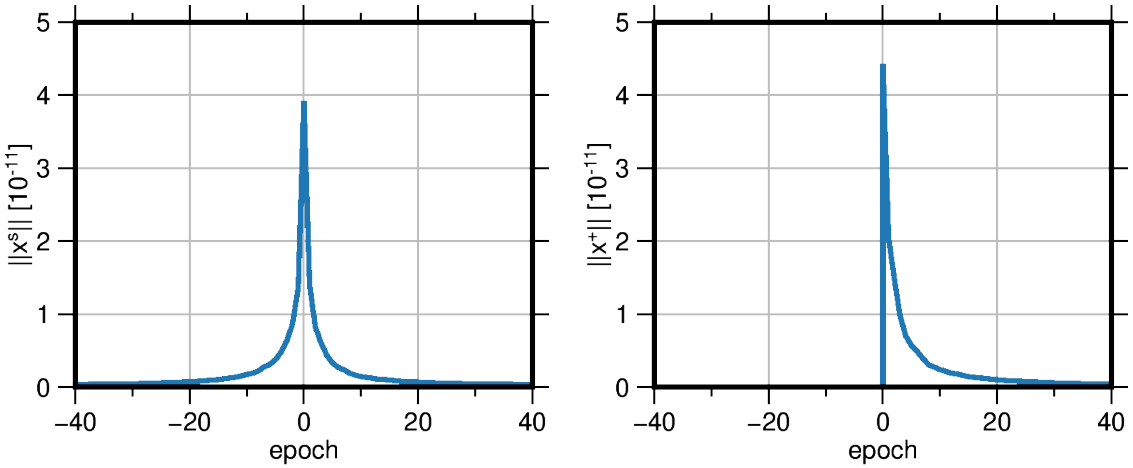

(a) Kalman smoother

(b) Kalman filter

Figure 2.3.: Norm of state estimates $\mathbf{x}_i^s$ and $\mathbf{x}_i^+$ of a Kalman smoother and Kalman filter excited by an impulse at epoch $D = 0$.

2.4. Derivation of the process model

Lütkepohl (2005) provides a thorough review of a variety of methods for the estimation of VAR processes, which will be briefly summarized here. All presented methods assume that a realization of the underlying stationary process given as N samples of dimension m is available. Further, this sample is assumed to be centered which, while not strictly required, does allow for a more concise mathematical description without loss of generalization.

As first method, the multivariate least squares estimator is discussed. By transposing the VAR model equation (2.36), the observation equation for a single process realization epoch, with

$$\mathbf{v}_i^T = \begin{bmatrix} \mathbf{v}_{i-1}^T & \mathbf{v}_{i-2}^T & \cdots & \mathbf{v}_{i-p}^T \end{bmatrix} \begin{bmatrix} \mathbf{\Phi}_1^{(p),T} \\ \mathbf{\Phi}_2^{(p),T} \\ \vdots \\ \mathbf{\Phi}_p^{(p),T} \end{bmatrix} + \mathbf{w}_i^T \tag{2.107}$$

is obtained. When arranged for all available epochs $i \in \{p, \ldots, N-1\}$, the overdetermined system of equations

$$\underbrace{\begin{bmatrix} \mathbf{v}_p^T \\ \vdots \\ \mathbf{v}_{N-1}^T \end{bmatrix}}_{=\mathbf{L}} = \underbrace{\begin{bmatrix} \mathbf{v}_{p-1}^T & \mathbf{v}_{p-2}^T & \cdots & \mathbf{v}_0^T \\ \vdots & \vdots & & \vdots \\ \mathbf{v}_{N-2}^T & \mathbf{v}_{N-3}^T & \cdots & \mathbf{v}_{N-1-p}^T \end{bmatrix}}_{=\mathbf{A}} \underbrace{\begin{bmatrix} \mathbf{\Phi}_1^{(p),T} \\ \mathbf{\Phi}_2^{(p),T} \\ \vdots \\ \mathbf{\Phi}_p^{(p),T} \end{bmatrix}}_{=\mathbf{X}} + \underbrace{\begin{bmatrix} \mathbf{w}_p^T \\ \vdots \\ \mathbf{w}_{N-1}^T \end{bmatrix}}_{=\mathbf{W}} \tag{2.108}$$

can then be solved using the standard method for multivariate parameter estimates (e.g. Koch, 2004). It is briefly noted that the process realizations $\mathbf{v}_i$ are treated as stochastic quantities on the observation side of the least squares adjustment but as deterministic quantities in the design matrix $\mathbf{A}$. This approximation results in a biased estimation of the VAR model coefficients as the first p are implicitly treated as constant initial values (Wei, 2006). The relative influence of this bias however decreases with increasing number of samples, thus asymptotically, the least squares adjustment yields unbiased estimates for the VAR model. Once the model coefficients are estimated, the noise covariance matrix $\mathbf{\Sigma}_{\mathbf{w}}^{(p)}$ can be determined from the estimated residuals $\hat{\mathbf{w}}_i$ through the empirical estimator

$$\mathbf{\Sigma}_{\mathbf{w}}^{(p)} = \frac{1}{N - mp} \sum_{i=p}^{N-1} \hat{\mathbf{w}}_i \hat{\mathbf{w}}_i^T. \tag{2.109}$$

An efficient QR factorization (Golub & Loan, 1996) based implementation of this method can be found in Neumaier and Schneider (2001).

Assuming that the distribution of the process is known, maximum likelihood (ML) estimation is an alternative to the the multivariate least squares estimator. With the assumption that the VAR(p) process is Gaussian, the probability density of $\mathbf{w}$ is

$$f_{\mathbf{w}}(\mathbf{w}) = \frac{1}{((2\pi)^{mN/2}} |\mathbf{I} \otimes \mathbf{\Sigma}_{\mathbf{w}}^{(p)}|^{-1/2} \exp\left[-\frac{1}{2} \mathbf{w}^T (\mathbf{I} \otimes \mathbf{\Sigma}_{\mathbf{w}}^{(p)^{-1}}) \mathbf{w} \right], \tag{2.110}$$

where m is the dimension of the process, $\otimes$ denotes the Kronecker product, and $|\mathbf{I} \otimes \mathbf{\Sigma}_{\mathbf{w}}^{(p)}|$ is the determinant of the matrix. This leads to the log-likelihood function

$$\begin{aligned} \ln l(\mathbf{\Phi}_1^{(p)}, \ldots, \mathbf{\Phi}_p^{(p)}, \mathbf{\Sigma}_{\mathbf{w}}^{(p)}) = &-\frac{mN}{2} - \ln 2\pi - \frac{N}{2} \ln |\mathbf{\Sigma}_{\mathbf{w}}^{(p)}| \\ &-\frac{1}{2} \mathrm{tr}\left[(\mathbf{L} - \mathbf{A}\mathbf{X}) \mathbf{\Sigma}_{\mathbf{w}}^{(p)^{-1}} (\mathbf{L} - \mathbf{A}\mathbf{X})^T \right], \end{aligned} \tag{2.111}$$

where $\mathbf{L}$, $\mathbf{A}$, and $\mathbf{X}$ are defined as in the least squares estimator. The values for $\mathbf{X}$ and $\mathbf{\Sigma}_{\mathbf{w}}^{(p)}$ which maximize this function are than the ML estimates for the VAR(p) model coefficients and white noise covariance. When the underlying distribution function is Gaussian, this ML estimate is identical to the least squares approach.

The last method discussed are the so-called the Yule-Walker (YW) equations. Multiplying (2.107) with $\mathbf{v}_j$ from the left yields

$$\mathbf{v}_j \mathbf{v}_i^T = \begin{bmatrix} \mathbf{v}_j \mathbf{v}_{i-1}^T & \mathbf{v}_j \mathbf{v}_{i-2}^T & \cdots & \mathbf{v}_j \mathbf{v}_{i-p}^T \end{bmatrix} \begin{bmatrix} \mathbf{\Phi}_1^{(p),T} \\ \mathbf{\Phi}_2^{(p),T} \\ \vdots \\ \mathbf{\Phi}_p^{(p),T} \end{bmatrix} + \mathbf{v}_j \mathbf{w}_i^T. \tag{2.112}$$

After taking the expectancy of (2.112),

$$\boldsymbol{\Sigma}_{\mathbf{v}}(j-i) = \begin{bmatrix}\boldsymbol{\Sigma}_{\mathbf{v}}(j-i+1) & \boldsymbol{\Sigma}_{\mathbf{v}}(j-i+2) & \cdots & \boldsymbol{\Sigma}_{\mathbf{v}}(j-i+p)\end{bmatrix} \begin{bmatrix}\boldsymbol{\Phi}_1^{(p),T} \\ \boldsymbol{\Phi}_2^{(p),T} \\ \vdots \\ \boldsymbol{\Phi}_p^{(p),T}\end{bmatrix} + E\{\mathbf{v}_j \mathbf{w}_i^T\} \tag{2.113}$$

is obtained when taking into account that $\mathbf{v}_i$ is a stationary process. The covariance matrix $E\{\mathbf{v}_j \mathbf{w}_i^T\}$ vanishes for $j \neq i$, since $\mathbf{w}_i$ is assumed to be white noise. Arranging (2.113) for $j - i = h \in \{-1, \ldots, -p\}$ then leads to the system of equations

$$\begin{bmatrix}\boldsymbol{\Sigma}_{\mathbf{v}}^T(1) \\ \boldsymbol{\Sigma}_{\mathbf{v}}^T(2) \\ \vdots \\ \boldsymbol{\Sigma}_{\mathbf{v}}^T(p)\end{bmatrix} = \begin{bmatrix}\boldsymbol{\Sigma}_{\mathbf{v}}(0) & \boldsymbol{\Sigma}_{\mathbf{v}}(1) & \cdots & \boldsymbol{\Sigma}_{\mathbf{v}}(p-1) \\ \boldsymbol{\Sigma}_{\mathbf{v}}^T(1) & \boldsymbol{\Sigma}_{\mathbf{v}}(0) & \cdots & \boldsymbol{\Sigma}_{\mathbf{v}}(p-2) \\ \vdots & \vdots & \ddots & \vdots \\ \boldsymbol{\Sigma}_{\mathbf{v}}^T(p-1)^T & \boldsymbol{\Sigma}_{\mathbf{v}}(p-2)^T & \cdots & \boldsymbol{\Sigma}_{\mathbf{v}}(0)\end{bmatrix} \begin{bmatrix}\boldsymbol{\Phi}_1^{(p),T} \\ \boldsymbol{\Phi}_2^{(p),T} \\ \vdots \\ \boldsymbol{\Phi}_p^{(p),T}\end{bmatrix}, \tag{2.114}$$

where the property $\boldsymbol{\Sigma}_{\mathbf{v}}(-h) = \boldsymbol{\Sigma}_{\mathbf{v}}^T(h)$ of a multivariate stationary covariance function was used. After solving (2.114), which yields the coefficients $\boldsymbol{\Phi}_k^{(p)}$, the white noise covariance matrix $\boldsymbol{\Sigma}_{\mathbf{w}}^{(p)}$, can be computed from (2.113) for $j = i$. Thus, after evaluating

$$\boldsymbol{\Sigma}_{\mathbf{w}}^{(p)} = \boldsymbol{\Sigma}_{\mathbf{v}}(0) - \begin{bmatrix}\boldsymbol{\Sigma}_{\mathbf{v}}(1) & \boldsymbol{\Sigma}_{\mathbf{v}}(2) & \cdots & \boldsymbol{\Sigma}_{\mathbf{v}}(p)\end{bmatrix} \begin{bmatrix}\boldsymbol{\Phi}_1^{(p),T} \\ \boldsymbol{\Phi}_2^{(p),T} \\ \vdots \\ \boldsymbol{\Phi}_p^{(p),T}\end{bmatrix}, \tag{2.115}$$

the VAR(p) model is fully determined. What stands out in (2.114) is that the covariance structure of the underlying process has to be known in order to populate the equations. In practice, this is however not the case. Thus, an estimate for $\boldsymbol{\Sigma}_{\mathbf{v}}(h)$, for example, (2.35) has to be used to set up and solve the YW equations. If the unbiased estimator (2.35) is used, the YW equations are numerically identical to the normal equations of the least squares estimate (2.108), which can easily be verified.

As discussed earlier, all methods for the determination of the VAR(p) model require a process realization either implicitly, like the YW equations, or explicitly, like the least squares approach. The question now arises as to what constitutes the process for the case at hand, the determination of high frequency gravity field solutions, and how such a realization can be obtained. According to Kurtenbach et al. (2012), the following can be postulated. The underlying process consists of all geophysical signals contained in the observations, which are not reduced by the background models. For a standard GRACE solution, this predominantly includes continental hydrology, changes in the cryosphere, residual atmosphere and ocean signals and variations of the solid earth (Bettadpur, 2018).

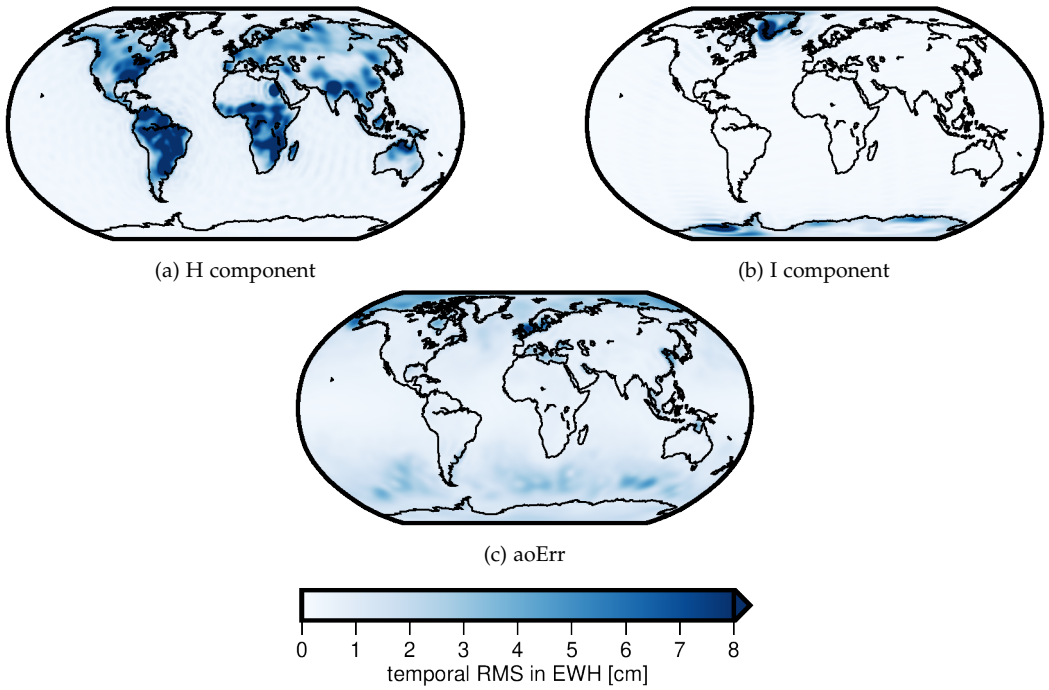

Figure 2.4.: Temporal RMS of H, I, and aoErr after reducing a linear trend and an annual oscillation, which serve as basis for the process model.

The realization of the process is obtained from the European Space Agency (ESA) Earth System Model (ESA ESM, Dobslaw et al., 2015, 2016) for satellite gravity mission simulations. The dataset provides six-hourly time series of potential changes from atmosphere (A) ocean (O), hydrosphere (H), cryosphere (I), and solid Earth (S), as well as a time series of estimated atmosphere and ocean model errors (aoErr). All subsystems are given to a maximum spherical harmonic degree of 180 for a full solar cycle of 12 years. To match the sampling of the sought-after gravity field snapshots, first a temporal low pass filter is applied. Then a downsampling to the appropriate time intervals is performed. Furthermore, the spatial resolution is also reduced by truncating at the same expansion degree as the parametrization of $\Delta\mathbf{x}_i$. Since $\Delta\mathbf{x}_i$ are estimated relative to a long-term mean field, including secular and annual variations, these constituents are estimated and reduced from the data set. The resulting residual time series

$$\tilde{\mathbf{v}}_i = \tilde{\mathbf{v}}_i^{\mathrm{H}} + \tilde{\mathbf{v}}_i^{\mathrm{I}} + \tilde{\mathbf{v}}_i^{\mathrm{aoErr}} \tag{2.116}$$

is then interpreted as a realization of the underlying process. It is briefly noted that variations in the solid Earth are not considered in (2.116), as the instantaneous co-seismic gravity field changes caused by earthquakes cannot be modelled through a stationary process. The temporal root mean square (RMS) of the three components H, I, and aoErr after reducing a linear trend and an annual oscillation can be seen in Figure 2.4. Even though $\tilde{\mathbf{v}}_i$ is of global nature, an argument can be made that errors in the ocean model are not correlated with the residual hydrological signal on the continents or changes in the cryosphere. Since these two processes are spatially separated, this assumption can be reflected in the covariance structure of $\tilde{\mathbf{v}}_i$, by introducing land/ocean masks in

the estimation of $\tilde{\mathbf{\Sigma}}_{\mathbf{v}}$. In practice, this is implemented by propagating $\tilde{\mathbf{v}}_i$ to the spatial domain as EWH and deriving covariance matrices for individual landmasses and the ocean independently. The reason for choosing the water height kernel as opposed to potential is that the potential generating masses are assumed to be localizing and can therefore be windowed. For each defined region Ω_i, the empirical covariance estimator (2.35) is applied to the time series of gridded EWH values, resulting in a set of covariance matrices $\mathbf{\Sigma}_{\Omega_i}$. Finally, the covariance matrices of all regions are then assembled in a block diagonal fashion with

$$(\mathbf{\Sigma}_{\Omega})_{ii} = \mathbf{\Sigma}_{\Omega_i}. \tag{2.117}$$

The spatial covariance matrix is then transformed back to the spectral domain through variance-covariance propagation with

$$\tilde{\mathbf{\Sigma}}_{\mathbf{v}} = \mathbf{F}\mathbf{\Sigma}_{\Omega}\mathbf{F}^T, \tag{2.118}$$

where

$$(f_{nm,j}) = \frac{R}{GM}\frac{a_j}{4\pi}\left(\frac{4\pi R^2\rho_w}{M}\frac{1+k'_n}{2n+1}\right)\left(\frac{r_j}{R}\right)^{n+1} Y_{nm}\left(\frac{\mathbf{r}_j}{r_j}\right). \tag{2.119}$$

The matrix $\mathbf{F}$ constitutes a quadrature, which yields spherical harmonic coefficients from a EWH values given at points at position $\mathbf{r}_j$, with area element a_j and geocentric radius r_j. In (2.119), R is the reference radius, GM is the geocentric gravitational constant, M is Earth's mass, ρ_w is the density of water, k'_n are load Love numbers, and Y_{nm} are surface spherical harmonics. The availability of the covariance matrix in the spatial domain also opens up another possibility to improve the robustness of the VAR model computation. By reducing the correlation between individual grid points, the compound covariance matrix $\mathbf{\Sigma}_{\Omega}$ becomes more diagonally dominant, thus potentially improving the condition of the matrix. The elements of $\mathbf{\Sigma}_{\Omega}$ can be written as $\sigma_{ij} = r_{ij}\sigma_i\sigma_j$, where r_{ij} is the correlation between the points i and j, with the corresponding standard deviation σ_i and σ_j, (e.g., Huber & Ronchetti, 2009). This allows the introduction of the modified correlation $\tilde{r}_{ij} = r_{ij} \cdot f(\psi_{ij})$, where f is a function of the spherical distance ψ_{ij} between the two points. For the application at hand, an exponential decay of the form

$$f(\psi) = e^{-\frac{\psi}{\psi_0}} \tag{2.120}$$

was chosen, although other functions are equally applicable. The amount of correlation change is governed by the parameter ψ_0. For $\psi_0 \to \infty$, the original matrix is obtained, for $\psi_0 \to 0$, the matrix becomes strictly diagonal. The effect of this correlation scaling and its dependency on ψ_0 can be seen in figure 2.5. The reciprocal condition number of the auto-covariance $\tilde{\mathbf{\Sigma}}_{\mathbf{v}}(0)$ is closer to 1 for smaller ψ_0, increasing the stability of the Yule-Walker equations. Compared to the unmodified covariance matrix, the condition improves by two orders of magnitude for a ψ_0 corresponding to a half-width of approximately 1100 km, when using this approach. The impact of each step, namely the introduction of a land/ocean mask and the artificial decrease of correlations between far away points, can be seen in Figure 2.6. Here, the spatial correlations of a single point at (15E, 47N)

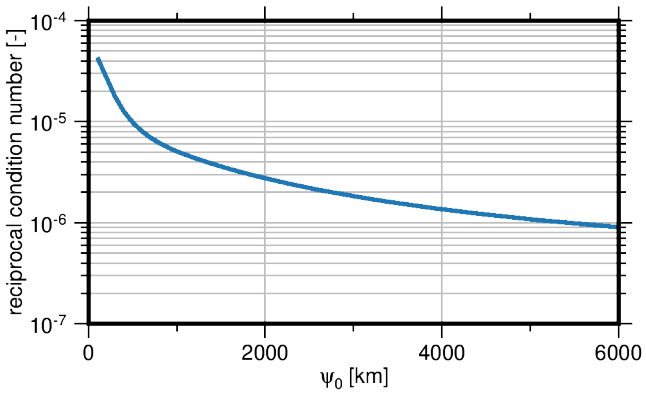

Figure 2.5.: Dependency of the condition number of $\tilde{\mathbf{\Sigma}}_{\mathbf{v}}(0)$ on the parameter ψ_0.

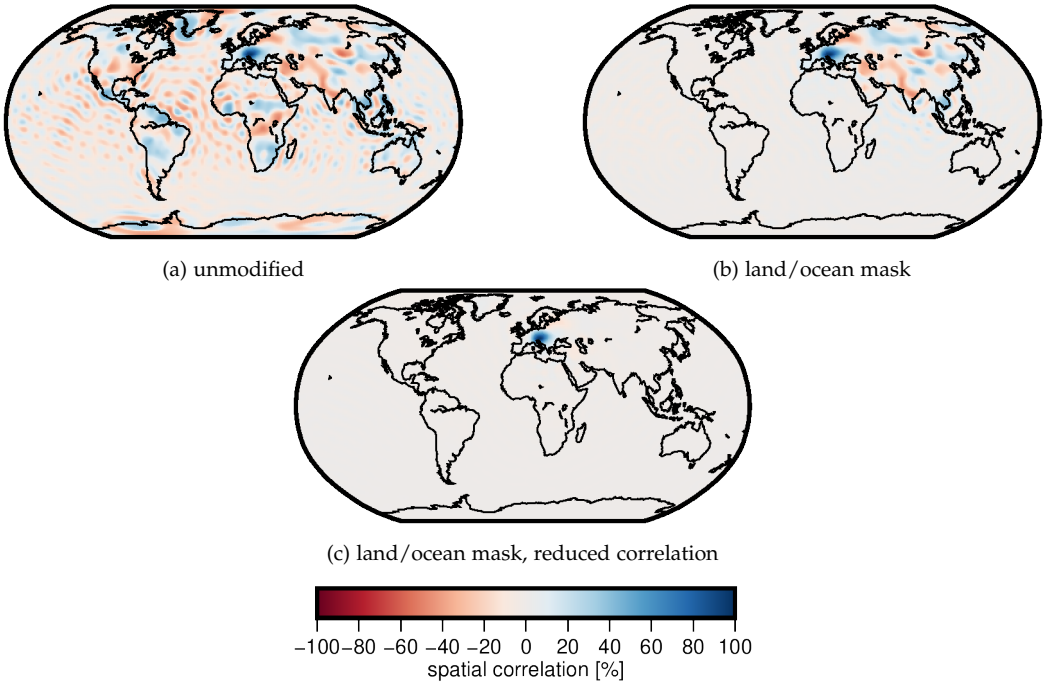

Figure 2.6.: Effect of correlation scaling and land/ocean mask on the spatial correlations of a single point (15E, 47N).

with all other points of the globe is visualized. In Figure 2.6a, which is based on the covariance matrix directly computed from the spherical harmonic vectors, thus includes no further information, global correlations can be observed. Striking are the ringing effects in the oceans which can reach up to $\pm 30\%$. The situation improves once a separation of landmasses and the ocean is introduced, which can be seen in Figure 2.6b. Finally, the introduced distance dependent exponential decay of the correlation does drastically reduce the correlation length, which results in a very localized covariance structure. While this in itself is not a guarantee for an improved description of the stochastic properties of the process, the improved condition during the process model computation as well as the clear reduction of ringing effects are an indication of a potential improvement. The processing of the ESA ESM potential coefficients can be summarized as

Truncation The potential coefficients are truncated to spherical harmonic degree 40, to reduce the dimensionality of the problem. While this improves both the computation time and the robustness of the covariance estimates, it also limits the spatial resolution of the VAR(p) models.

Downsampling From six-hourly potential coefficient time series, daily averages are computed. This constitutes both a low-pass filter and downsampling in time domain.

EWH covariance matrices The daily potential coefficient time series is propagated to EWH grids. From these grid time series, covariance matrices are estimated using the unbiased estimator (2.35). Correlations between land and ocean points are set to zero, the correlations between the remaining points are scaled with a distance-dependent function.

Propagation to spherical harmonic domain Finally, the resulting covariance matrices are propagated back to spherical harmonic domain.

The obtained covariance matrices $\tilde{\mathbf{\Sigma}}(h)$ are then used to estimate VAR(p) model coefficients using Yule-Walker equations. Result of this step are $p_{\max}+1$ VAR(p) models, each consisting of model coefficients $\mathbf{\Phi}_k^{(p)}$ and white noise covariance matrix $\mathbf{\Sigma}_{\mathbf{w}}^{(p)}$. When using the 12 years of ESA ESM data in conjunction with the land/ocean mask and correlation scaling, the maximum order of the derived VAR(p) models was $p_{\max}=3$. For higher orders, the coefficient matrix of the YW equations was singular and thus not invertible. The white noise covariance matrices for each of the derived VAR(p) models, propagated to space domain, can be seen in Figure 2.7. It is evident, that the white noise covariance of the VAR(0) model is higher than the other model orders. This is simply explained by the fact that, since no correlations in time are considered, it is identical to the auto-covariance of the process. For all orders $p>0$ the picture looks pretty similar. In order to better identify areas of variance change, the variance reduction (VR) of each grid point for consecutive model orders is shown in Figure 2.8. VR is defined as

$$VR = 1 - \frac{\sigma_y^2}{\sigma_x^2} \tag{2.121}$$

and maps the variances of two stochastic variables onto the interval $(-\infty, 1]$. This allows for a unitless comparison of two variance values. It is evident that, unsurprisingly, the largest variance reduction happens from order 0 to order 1. From order 1 to order 2, large improvements in ocean areas can be observed. While globally, the improvement from

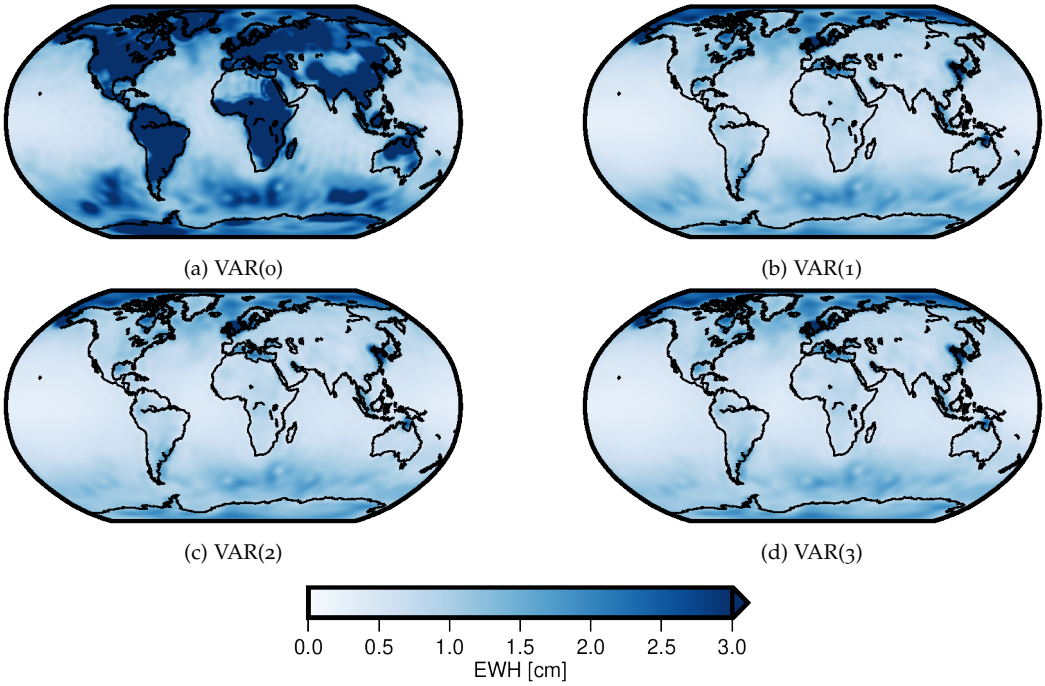

(a) VAR(0) (b) VAR(1)

(c) VAR(2) (d) VAR(3)

Figure 2.7.: White noise covariance matrix $\boldsymbol{\Sigma}_{\mathbf{w}}^{(p)}$ for autoregressive models of order $p = \{0, 1, 2, 3\}$ (standard deviation propagated to EWH).

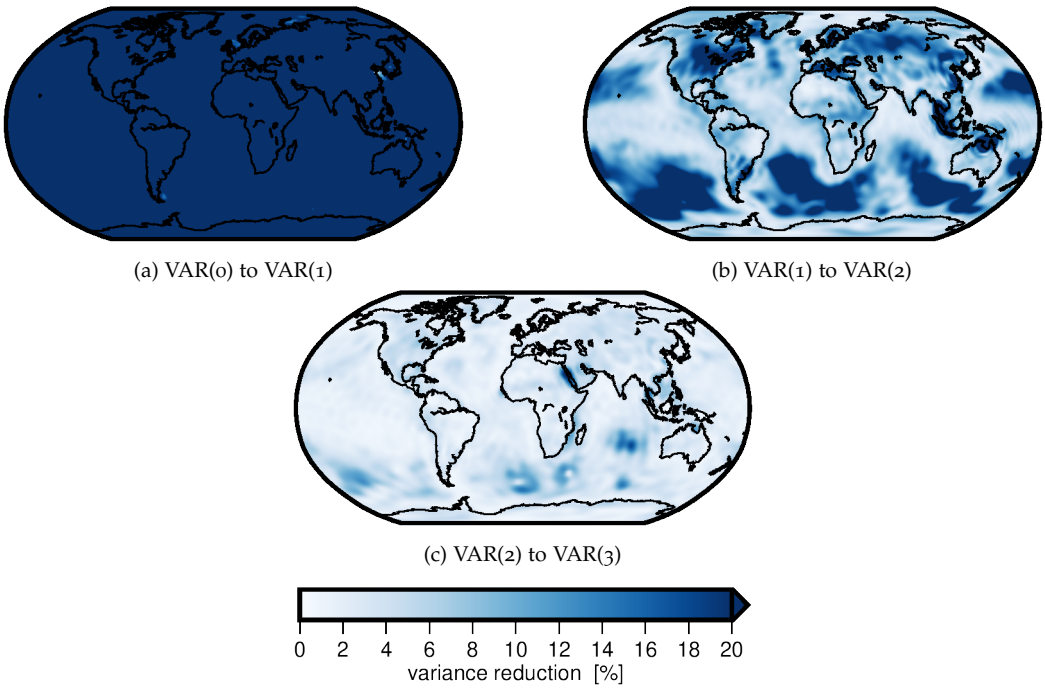

(a) VAR(0) to VAR(1) (b) VAR(1) to VAR(2)

(c) VAR(2) to VAR(3)

Figure 2.8.: White noise variance reduction between consecutive orders of VAR(p) models.

order 2 to order 3 is only moderate, locally a variance reduction of up to 25% can be seen. It is also briefly noted that the variance reduction is always positive with increasing model order. This can be explained trough the equivalence of the YW equations with the least squares estimator for VAR models. Increasing the model order requires more parameters to be estimated, which implies that the adjusted residuals $\hat{\mathbf{w}}_i$ become smaller. Since $\boldsymbol{\Sigma}_{\mathbf{w}}^{(p)}$ is essentially the covariance matrix of these adjusted residuals, their variances also decrease.

2.4.1. Evaluation of the derived process model

The innovation sequence

In order to gauge the quality of the derived process model, a variety of methods exist. A first key question concerning the process model is: "How well does the prediction fit actual GRACE observations?" Starting from a VAR(p) constrained gravity field estimate $\Delta\hat{\mathbf{x}}^{(p)}$, the gravity field prediction

$$\Delta\mathbf{x}_i^- = \sum_{k=1}^{p} \boldsymbol{\Phi}_k^{(p)} \Delta\hat{\mathbf{x}}_{i-k}^{(p)}, \tag{2.122}$$

can be computed. By substituting the predicted state $\Delta\mathbf{x}_i^-$ into the corresponding observation equations, predicted observations denoted $\Delta\mathbf{l}_i^-$ are obtained. It is important to remember here that the observations do not only depend on the gravity field but also satellite state and instrument calibration parameters. Thus, the predicted observations have to be computed from the full functional model

$$\Delta\mathbf{l}_i^- = \mathbf{A}_i\Delta\mathbf{x}_i^- + \mathbf{B}_i\Delta\mathbf{z}_i^-. \tag{2.123}$$

However, since the parameter subset $\mathbf{z}$ is not contained in the process model, no prior information about these unknowns is introduced. This can equivalently be interpreted as predicting these parameters with a zero-vector and complete uncertainty. Thus, the prediction of $\Delta\mathbf{z}_i$ is given by

$$\Delta\mathbf{z}_i^- = \mathbf{0}, \text{ with } \boldsymbol{\Sigma}_{\Delta\mathbf{z}_i^-} \to \infty. \tag{2.124}$$

Consequently, the predicted observations reduce to

$$\Delta\mathbf{l}_i^- = \mathbf{A}_i\Delta\mathbf{x}_i^-. \tag{2.125}$$

The difference vector

$$\mathbf{d}_i = \Delta\mathbf{l}_i - \Delta\mathbf{l}_i^- \tag{2.126}$$

then gives a measure of how well the predicted observations fit with the actual measurements. In the context of state estimation, it is often denoted the innovation vector (Lütkepohl, 2005).

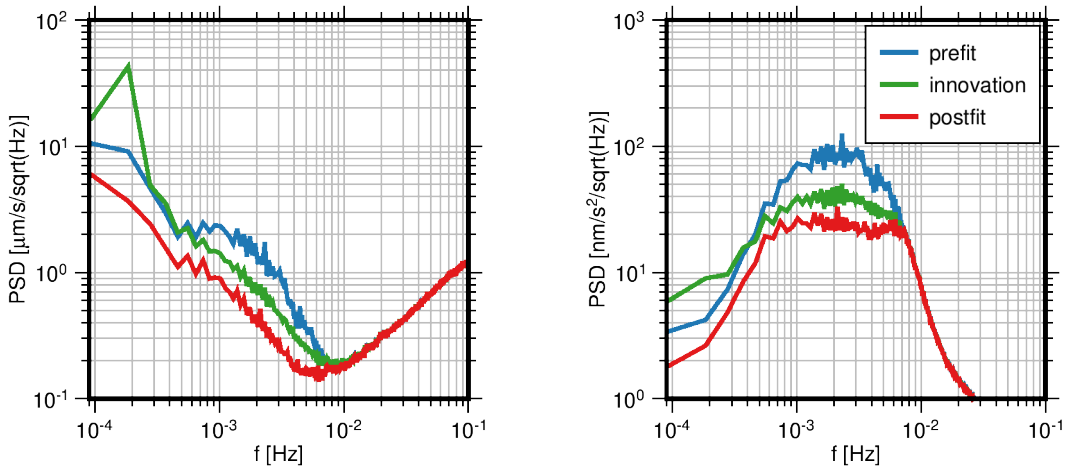

(a) range-rate

(b) range-acceleration (band-pass filtered)

Figure 2.9.: PSD of pre-fit residual, post-fit residuals, and innovation as range rates (left) and band-pass filtered range acceleration.

For an easier interpretation, each epoch of $\mathbf{d}_i$ can be mapped to a point on the Earth's surface through the satellites' ground track pattern. Given the polar orbit of GRACE-type missions, a rule-of-thumb which relates the spatial frequencies of the spherical harmonic spectrum to the time series domain can be formulated. Denoting the orbital period of the satellites T, thus relation between a spherical harmonic degree n and spectral line in the Fourier domain f_n is simply given through $f_n = \frac{n}{T}$. For GRACE, where $T \approx 5400$ s and the chosen parametrization of the gravity field with $n = \{2, \ldots, 40\}$, the frequency band of interest therefore spans approximately $3.7 \cdot 10^{-4}$ Hz to $7.4 \cdot 10^{-3}$ Hz. Furthermore, it is reasonable to convert the range-rates to range-accelerations through numerical differentiation. This high-pass filter reduces the correlation length, which reveals more localized geophysical features along the orbit. The spectral characteristics of $\mathbf{d}_i$ compared to pre-fit and post-fit residuals for a single month before and after filtering can be seen in figure 2.9. Unsurprisingly, pre-fit residuals exhibit the highest power in the frequency band where gravity signal is expected. In the innovation sequence, the situation slightly improves, which means the prediction is at least better than assuming a zero state vector. Finally, the post-fit residuals have the lowest magnitude as they are based on both the estimated gravity field, instrument calibration, and satellite state parameters. To evaluate the prediction capabilities of the computed VAR models, filtered differences in the time span from 2005 to 2010 were computed. This time period was chosen because a nearly homogeneous observation quality due to the still-active thermal management of the satellites (Tapley, Flechtner, Watkins, & Bettadpur, 2015), minimal orbit decay, and an extended solar flux quiet period (e.g., Agee, Cornett, & Gleason, 2010). Moreover, this time span contains no large data gaps or orbit repeat cycles. Therefore, a consistent set of estimates $\Delta\hat{\mathbf{x}}_i^{(p)}$ can be expected.

In order to gauge the effect of the introduced geophysical constraints, a comparison between two VAR(1) models is performed. For the derivation of the first model, neither land/ocean mask nor distance depended scaling have been applied, that is, the unbi-

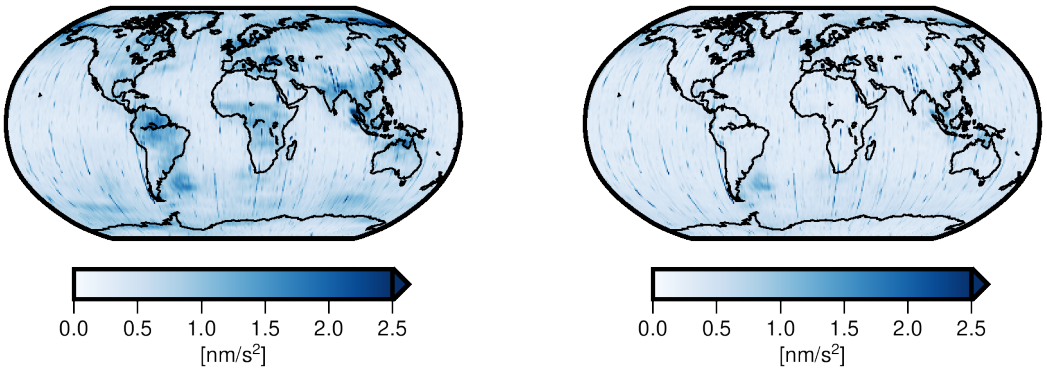

(a) no constraints (b) constraints applied

Figure 2.10.: RMS of band-pass filtered range-acceleration innovation for two VAR(1) models.

ased estimator (2.35) is directly applied to the time series of potential coefficients. This corresponds to the approach used by Kurtenbach et al. (2012). It is briefly noted that in order for the auto-covariance to be positive definite, the diagonal of the matrix had to be augmented with isotropic noise. This post-processing step is discussed in detail in Kurtenbach (2011). The second VAR(1) model is based on the same input data, however both geophysical constraints are applied. Filtered innovations $\mathbf{d}_i$ based on the two VAR(1) models, mapped to Earth's surface can be seen in Figure 2.10. All epochs within the evaluation time span were binned in 1×1 degree tiles and the RMS for each tile was computed. The innovations $\mathbf{d}_i$ clearly carry geophysical information, as the largest RMS values occur in regions where the geophysical models used to derive the VAR model are known to have deficiencies (Dobslaw et al., 2015, 2017). This includes marginal seas like the Black Sea, the Mediterranean Sea, the North Sea or the Gulf of Carpentaria. Regions with large ocean currents such as the Gulf Stream or the Agulhas Current can also be identified. Another very prominent signal is visible in the Argentinian basin, where a stochastic eddy generation process which cannot be modelled in non-assimilated ocean models is a major driver of the variability. It is evident that the geophysical constraints reduce the RMS of the innovation sequence with an average RMS reduction of 33%. RMS reduction in this context is defined as

$$RR_\Omega = 1 - \frac{RMS_\Omega(y_i)}{RMS_\Omega(x_i)}, \tag{2.127}$$

where $RMS_\Omega(\cdot)$ denotes the RMS of all values in a single tile Ω. This is a clear indication that the developed approach does improve the derived Kalman filter process models.

Decorrelation properties of VAR(p) models

The mapping $\mathbf{w} = \bar{\mathbf{\Phi}}\mathbf{v}$ can be interpreted as a decorrelation filter, since the input sequence $\mathbf{v}$ is possibly correlated in time, while the output $\mathbf{w}$ is white noise. This will only hold true if the VAR(p) perfectly represents the temporal correlations of the process. Given the challenges encountered in the determination of the model coefficients as outlined in

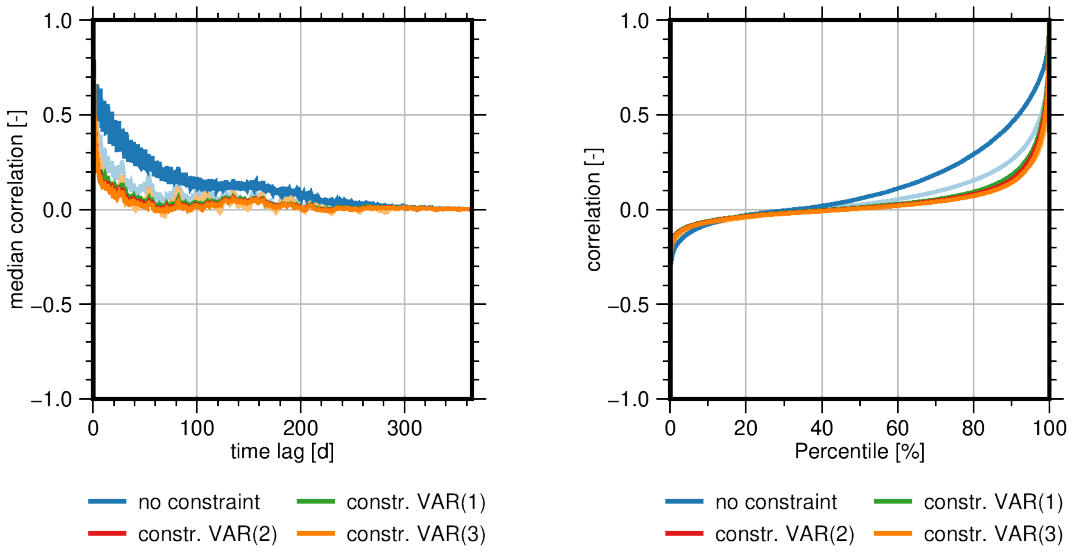

(a) median correlation

(b) cumulative distribution

Figure 2.11.: Median autocorrelation function for different VAR models separated into land points (dark colors) and ocean points (light colors).

the previous section, it is reasonable to assume that the estimated stochastic properties are only an approximation. In order to gauge the quality of the approximation, one can investigate if the supposed white noise sequence $\mathbf{w}$ still contains correlations in time.

To gauge the decorrelation properties of the VAR(p) models, the post-fit residuals $\hat{\mathbf{w}}_i$ of a least squares adjustment with GRACE data are investigated. To provide a more intuitive geophysical interpretation, the residual potential coefficients are propagated to a Reuter grid (Reuter, 1982) in EWH. This grid was chosen as the even point distribution avoids the overrepresentation of higher latitudes when, for example, a geographic grid is used. The representation in space domain also allows to easily discriminate between land and ocean points, for a more detailed analysis. As a measure of remaining temporal correlation in the residuals, the auto-correlation function for each of these EWH time series was then computed. Figure 2.11 shows different representations of the autocorrelation function of the post-fit residuals. In Figure 2.11a, the median correlation of all land/ocean points for an unconstrained VAR model and constrained VAR model of different orders are shown. As can be seen, the unconstrained VAR model exhibits a higher correlation length compared to the constrained models. The residual time series of the constrained models are much closer to white noise, with a sharp drop in correlation in the first few days. Also, the median correlation for land and ocean pixels is much more similar compared to the unconstrained model, which suggests a globally homogeneous fit. A minor improvement can be observed when the model order is increased. From Figure 2.11b, which shows the cumulative distribution of the auto-correlation function, similar conclusions can be drawn. Again, the number of non-zero correlation values is much higher for the unconstrained model compared to the constrained VAR(p) estimates. These investigations lead to the same conclusions as the analysis of the innovation sequence, indicating an overall better fit of the constraint VAR(p) to the GRACE data.

3. Near real-time processing chain

To obtain gravity field estimates from GRACE/GRACE-FO, not only data collected by the satellites themselves, but a variety of external data and geophysical models are required. A key challenge when operating in near real-time is the acquisition of these data, which are generally distributed across multiple data centers. The availability, latencies, and update periods generally vary between data sources. The implementation of a robust strategy for acquiring the necessary observation and model values, tailored to each source, is therefore fundamental. After all required data is available, the gravity field recovery process can be initiated. Ideally, this procedure is designed in a way so that it can easily be automated to enable operational applications which do not require manual intervention. To ensure traceability of the results, a thorough documentation of each processing step and archiving of intermediate results is key.

3.1. Observables and data stream

The main observables for GRACE/GRACE-FO based gravity field solutions used in the approach outlined here are kinematic orbit positions and inter-satellite range-rates as listed in section 2.1. In order to compute these quantities, a variety of input data from multiple data sources is required. Naturally, the measurements taken aboard the spacecraft are fundamental for the further processing steps. For GRACE/GRACE-FO, pre-processed observation data are contained in the Level-1B (L1B) data stream, which consists of daily files for the primary instruments, housekeeping data, and auxiliary telemetry. A comprehensive list of all available data files is given in Table 3.1. Relevant instrument files for gravity field recovery include SCA1B, ACC1B, KBR1B, GPS1B, GNV1B. Furthermore, the sequence-of-event (SOE) file contains additional information about the satellite state, such as active instrument, attitude modes and orbit maneuvers. The GRACE/GRACE-FO data stream is self-contained and directly provided by JPL. To process the instrument files however, external data is required. Kinematic orbit positions are derived by performing precise point positioning (PPP) using phase and code measurements of the GPS receiver aboard the spacecraft. This requires precise orbit and clock data from the GPS satellites. In order to ensure high-quality kinematic orbit positions of the satellites, auxiliary global navigation satellite system (GNSS) data products are required to perform corrections to the GPS observations. Examples of such auxiliary data products are differential code bias (DCB), or precise antenna phase center variations (ACV) for the transmitting GPS satellites contained in an Antenna Exchange Format (ANTEX) file, as well as GRACE. Since the GPS ACV of GRACE also depend on the state of instruments aboard the satellites, additional metadata and telemetry are

Table 3.1.: GRACE quick-look L1B data files.

File name	Satellite ID	Contents
ACC1B	A/B	accelerometer measurements (linear and angular)
ACC1B (R3)	B	accelerometer transplant
AHK1B	A/B	accelerometer housekeeping data
CLK1B	A/B	satellite clock estimate
GNV1B	A/B	dynamic orbit
GPS1B	A/B	GPS flight data
IHK1B	A/B	processing unit housekeeping data
KBR1B	both	KBR ranging data
MAG1B	A/B	Magnetic torquer activation, magnetometer data
MAS1B	A/B	Spacecraft mass
SCA1B	A/B	Star camera data
TDP1B	A/B	intermediate clock solution
THR1B	A/B	Thruster activation data
TIM1B	A/B	Mapping of onboard to GPS time
TNK1B	A/B	Gas tank sensor data
USO1B	A/B	Oscillator frequency

required (Zehentner, 2017). These include the SOE file and external information, for example, if and in what configuration radio occultation is performed. Primary source of these GPS related data products are analysis center (ACs) of the International GNSS Service (IGS). For example, the Center for Orbit Determination in Europe (CODE) provides all relevant products in an operational manner.

Another key component in the processing of GRACE/GRACE-FO data is the atmosphere and ocean dealiasing product (AOD1B, Dobslaw et al., 2017). Primary purpose of this dataset is the reduction of high-frequency mass variations from the input data to reduce temporal aliasing effects. The potential coefficients are provided by GFZ in daily files with model values from 00:00 to 21:00 in 3-hourly intervals.

Earth orientation parameters (EOP) are required for the transformation between earth- and space-fixed reference frames. These are required to rotate orbits as well as background models, such as ocean tides, given in the earth fixed frame into the quasi-inertial frame where the computations are performed.

Finally, in order to derive mass estimates from the computed gravity field solutions, additional geophysical models are required for each specific subsystem. If, for example, continental water storage changes are of interest, other sources of mass change, such as GIA have to be reduced. Furthermore, it is reasonable to provide the water storage changes not in the center of mass frame of the whole earth, but rather in the center of mass of subsystem of interest. This is performed by adding degree 1 coefficients to the solution, which cannot be determined by GRACE alone, but require additional information (Bergmann-Wolf, Zhang, & Dobslaw, 2014; Rietbroek et al., 2009; Sun, Ditmar, & Riva, 2016; Swenson, Chambers, & Wahr, 2008). Table 3.2 lists all required input data in their respective latency. Next to observation data sets, (geophysical) models are required

Table 3.2.: Input data, latency and update period for all required input datasets.

Category	Product	Provider	Nominal latency	Update period
GNSS	Rapid orbits	CODE/IGS	17-41 hours	daily
	Rapid clocks	CODE/IGS	17-41 hours	daily
	DCB	CODE	$\approx$ 4 days	monthly
	ANTEX	JPL	-	on demand
GRACE/	L1B	JPL	$\approx$ 17 hours	daily
GRACE-FO	AOD1B	GFZ	$\approx$ 6 hours	daily
	SOE	JPL	on demand	daily
EOP	Rapid EOP	IERS	predicted	daily

in the gravity field recovery process. The purpose of these models is on the one hand to perform signal separation, for example, remove effects from ocean and Earth tides, on the other hand models are required to reduce high-frequency signal which causes temporal aliasing. A non-exhaustive set of forces typically modelled in GRACE processing and examples for geophysical models which represent these forces can be found in Table 3.3. Some of these models are based on fixed sets of constants and require only the evaluation time (e.g., pole tide) as parameter. Others also depend on the satellite state (e.g., relativistic corrections), but generally the models themselves are static and require no updates. Two notable exceptions are the non-tidal atmosphere and ocean loading model AOD1B and the measured non-conservative forces. Both of these models are data driven, as AOD1B relies on ECMWF forcing data (Dobslaw et al., 2017) and the non-conservative forces are directly measured. The accelerometer data is contained in the L1B data stream, whereas AOD1B is provided by GFZ in an operational manner. In principle also the model representing Earth's static gravity field should be updated if it includes time-variable constituents. The reason behind this is that strictly co-estimated trend and annual signals are only valid for the time span of the input data. This is an important detail, especially for the Kalman filter approach as the Kalman solutions are constrained towards the background gravity field model. Since in NRT application one probably operates outside this interval, a regular update might become necessary in order to compensate for changes in long-term trend and annual signal.

3.2. Daily process flow and scheduling

In order to provide a structured process flow which is easy to automate, maintain, and possibly alter during an operational service a top down analysis of the gravity field recovery was performed. Starting with the final task, the upload of gridded water storage anomalies to a dedicated File Transfer Protocol (FTP) server, each processing step was recursively disaggregated into smaller parts. This resulted in a task sequence which is closely tied to the hierarchy of the input data starting from raw observation data (L1) over gravity field solutions in the form of potential coefficients (L2) to the final gridded product (L3). The flow chart in Figure 3.1 shows the task sequence for a single day. As depicted in this diagram all identified tasks roughly fit into one of four categories:

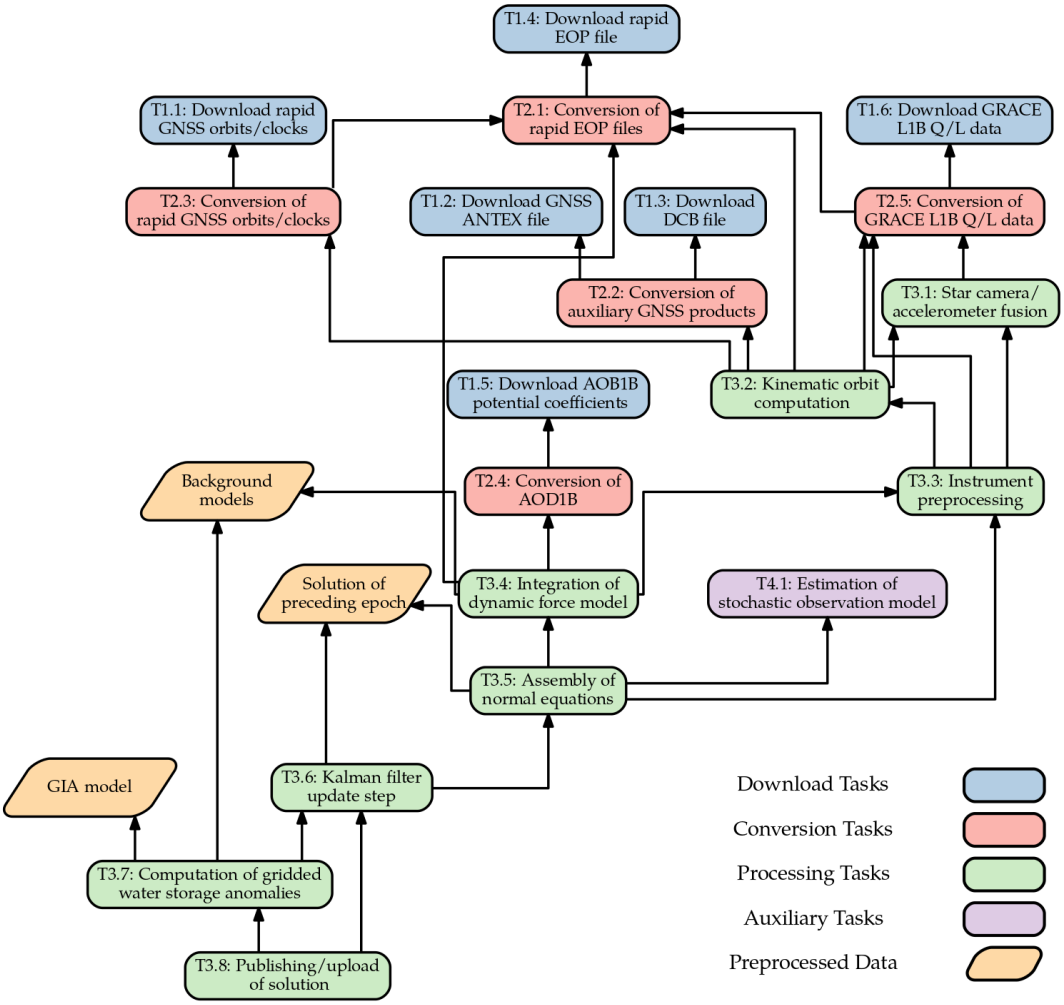

Figure 3.1.: Dependency graph for all tasks required to compute a daily gravity field solution.

Table 3.3.: Examples of force models used in GRACE gravity field recovery.

Force	Model (example)
Earth's static gravity field, trend, and annual oscillations	GOCO05s[a], GOCO06s[b]
Non-tidal atmosphere and ocean loading	AOD1B[c], MOG-2D[d]
Tidal effects from Moon, Sun, and planets	IERS2010[e]
JPL DE421 ephemerides[f]	
Atmospheric tides	AOD1B[c], van Dam and Ray (2010)
Ocean tides	FES2014b[g], EOT11a[h]
Solid Earth tides	IERS2010[e]
Pole tides	IERS2010[e]
Ocean pole tides	Desai (2002)
Non-conservative forces	ACC1B[i]
Relativistic corrections	IER2010[c]

[a]Mayer-Gürr and GOCO Team (2015), [b]Kvas, Brockmann, et al. (2019), [c]Dobslaw et al. (2017), [d]Carrère and Lyard (2003), [e]Petit and Luzum (2010), [f]Folkner, Williams, Boggs, Park, and Kuchynka (2009), [g]Carrere, Lyard, Cancet, and Guillot (2015), [h]Savcenko and Bosch (2012), [i]JPL (2018)

Acquisition Download, renaming, and possibly file format conversion of raw data files from external sources such as FTP servers.

Conversion Here, one or more raw input data files are converted into the internally used file formats. This might also include modification of the data, for example, the rotation of satellite orbits from terrestrial to the celestial reference frame or gap filling through interpolation.

Processing Computation of a new quantity from one or more input data sets. An example of such a task is the determination of kinematic satellite orbits from GPS data products and GRACE L1B quick look (Q/L) data.

Auxiliary Tasks which are either performed periodically in longer intervals (e.g. weekly) or irregularly (on demand). An example of such irregular task is the estimation of the stochastic observation model, which is performed in weekly intervals or if drastic change in instrument behavior occurred.

The level of disaggregation for each task was chosen as a trade-off between flexibility, which requires smaller work chunks, and manageable implementation complexity. An example of such a non-atomic processing step is the blunder detection in the GRACE L1B data. Here, the outlier detection was performed for all instruments in a single task, rather than treating each data file independently. Given the nature of the daily gravity field recovery, it suggested itself to define the tasks as processes which transform one or more input data files into one or more output data files. This is also very convenient from an implementation point of view, as it allows individual tasks to monitor the task-relevant

Table 3.4.: Description of Task 1.1 — Download of rapid GNSS orbits and clocks.

T1.1: Download rapid GNSS orbits/clocks			
Start:	16:00	Grace period:	5 days
Poll interval:	60 min	Scheduling:	daily
Dependencies:	-		
Input:	-		
Output:	Rapid GNSS ephemerides and clocks (uncompressed)		

progress, by simply checking whether a specific output file exists. A task can therefore be started by a job scheduler at the earliest time all preceding tasks are expected to finish. It then checks whether all necessary intermediate results are present, and if so, performs its own processing steps. Since delays must be expected in an operational environment, each task is assigned a specific grace period in which it checks whether the required input files are present. The length of the grace period has to be chosen in accordance with the required latency of the final product and take into account both idle and computation time of all subsequent steps. If the processing interval is shorter than the target latency of the service and an interdependency between epoch exists, multiple instances of the same task, albeit for different epochs, might also be active in parallel. From a monitoring perspective the partitioning of the process flow also has the advantage that each task can produce a log file which records the progress. This is key from a traceability point of view and allows for convenient notifications if a task failed. Another aspect to consider is the graphical representation of data time series. While this generally only provides a qualitative overview of the processing steps performed by a task, if a solution quality measure indicates anomalous input data, such figures can be used to quickly identify the problem. A practical example of how this graphical indication can be helpful was the pitch bias removal of the GRACE satellites on March 29, 2017 (Flechtner, Bettadpur, Kruizinga, Dahle, & Tapley, 2017). This event was only reported after the fact; however the changed attitude was clearly visible in the pointing angle time series (cf. also Chapter 4).

3.2.1. Data acquisition

The tasks in the data acquisition group generally follow a very similar structure. Their primary goal is to check remote locations, such as FTP servers, and download the specified raw data files. Some of the download tasks also directly uncompress archive files and pre-select files for further processing. This is, for example, the case for the GRACE L1B Q/L data, where all data and metadata files are provided as a single archive.

The first group of tasks described here consists of the acquisition of GNSS orbits and clocks (T1.1, cf. Table 3.4), the ANTEX file update (T1.2, cf. Table 3.5) and the download of the DCB (T1.3, cf. Table 3.6). GNSS orbits and clocks are fundamental for the determination of a GNSS receiver position (Teunissen & Montenbruck, 2017). The IGS and the contributing ACs provide these data sets in an operational manner with different

Table 3.5.: Description of Task 1.2 — Download of GNSS ANTEX file.

T1.2: Download GNSS ANTEX file			
Start:	17:00	Grace period:	14 days
Poll interval:	60 min	Scheduling:	daily
Dependencies:	-		
Input:	-		
Output:	GNSS ANTEX file		

Table 3.6.: Description of Task 1.3 — Download of differential code biases (DCB).

T1.3: Download DCB file			
Start:	17:00	Grace period:	14 days
Poll interval:	60 min	Scheduling:	25th DOM
Dependencies:	-		
Input:	-		
Output:	DCB files		

latencies and accuracies. There are ultra-rapid ephemerides and clocks for real-time applications (predicted, $\approx 3 - 9$ hours), rapid products ($\approx 17 - 41$ hours) for near real-time applications and final products ($\approx 12 - 18$ days) for post-processing applications (*IGS Quality of Service Fact Sheet*, 2013). For the application at hand the rapid products are suitable, given their latency. The GNSS ANTEX file contains information about the ACV of the transmitting satellite required for PPP. These satellite ACV are estimated in conjunction with satellite orbits, clocks and a global station network (e.g., Schmid, Steigenberger, Gendt, Ge, & Rothacher, 2007). This file is updated regularly when new receiver or satellite antenna values become available. Therefore, one has to either compare the contents of the local and remote files in order to detect changes, or download the remote file before processing regardless of whether a change occurred. The DCB are estimated monthly using the last 30 days of GNSS observation data (e.g., Montenbruck, Hauschild, & Steigenberger, 2014, and references therein). They are usually published within the first days of the following month. Since the monthly update interval does not align well with daily NRT applications, the latest DCB estimates are taken as the best information available.

Another critical dataset for the processing of GRACE data are observations of the EOP. This stems from the fact that the functional model based on the equation of motion is expressed in the (quasi-) inertial reference frame, whereas some input data sets and models are given in an Earth fixed frame. In order to connect these two coordinate frames, a rotation matrix based on a mathematical model (Petit & Luzum, 2010; Seidelmann, 1982) and observation based corrections are required. These corrections are based on a variety of space geodetic techniques (Bizouard, Lambert, Gattano, Becker, & Richard, 2019) and provided through the International Earth Rotation and Reference Systems Service (IERS, Dick & Richter, 2004). Similar to the GNSS products provided by the IGS and contributing ACs, the IERS also offers data products with different latencies. For the GRACE NRT application, the rapid time series consisting of quick-look daily EOP estimates based on

Table 3.7.: Description of Task 1.4 — Download of rapid EOP.

T1.4: Download rapid EOP file			
Start:	17:00	Grace period:	5 days
Poll interval:	60 min	Scheduling:	daily
Dependencies:	-		
Input:	-		
Output:	Rapid EOP XML file (time-stamped)		

very long baseline interferometry (VLBI) 24-hour sessions, GPS, and atmospheric angular momentum data is the best fit. The rapid data product uses observation data available up to the current epoch if possible, and predicts the following epochs. It features a daily update interval where the data file is updated in-place (i.e. overwritten) on the remote location and spans 181 days (from 90 days in the past to 90 days into the future). This update happens regardless of the amount of new data available, which means that there is essentially no latency, as the current file always represents the best EOP estimate. Since this data product employs backward smoothing, data points in the past change over time. To ensure a traceable and reproducible processing chain, the data files are time-stamped once downloaded (see Table 3.7). This means the for each (daily) processing epoch a dedicated EOP file is stored.

The AOD1B is a fundamental part of GRACE processing, and provides a priori information about high-frequency temporal variations in the Earth's gravity field caused by mass redistribution in atmosphere and ocean. It is based on analysis and forecast data from the European Centre for Medium-Range Weather Forecasts (ECMWF) and ocean bottom pressure from a global ocean circulation model that is consistently forced with ECMWF atmospheric data. Its main purpose is to reduce sub-monthly gravity field variations to reduce temporal aliasing in the standard monthly GRACE solutions. GFZ provides this dataset in an operational manner in the framework of the GFZ operational Earth System Model (GFZESM) (cf. Dill & Dobslaw, 2013; Dill, Dobslaw, & Thomas, 2017). AOD1B data files are updated daily and are available through GFZs Information System and Data Center for geoscientific data (ISDC). The download and uncompressing of these files is handled by task T1.5 (cf. Table 3.8). In a single file, non-tidal coefficients for four individual components denoted as ATM, OCN, GLO, and OBA are provided. The effects of the atmosphere are contained in the ATM coefficients. This includes the contribution of atmospheric surface pressure over the continents, the static contribution of atmospheric pressure to ocean bottom pressure and the much weaker contribution of upper-air density anomalies over continents and oceans. OCN contains the contribution of the dynamic ocean to ocean bottom pressure. The dealiasing product used in GRACE/GRACE-FO processing is given by the GLO coefficients which constitutes the sum of ATM and OCN. Finally, OBA is zero over the continents and provides the simulated ocean bottom pressure that includes air and water contributions. The difference between OBA deviates and GLO over the ocean domain is the disregard of the small contribution of upper-air density anomaly contributions to the external gravity field in the OBA data set.

The core data set for GRACE NRT processing is naturally the data stream of the satellite

Table 3.8.: Description of Task 1.5 — Download of AOD1B.

T1.5: Download AOD1B potential coefficients			
Start:	10:00	Grace period:	5 days
Poll interval:	60 min	Scheduling:	daily
Dependencies:	-		
Input:	-		
Output:	AOD1B potential coefficients		

Table 3.9.: Description of Task 1.6 — Download of GRACE L1B Q/L data.

T1.6: Download GRACE L1B Q/L data			
Start:	17:00	Grace period:	5 days
Poll interval:	60 min	Scheduling:	daily
Dependencies:	-		
Input:	-		
Output:	Raw GRACE L1B Q/L data files (uncompressed)		

mission itself. Within the L1B data archive, all observations and auxiliary housekeeping data collected during a single day are contained. For NRT applications, the standard L1B data files cannot be used, as they exhibit a varying latency of 1-2 months for GRACE and 2-3 weeks for GRACE-FO. Rather, the L1B Q/L data stream, which is not publicly available, is required for low-latency use cases. The file format for the Q/L data is nearly identical to the final L1B product, however it deviates in a few critical places, as not all post-processing steps have been applied yet (cf. T2.5, Table 3.14). Specifically, the reduced-dynamic orbit is given in 60 second sampling rather than 5 second sampling in the final product. It is also briefly noted that due to the time tag correction, which also depends on the GPS receiver clock error, differences in the data files between Q/L and final have to be expected for all sensors. Typically, the data is available $\approx$ 17 hours after the latest measured epoch with daily update intervals. Task 1.6 (see Table 3.9), is responsible for the download and unpacking of the data file archive.

3.2.2. File format conversion

To alleviate further processing, the downloaded raw data files are converted into consolidated file formats which are tailored to the processing software. The focus here no longer lies on human readability, but more so on efficient storage and read/write operations. Thus, most raw text files are converted from American Standard Code for Information Interchange (ASCII) to binary format, or machine readable text formats such as in Extensible Markup Language (XML), which can be efficiently parsed. This also allows for same data types of different sources to be coerced into a single file format (e.g., GNSS satellite orbits and GRACE orbits), which increases the reusability of source code.

Table 3.10.: Description of Task 2.1 — Conversion of rapid EOP files.

T2.1: Conversion of rapid EOP files			
Start:	17:00	Grace period:	2 days
Poll interval:	10 min	Scheduling:	daily
Dependencies:	T1.4		
Input:	Rapid EOP XML file (T1.4)		
Output:	EOPs in internal format		

Table 3.11.: Description of Task 2.2 — Conversion of auxiliary GNSS products.

T2.2: Conversion of auxiliary GNSS products			
Start:	17:00	Grace period:	2 days
Poll interval:	10 min	Scheduling:	daily
Dependencies:	T1.2, T1.3		
Input:	GNSS ANTEX file (T1.2), GNSS DCB files (T1.3)		
Output:	Antenna definitions and DCB files in internal format		

The conversion of the rapid EOP file (cf. Table 3.10) is essentially only a format conversion from the IERS XML format to a XML format understood by the processing software. Values of the EOP time series are not changed during this step.

During the conversion of the auxiliary GNSS data products (T2.2, cf. Table 3.11), the ANTEX and DCB files are parsed. For each pseudorandom noise number (PRN), a file which contains the mapping to a physical satellite represented by the space vehicle identifier (SV ID) based on time is created. This is then the key to properly associate the satellite ACVs, which are stored per SV ID, to the PRN during further GNSS processing. Similarly, a file for each PRN which contains the current DCB estimate is created.

GNSS orbits and clocks are also stored per PRN after they are extracted from the ephemeris and clock files respectively (cf. Table 3.12). Since the orbits are given in the terrestrial reference frame, the previously converted EOPs (T2.1) are used to rotate the positions into the celestial reference frame.

The raw data files of AOD1B contain potential coefficients with a sampling of 3 hours from 00:00 to 21:00. To avoid redundant information at the midnight epochs, the values

Table 3.12.: Description of Task 2.3 — Conversion of rapid GNSS orbits/clocks.

T2.3: Conversion of rapid GNSS orbits/clocks			
Start:	17:00	Grace period:	2 days
Poll interval:	10 min	Scheduling:	daily
Dependencies:	T1.1, T2.1		
Input:	EOPs (T2.1), raw GNSS orbits/clocks (T1.1)		
Output:	GNSS orbits and clocks in internal format		

Table 3.13.: Description of Task 2.4 — Conversion of AOD1B.

T2.4: Conversion of AOD1B			
Start:	17:00	Grace period:	2 days
Poll interval:	10 min	Scheduling:	daily
Dependencies:	T1.5		
Input:	Raw AOD1B potential coefficients (T1.5)		
Output:	AOD1B as linear splines of potential coefficients from 00:00 to 24:00 with 3 hour node interval.		

Table 3.14.: Description of Task 2.5 — Conversion of GRACE L1B Q/L data.

T2.5: Conversion of GRACE L1B Q/L data			
Start:	17:00	Grace period:	2 days
Poll interval:	10 min	Scheduling:	daily
Dependencies:	T1.6, T2.1		
Input:	EOPs (T2.1), raw GRACE L1B Q/L data (T1.6)		
Output:	Accelerometer data (ACC1B), GPS receiver observations (GPS1B), dynamic orbits (GNV1B, resampled to 5 seconds), satellite velocities (from dynamic orbit), satellite tracking data and corrections (KBR1B), attitude data (SCA1B) in internal format		

at 24:00 are omitted in the original files. For the GRACE processing, these epochs are however required during the gravity field recovery process. The value at 24:00 was computed by forming the average over the 8 given data points (from 00:00 to 21:00). The resulting 9 sets of potential coefficients are then interpreted as nodal points of linear basis splines and stored as the results of T2.4 (cf. Table 3.13).

For the conversion of the GRACE L1B data the output of T1.6 and T2.1 is required. Equivalent to the GNSS orbits, the GRACE dynamic orbits are also stored in the terrestrial reference frame. To rotate the epochs, the EOPs of T2.1 are used. Compared to the final L1B data set, where the dynamic orbits are given with a 5 seconds sampling, the Q/L dynamic orbit positions are given every minute. To resample to Q/L orbits to 5 seconds, a polynomial of degree 15 is used. For all other data files, T2.5 (cf. Table 3.14) simply consists of a file format conversion, where no modification to the data is performed. This implies that the quality flag given in the L1B files are fully ignored.

3.2.3. Data processing

The main purpose of the star camera/accelerometer fusion (Table 3.15) is to improve the satellite attitude by supporting the absolute attitude measured by the star cameras with

Table 3.15.: Description of Task 3.1 — Star camera/accelerometer fusion.

T3.1: Star camera/accelerometer fusion			
Start:	17:00	Grace period:	2 days
Poll interval:	10 min	Scheduling:	daily
Dependencies:	T2.5		
Input:	Star camera data, accelerometer data, dynamic orbits (T2.5)		
Output:	Smoothed attitude product, smoothed K-band antenna center correction		

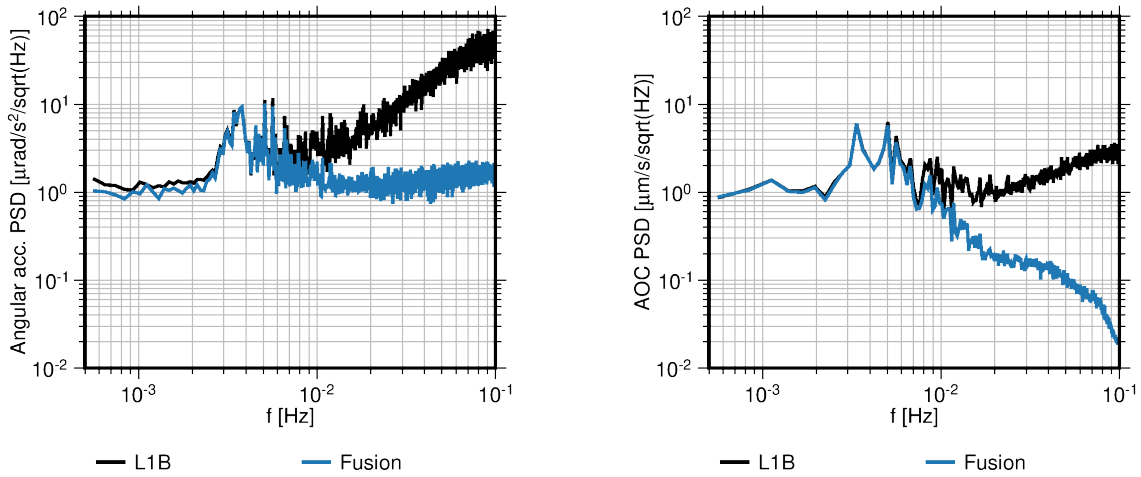

(a) PSD of angular acceleration (pitch)

(b) PSD of antenna offset correction

Figure 3.2.: Effect of the combination of star camera data with angular accelerations measured by the onboard accelerometer on the satellite attitude (left) and the antenna offset correction (AOC, right).

angular accelerations measured by the onboard accelerometer. This not only results in a reduction of high frequency noise in the combined attitude product (Klinger, 2018), but also allows to fill gaps in the star camera observations with a data driven approach, rather than simple interpolation. Since the K-band antenna offset correction (AOC) also depends on the measured satellite attitude (Horwath, Lemoine, Biancale, & Bourgogne, 2011), any improvements in the attitude determination also benefit the intersatellite ranging observations. The low pass filter effect for both attitude and AOC is clearly visible in their respective power spectral densities shown in Figure 3.2.

Kinematic orbits are a purely geometric quantity and provide information about the absolute position of the satellites. To compute the kinematic orbit positions, precise point positioning (PPP) after the approach by Zehentner and Mayer-Gürr (2016) is performed. Next to the code and phase observations recorded by the GPS receiver aboard GRACE, the GNSS constellation in the celestial reference frame, the clock product, and additional telemetry from the GRACE satellites is required. This primarily consists of the satellite attitude derived in task T3.1 to relate the observations to the satellites' center of mass rather than to the GPS antenna phase center. Further information about if and in which

Table 3.16.: Description of Task 3.2 — Kinematic orbit computation.

T3.2: Kinematic orbit computation			
Start:	17:00	Grace period:	2 days
Poll interval:	10 min	Scheduling:	daily
Dependencies:	T2.1, T2.2, T2.3, T2.5, T3.1		
Input:	EOPs (T2.1), auxiliary GNSS products (T2.2), GNSS orbits/clocks(T2.3), GPS receiver observations, dynamic orbits (T2.5), smoothed attitude product (T3.1)		
Output:	Kinematic orbit positions, corresponding 3×3 covariance matrices		

Table 3.17.: Description of Task 3.3 — Instrument preprocessing.

T3.3: Instrument preprocessing			
Start:	17:00	Grace period:	2 days
Poll interval:	10 min	Scheduling:	daily
Dependencies:	T2.5, T3.1, T3.2		
Input:	GRACE L1B Q/L data (T2.5), smoothed attitude product (T3.1), kinematic orbit positions (T3.2)		
Output:	Cleaned and synchronized GRACE L1B Q/L data (large outliers and yaw turns removed, accelerometer precalibrated)		

configuration radio occultation is performed is required as this influences the antenna phase centers (Zehentner, 2017). Compared to the CODE final products, where post-processed 5 second GPS clocks are available, the CODE rapid constellation only provides clocks with 30 second sampling interval (Dach et al., 2018). It was therefore decided to not use the full 10 second code/phase observations contained in the GRACE L1B data, but to only process epochs where a clock estimate is available. The derived orbits are later used as observations in the gravity field recovery process. There, in order to find an appropriate weighting for the positions with respect to the intersatellite ranging observations, not only the 3D positions of the satellites are determined, but also the corresponding precision represented by the 3×3 covariance matrix obtained during the PPP process (cf. Table 3.16).

After both the smoothed satellite attitude and the kinematic orbit positions have been determined, all GRACE L1B Q/L datasets required for further processing are subjected to a blunder detection represented by task T3.3 (see Table 3.17). The accelerometers are precalibrated using the values from Technical Note 2 (TN-02, Bettadpur, 2009). Then, values larger than 10^3 nm/s^2 are discarded. Furthermore, epochs at the beginning and end of satellite yaw-turns are also excluded. Finally, all epochs which do not have a simultaneous intersatellite ranging, accelerometer and attitude measurement are excluded from further processing. The remaining epochs are then divided into contiguous segments

Table 3.18.: Description of Task 3.4 — Integration of dynamic force model.

T3.4: Integration of dynamic force model			
Start:	17:00	Grace period:	2 days
Poll interval:	10 min	Scheduling:	daily
Dependencies:	T2.1, T2.4, T3.3		
Input:	EOPs (T2.1), AOD1B (T2.4), smoothed attitude product, accelerometer data, kinematic orbit positions, satellite tracking data and corrections (cleaned, T3.3), gravity field background models		
Output:	Dynamic force model (variational equations), integrated dynamic orbit, recomputed antenna center offset correction		

Table 3.19.: Description of Task 3.5 — Assembly of normal equations.

T3.5: Assembly of normal equations			
Start:	17:00	Grace period:	2 days
Poll interval:	10 min	Scheduling:	daily
Dependencies:	T3.3, T3.4, T4.1		
Input:	Smoothed attitude product, accelerometer data, kinematic orbit positions, satellite tracking data and corrections (cleaned, T3.3), dynamic force model (variational equations, T3.4), stochastic observation model (T4.1), gravity field solutions from previous epoch		
Output:	daily normal equation		

with a maximum length of 3 hours, so called "arcs", for further processing. Also, the sampling of the kinematic orbit positions is reduced to 300 seconds, which reduces the computational burden and the information contribution to the gravity field estimates. This improves the solutions, an effect which has also been observed by other GRACE processing centers (Meyer, Jäggi, Jean, & Beutler, 2016), however is not fully understood. A key component and the initial step of the gravity field recovery process is the integration of the dynamic force model, which constitutes the solution of the variational equations. All background models are evaluated at approximate orbit positions given by the GRACE L1B dynamic orbit, then an initial dynamic orbit is integrated and the corresponding state transition matrix is computed. The initial state of this orbit is then fitted to both kinematic orbit positions and intersatellite ranging observations. This brings the orbit closer to the actual satellite trajectory and servers as starting point for the next orbit integration. The procedure is stopped once the maximum orbit difference between two iteration steps is below the μm level, which is typically reached after 2-3 iterations.

Once the dynamic force model is determined, the system of normal equations can be assembled. Next to the functional model represented by (2.12), another integral part to

this processing step is the stochastic observation model. The covariance functions of all observation groups (kinematic orbit positions and intersatellite ranging observations) are assumed to be known from task T4.1 (cf. Table 3.23). In order to determine appropriate weights for the observations, variance component estimation (VCE, e.g., Koch & Kusche, 2002) is employed. This allows the determination of the relative weighting of the 3 hourly data batches and possibly identify erroneous observations. Basis for the VCE is the normal equation representation of the Kalman filter update step (2.59), which can be written more concisely as

$$[\mathbf{N}_i + \hat{\mathbf{\Sigma}}^{-1}_{\mathbf{x}_i^-}]\mathbf{x}_i^+ = \mathbf{n}_i + \hat{\mathbf{\Sigma}}^{-1}_{\mathbf{x}_i^-}\mathbf{x}_i^- . \tag{3.1}$$

As previously stated, all observations within one day are divided into contiguous segments with a maximum length of 3 hours. If all observations in one day are available, and no data gaps are present this results in 8 different observation groups. In practice however, this number, denoted J will vary depending on data availability and data gaps. For each of these segments, which are treated as uncorrelated, a variance factor σ_j^2 is set up. The covariance matrix $\mathbf{\Sigma}_{\mathbf{l}_i^j}$ of the observations $\mathbf{l}_i^j$ of each segment is assumed to be known, thus only the relative weighting has to be determined. The system of normal equations of each segment is then given by

$$\mathbf{N}_i^j \mathbf{x}_i^+ = \mathbf{n}_i^j, \tag{3.2}$$

where i denotes the Kalman filter epoch and the superscript j denotes the data batch within the corresponding interval. An additional variance factor $\sigma^2_{\mathbf{x}^-}$ is set up for the pseudo-observations of the initial state. Applying all these assumptions to (3.1), leads to the system of normal equations

$$\left[\sum_{j=0}^{J-1} \frac{1}{\sigma_j^2}\mathbf{N}_i^j + \frac{1}{\sigma^2_{\mathbf{x}^-}}\hat{\mathbf{\Sigma}}^{-1}_{\mathbf{x}_i^-}\right]\mathbf{x}_i^+ = \sum_{j=0}^{J} \frac{1}{\sigma_j^2}\mathbf{n}_i^j + \frac{1}{\sigma^2_{\mathbf{x}^-}}\hat{\mathbf{\Sigma}}^{-1}_{\mathbf{x}_i^-}\mathbf{x}_i^- . \tag{3.3}$$

The variance components σ_j^2 and $\sigma^2_{\mathbf{x}^-}$ are determined by iteratively solving (3.3) and updating their values with

$$\sigma_j^2 := \frac{q_j}{r_j}. \tag{3.4}$$

Here, q_j is the square sum of the residuals for observation group j with

$$q_j = \mathbf{x}_i^{+^T}\mathbf{N}_i^j\mathbf{x}_i^+ - 2\,\mathbf{n}_i^{j^T}\mathbf{x}_i^+ + \mathbf{l}_i^{j^T}\mathbf{\Sigma}^{-1}_{\mathbf{l}_i^j}\mathbf{l}_i^j \tag{3.5}$$

and r_j is the redundancy of the n_j observations with

$$r_j = n_j - \frac{1}{\sigma_j^2}\mathrm{tr}\left\{\left[\sum_{j=0}^{J-1}\frac{1}{\sigma_j^2}\mathbf{N}_i^j + \frac{1}{\sigma^2_{\mathbf{x}^-}}\hat{\mathbf{\Sigma}}^{-1}_{\mathbf{x}_i^-}\right]^{-1}\mathbf{N}_i^j\right\}. \tag{3.6}$$

Table 3.20.: Description of Task 3.6 — Kalman filter update step.

T3.6: Kalman filter update step			
Start:	17:00	Grace period:	2 days
Poll interval:	10 min	Scheduling:	daily
Dependencies:	T3.5		
Input:	Daily system of normal equations (T3.5), gravity field solutions from previous epoch		
Output:	Updated state and corresponding covariance matrix, daily mean of background models		

Equivalently, the variance factor for the pseudo-observations of the predicted state is computed through

$$\sigma^2_{\mathbf{x}^-} := \frac{q_{\mathbf{x}^-}}{r_{\mathbf{x}^-}}, \tag{3.7}$$

with

$$q_{\mathbf{x}^-} = (\mathbf{x}_i^+ - \mathbf{x}_i^-)^T \hat{\boldsymbol{\Sigma}}^{-1}_{\mathbf{x}_i^-} (\mathbf{x}_i^+ - \mathbf{x}_i^-) \tag{3.8}$$

and

$$r_{\mathbf{x}^-} = m - \frac{1}{\sigma^2_{\mathbf{x}^-}} \operatorname{tr} \left\{ \left[\sum_{j=0}^{J-1} \frac{1}{\sigma_j^2} \mathbf{N}_i^j + \frac{1}{\sigma^2_{\mathbf{x}^-}} \hat{\boldsymbol{\Sigma}}^{-1}_{\mathbf{x}_i^-} \right]^{-1} \hat{\boldsymbol{\Sigma}}^{-1}_{\mathbf{x}_i^-} \right\} \tag{3.9}$$

respectively. Once the procedure is converged, the relative weights of all observations and the predicted state as well as the updated state $\mathbf{x}_i^+$ is obtained. In practice, it is however convenient to store the final system of normal equations given by

$$\mathbf{N}_i = \sum_{j=0}^{J-1} \frac{\sigma^2_{\mathbf{x}^-}}{\sigma_j^2} \mathbf{N}_i^{(j)} \quad \text{and} \quad \mathbf{n}_i = \sum_{j=0}^{J-1} \frac{\sigma^2_{\mathbf{x}^-}}{\sigma_j^2} \mathbf{n}_i^{(j)} \tag{3.10}$$

and perform the Kalman filter update in a separate processing step. The reason for additionally scaling the individual system of normal equations with the variance factor of the predicted state is that (2.59) can then be directly used, i.e. no information about the VCE has to be passed on to the Kalman filter update step.

In task T3.6 (cf. Table 3.20), the Kalman filter update step is performed. This essentially means the evaluation of (2.59). If no system of normal equations is available at the current epoch, e.g., because of missing data or a processing failure, only the prediction step is performed and the predicted state and its covariance matrix is seen as the best gravity field estimate for this epoch.

Based on the output of T3.6, task T3.7 (cf. Table 3.21) computes gridded water storage anomalies from the current gravity field estimate. Since the Kalman filter output is given relative to trend and annual signal of the background gravity field, these constituents

Table 3.21.: Description of Task 3.7 — Computation of gridded water storage anomalies.

T3.7: Computation of gridded water storage anomalies			
Start:	17:00	Grace period:	2 days
Poll interval:	10 min	Scheduling:	daily
Dependencies:	T3.6		
Input:	Kalman filter solution, daily mean of AOD1B (T3.6), background gravity field, GIA model		
Output:	Gridded water storage anomalies (geocenter and GIA corrected)		

Table 3.22.: Description of Task 3.8 — Publishing/upload of solution.

T3.8: Publishing/upload of solution			
Start:	17:00	Grace period:	2 days
Poll interval:	10 min	Scheduling:	daily
Dependencies:	T3.6, T3.7		
Input:	Kalman filter solution, gridded water storage anomalies		
Output:	-		

are restored first. Then non-hydrological signals such as GIA are removed. The reduced potential coefficients are subsequently propagated to equivalent water heights on a 1×1 degree grid by evaluating (1.6). In order to transform the gridded water storage anomalies into the appropriate coordinate system, degree 1 coefficients determined using the approach of Swenson et al. (2008) are added to the solution.

The last step (T3.8, Table 3.22) in each daily processing schedule is the upload of both the estimated potential coefficients and gridded water storage anomalies to a remote location for further processing. Next to file handling, that is, creating a compressed archive of the output files, this task also categorizes each solution according to the GRACE contribution (cf. Section 3.3).

3.2.4. Auxiliary processing tasks

In order to compute an optimal least squares solution in a statistical sense, the covariance structure of the observations $\boldsymbol{\Sigma}_{\mathbf{l}}$ has to be known. While the instruments aboard the satellites are characterized reasonably well (e.g, Flury, Bettadpur, & Tapley, 2008; Frommknecht, Fackler, & Flury, 2006; Inácio, Ditmar, Klees, & Farahani, 2015; Meyer, Jäggi, & Beutler, 2012; Peterseim, 2014; Touboul, Foulon, Rodrigues, & Marque, 2004), the changing mission environment, for example, sensor degradation, increased drag due to orbit decay, and varying solar flux, suggests that a data driven determination of the measurement accuracy might provide better results. For the task at hand, a post-fit residual analysis using VCE as it is used in the ITSG-Grace processing was chosen. Here, only a brief summary of the methodology will be given, a detailed description of

Table 3.23.: Description of Task 4.1 — Estimation of stochastic observation model.

T4.1: Estimation of stochastic observation model			
Start:	9:00	Grace period:	-
Poll interval:	-	Scheduling:	weekly/on demand
Dependencies:	T3.3, T3.4		
Input:	Cleaned GRACE L1B Q/L data (T3.3) and dynamic force model (T3.4) from at least 14 of the previous 30 days		
Output:	Stochastic observation model (covariance functions for K-band range rates and kinematic orbit positions, valid until next update		

the algorithm can be found in Ellmer (2018, section 6.5). The covariance function of a wide-sense stationary process is connected to the process' power spectral density through the inverse Fourier transform (Pisarenko, 1973). Arranging both the covariance function of the process $c(\tau)$ for discrete time lags τ_j and the power spectral density (PSD) $P(f)$ for discrete frequencies f_k as column vectors $\mathbf{c}$ and $\mathbf{p}$ respectively allows to express this relationship as a matrix-vector product. Specifically, the covariance function $\mathbf{c}$ is given by

$$\mathbf{c} = \mathbf{F}^{-1}\mathbf{p}. \tag{3.11}$$

Here, $\mathbf{F}^{-1}$ is the inverse discrete Fourier transform (IDFT) matrix (Rao & Yip, 2000). More explicitly, the covariance function is the linear combination of N vectors, where N is the number of lags considered and $\mathbf{f}_k^{-1}$ is the $k-$th column of the IDFT matrix:

$$\mathbf{c} = \sum_{k=0}^{N-1} \mathbf{f}_k^{-1} P(f_k). \tag{3.12}$$

The underlying process is assumed to be wide-sense stationary, so its covariance matrix is symmetric with Toeplitz structure (Akaike, 1973). Since this means the covariance matrix is purely determined by a single vector, it is convenient to introduce the notation $\mathbf{T}\{\cdot\}$, which represents the Toeplitz matrix constructed from a column vector. Using this notation, the covariance matrix of the process can be written as $\mathbf{C} = \mathbf{T}\{\mathbf{c}\}$. For (3.12) this means that

$$\mathbf{C} = \mathbf{T}\{\mathbf{c}\} = \mathbf{T}\left\{\sum_{k=0}^{N-1} \mathbf{f}_k^{-1} P(f_k)\right\}, \tag{3.13}$$

which can be simplified to

$$\mathbf{C} = \sum_{k=0}^{N-1} \mathbf{T}\left\{\mathbf{f}_k^{-1}\right\} P(f_k), \tag{3.14}$$

Thus, the covariance matrix of the process can be expressed as the sum of Toeplitz matrices based on the columns of the IDFT-matrix, scaled by the PSD value of the corresponding

frequency. According to Koch (2004, chapter 36) this representation of a covariance matrix can be used to perform VCE. Specifically, the variance components $\sigma_k^2 = P(f_k)$ can be determined iteratively within the least squares adjustment which also yields the estimated potential coefficients, instrument calibration and satellite state parameters. The drawback of this approach is that a certain number of epochs are required in order to obtain a robust estimate of the PSD. Similar to the methods of Bartlett (Bartlett, 1948, 1950) and Welch (Welch, 1967), the VCE approach reduces the spectral resolution of the PSD estimates, for the benefit of increased redundancy. Here, the 3-hour arcs determine the spectral resolution, which results in spectrum from $f_0 = 0$ to $f_{N-1} = 0.1$ Hz for range rate observations and $f_0 = 0$ to $f_{N-1} \approx 1.7$ mHz for the kinematic orbits with a a frequency spacing $\Delta f \approx 0.1$ mHz. Since the fundamental assumption is the wide-sense stationarity of the process, any changes in sensor behavior which results in different noise characteristics can not be modeled by this approach. It is therefore necessary if such an event occurs, to split the input data into appropriate segments and perform a separate estimate for each resulting interval. For near real-time applications, this might not be possible. On the one hand, sudden changes in instrument behavior need to be detected first, on the other hand even if they are detected a re-estimation of the PSD might not be immediately possible due to a lack of observation data. Such an event occurred during the operational test run of the near real-time processing chain and is discussed in chapter 4.

3.3. Operational quality control and blunder detection

For the operational processing, an automated quality control and blunder detection is crucial for the delivery of a robust water storage product. In the case at hand, three measures of how blunders can be detected, treated, and communicated were implemented. The first measure to ensure a robust solution is the gross outlier detection performed in task T2.1 (cf. Table 3.10). The second measure undertaken is the adaptive relative weighting between observations and predicted state as described in task T3.3 (cf. Table 3.17). Closely tied to the relative weighting is the contribution of GRACE to the updated state parameters, which can give an overall impression of the data quality. Finally, a classification scheme based on the contribution measure was developed to communicate the solution quality to downstream users. The contribution of GRACE can be computed from the normal equation representation of the Kalman filter in (2.59). The solution to this system of normal equations is given by

$$\mathbf{x}_i^+ = [\mathbf{N}_i + \hat{\mathbf{\Sigma}}_{\mathbf{x}_i^-}^{-1}]^{-1}\mathbf{n}_i + [\mathbf{N}_i + \hat{\mathbf{\Sigma}}_{\mathbf{x}_i^-}^{-1}]^{-1}\hat{\mathbf{\Sigma}}_{\mathbf{x}_i^-}^{-1}\mathbf{x}_i^- . \tag{3.15}$$

Substituting $\mathbf{n}_i = \mathbf{N}_i\hat{\mathbf{x}}_i$, where $\hat{\mathbf{x}}$ is the unconstrained GRACE estimate for epoch i, yields

$$\mathbf{x}_i^+ = \underbrace{[\mathbf{N}_i + \hat{\mathbf{\Sigma}}_{\mathbf{x}_i^-}^{-1}]^{-1}\mathbf{N}_i}_{=\mathbf{R}_{\hat{\mathbf{x}}}}\hat{\mathbf{x}}_+ \underbrace{[\mathbf{N}_i + \hat{\mathbf{\Sigma}}_{\mathbf{x}_i^-}^{-1}]^{-1}\hat{\mathbf{\Sigma}}_{\mathbf{x}_i^-}^{-1}}_{=\mathbf{R}_{\mathbf{x}^-}}\mathbf{x}_i^- . \tag{3.16}$$

The matrices $\mathbf{R}_{x^-}$ and $\mathbf{R}_{\hat{x}}$ are known as resolution matrices (Jackson, 1972) and have already been used by Kurtenbach et al. (2012) to study the contribution of GRACE to the updated state. They can be interpreted as coefficients of a weighted mean between observations and predicted state. It can easily be verified that $\mathbf{R}_{x^-} + \mathbf{R}_{\hat{x}} = \mathbf{I}$ and thus

$$\mathrm{tr}\{\mathbf{R}_{x^-}\} + \mathrm{tr}\{\mathbf{R}_{\hat{x}}\} = m. \tag{3.17}$$

The quantity

$$c = \frac{1}{m}\mathrm{tr}\{\mathbf{R}_{\hat{x}}\} \cdot 100 \tag{3.18}$$

then represents the total contribution of GRACE to the updated state parameters in percent with $c \in [0, 100)$. Since the relative weights of the GRACE observations and the predicted state are determined through VCE, where bad data patches are downweighted, a low contribution value is a strong indicator for erroneous observations in the current state estimate. The extreme case where $c = 0$ happens when no observations are available, i.e. the solution is predicted. A significantly lower value than a "standard solution" ($c \approx 14$), derived from historic data) therefore indicates a less trustworthy water storage estimate. For the operational processing a categorization scheme was implemented in task T3.8 (cf. Table 3.22) before a solution was uploaded. If GRACE has a significant non-zero contribution, the solution was flagged with "A". If the solution is predicted or the contribution is close to zero, but there has been a state update in the last three days, the solution was flagged with "B". In the case where no GRACE information was available at the current epoch and the last three days, the solution was flagged with "C". The threshold values would typically be derived from a historical data set, for the case at hand this was not possible, since the data characteristics towards the end of the GRACE mission was expected to vastly differ from the rest of the observation period. Therefore, a conservative empirical value ($c_0 = 1$) was chosen until a large enough sample for a proper characterization of the contribution during the operational test run was feasible.

These quality control measures were tailored to the planned application of the daily water storage estimates. VCE reduces the weight of non-matching data batches, thus the overall contribution of GRACE is reduced, which results in a smaller state update. In combination with the exponential decay of the predicted state, the water storage estimate then tends towards zero. This in turn means that an underestimation of the global water storage is more likely. For the application at hand — the detection of extreme events — this is a reasonable outcome. Other applications might however require different or additional quality control measures.

Since the Kalman filter approach yields constraint gravity field estimates, which may hide unexpected features in the data due to the implicit filtering process, it was decided to also compute a "companion solution" based on the last five days of data. As opposed to the sophisticated Kalman filter process dynamic, a simple Kaula-type function was used to constrain the accumulated system of normal equations. While this yields a noisier gravity field estimate, it can reveal possible problems with the data which might be filtered out by the Kalman constraints. A comparison of a Kalman smoother estimate and the Kaula-type constraint can be seen in Figure 3.3. As the Kaula-type constraint

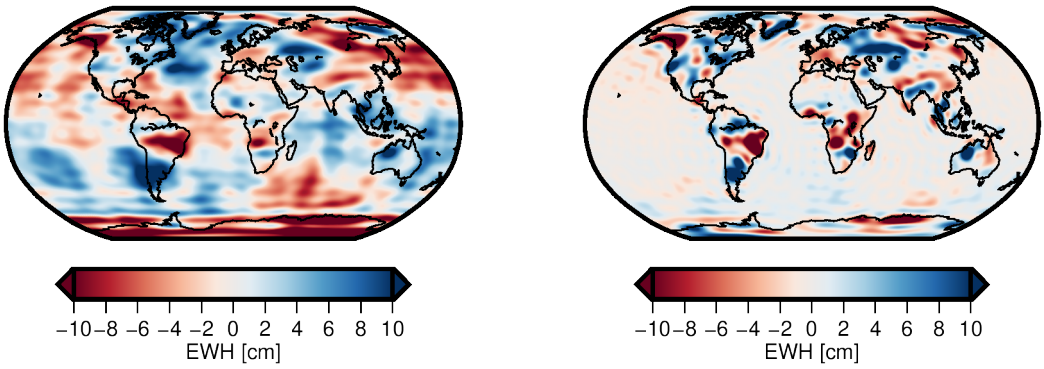

(a) Kaula-type

(b) Kalman smoother

Figure 3.3.: Comparison of a Kaula-type constraint solution using 5 days of data and the Kalman smoother estimate of the central epoch.

solution spans multiple Kalman filter epochs, the comparison is made with the central epoch, which is defined as the reference epoch. The effect of the different constraints can be clearly seen. While the large geophysical signals on the continents are similar, the Kalman filter has a stronger filter effect over the oceans. This is a direct consequence of the isotropic signal model of the Kaula-type constraint as opposed to the non-isotropic VAR process model. From an operational point of view, a companion solution of this form has the advantage that it is trivial to implement. All necessary input is readily available, since it is also basis for the primary gravity field solutions. Therefore, it can provide an additional, albeit qualitative, measure of the data characteristics with very little additional implementation and computational effort.

4. Test run of the EGSIEM Near Real-Time Service

4.1. Introduction and overview

Within the Horizon 2020 funded project European Gravity Service for Improved Emergency Management (EGSIEM), a technology demonstrator for a near real-time (NRT) service was established (Jäggi et al., 2019). The primary purpose of this service was to show the usefulness of gravity based indicators for flood and drought prediction. Its goal was to provide gridded water storage anomalies from daily gravity field solutions with a maximum latency of five days. For this purpose, two independent approaches were developed at the German Research Centre for Geosciences (GFZ, Gruber & Gouweleeuw, 2019) and TU Graz (TUG, presented in detail in chapter 3). These daily solutions served as input data for the derivation of flood and drought indicators at the EGSIEM Hydrological Service run at GFZ, with offline evaluation of the solutions through GNSS loading observations by the University of Luxembourg (Jäggi et al., 2019, section 6). Final user of these derived data products was the Center for Satellite based Crisis Information (ZKI) of the German Aerospace Center (DLR). The operational test run of the NRT- and dependent services was planned to start on April 2017 and run for 6 months. However, due to a battery failure on GRACE-B, the test run was cut short and ended with last available GRACE measurements on June 29th 2017. The daily process flow for the interconnected services started with acquisition of all required data to compute a daily gravity field solution (c.f. chapter 3). This step happened in parallel at GFZ and TUG as two independent gravity field solutions were produced by the respective processing centers. After the daily gravity field solutions were finished and converted to water storage anomalies, the dataset was uploaded for further processing. The Hydrological Service used this data to compute flood- and drought indicators which were then passed on to the ZKI for use in their remote sensing satellite tasking software. Here, the application was to potentially change the image acquisition scheme of the satellites to increase the number of scenes in affected areas, possibly even before the onset of a flood. A general flowchart of this process can be found in figure 4.1. The remainder of this chapter exclusively focuses on the operational gravity field processing performed at TUG.

4.2. Pre-operational simulations

As the health of the GRACE satellites was expected to further deteriorate in 2016 and 2017, a simulation study based on one year of (historic) data was conducted in mid-2016

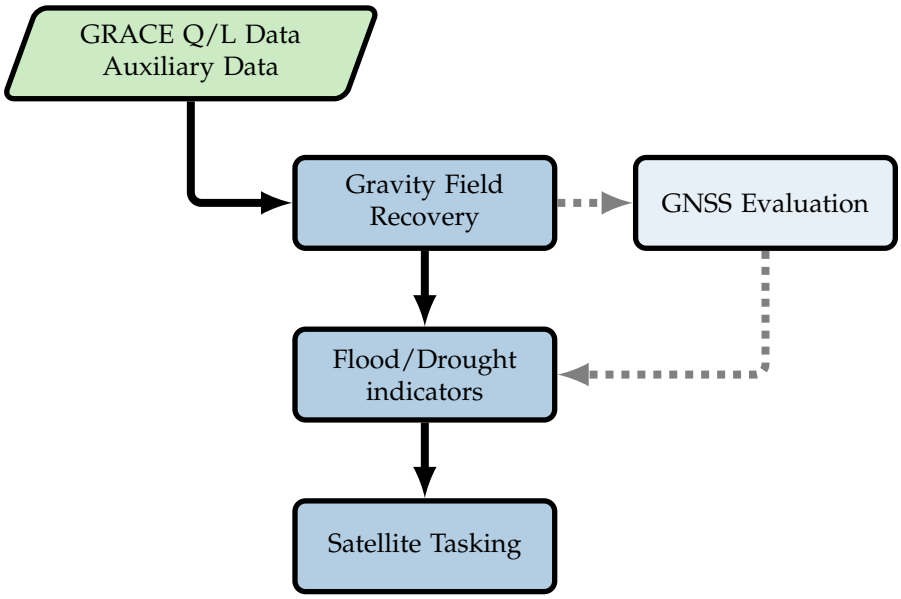

Figure 4.1.: Daily process flow of the EGSIEM NRT Service and related services. GNSS Evaluation was not performed operationally, but in offline (manual) mode.

to estimate the quality of the daily gravity solutions during the NRT Service test run. Two constraints were considered: measurements only in orbital segments where the satellites are in full sunlight, leading systematic data gaps and reduced observation count, as well as the unavailability of accelerometer measurements on GRACE-B. Both constraints were considered a direct cause of a battery cell failure, which happened on 17 September 2016 (Flechtner, Bettadpur, Kruizinga, Dahle, & Tapley, 2016b). The simulated data sets were generated by removing all measurements taken in Earth's shadow. To identify the affected observations, a shadow function based on a conical shadow model (Montenbruck & Gill, 2000, Fig. 3.4) was used. Figure 4.2 shows the distribution of the observations collected in sun- and shadow segments during nominal science operations. As is evident,

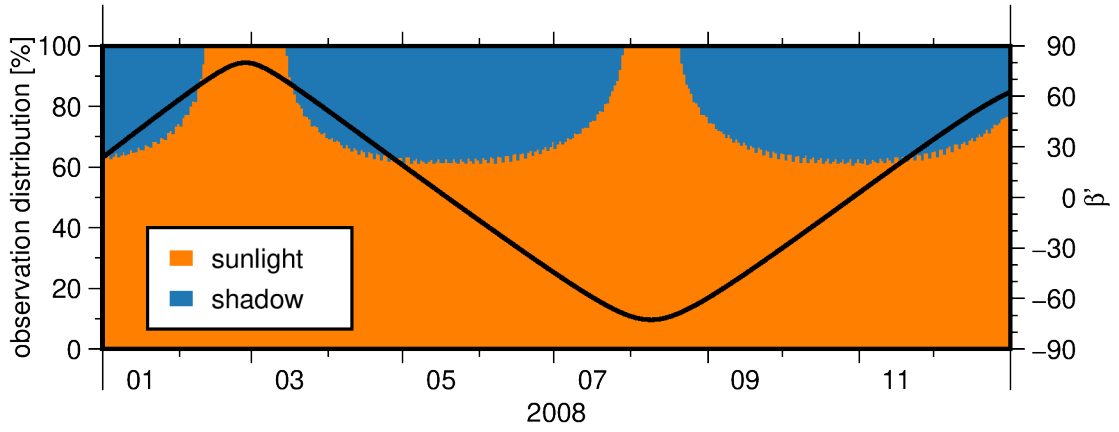

Figure 4.2.: Observation distribution in sun/shadow for the study period.

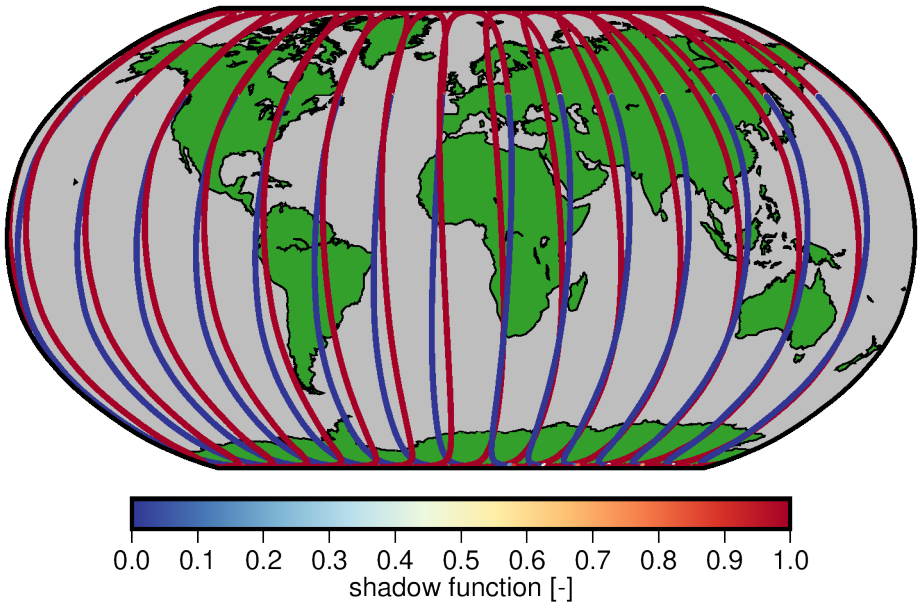

Figure 4.3.: Ground track and shadow function of the GRACE satellites for 15 May 2008.

this ratio depends on the orientation of the satellites' orbital plane with respect to the sun (β' angle), which is represented by the black line. During periods of low beta-prime angles ($|\beta'| < 25°$), the overall observation count is reduced by nearly 40%. Since whole data segments rather than single epochs will be lost when the satellites pass through Earth's umbra and penumbra, the effect these long data gaps have on the recovered gravity fields is of primary interest. Specifically, any change in the spectral characteristics represented by the maximum resolvable order has to be carefully reviewed. The extreme case of $\beta' = 0$ can be seen in Figure 4.3, where the ground track of the satellites for 15 May 2008 is shown. The color code of the ground track represents the shadow function of the satellite at the given epoch. Red colors mean the satellite is exposed to sunlight, while blue colors mark shadow crossings. As can be seen 15 unique equator crossings with observations still remain, even in time periods where $\beta' = 0$ and if only observations in sunlight are considered. Therefore, it can be concluded that the spatio-temporal sampling of GRACE does not change in these conditions, rather the redundancy of the solutions is decreased due to the lower observation count.

Further, the accelerometer measurements on GRACE-B were created by a rotating and time-shifting the corresponding GRACE-A data set. This approach corresponds to the one presented in Save, Bettadpur, and Tapley (2006). Following the battery cell failure on GRACE-B on 17 September 2016, there was a strong possibility that the accelerometer aboard the spacecraft would be kept offline for the remainder of the mission duration. It was therefore envisaged by JPL to include a so called "transplant" product, i.e. using the accelerometer measurements of GRACE-A for GRACE-B, into the L1B data stream (Frank Flechtner, personal communication, Flechtner, Bettadpur, Kruizinga, Dahle, & Tapley, 2016a). Since this official product would be based on L1A data, it was expected that the operational accelerometer transplant data would be of higher quality than the

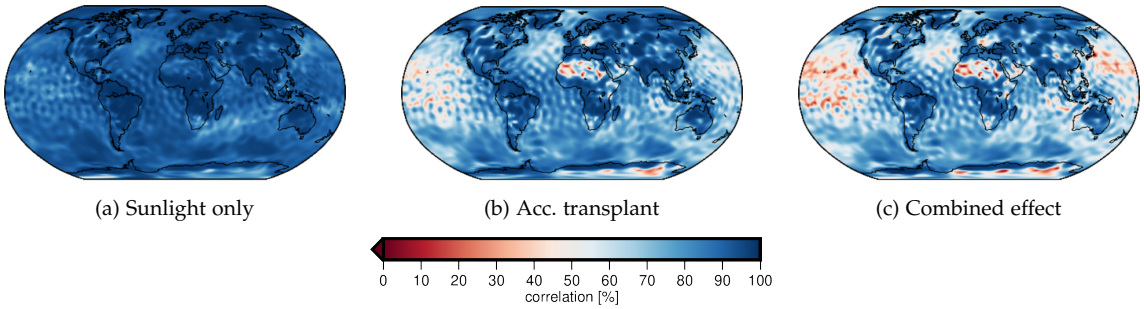

(a) Sunlight only (b) Acc. transplant (c) Combined effect

Figure 4.4.: Correlation with respect to ITSG-Grace2016 daily solutions for each of the computed time series: measurements in sunlight only (a), accelerometer transplant only (b), and combined effect (c).

one used in this study (Bandikova, McCullough, Kruizinga, Save, & Christophe, 2019). The results of this simulation study were therefore treated as a conservative estimate of the overall solution quality.

Based on these simulated data sets, three daily gravity field time series were generated: one for each constraint individually and additionally the combination of both. The original — unaltered — data was used as a benchmark. From these three time series and intercomparisons between the data sets, it was evident that the expected differences between the data available during the operational test run and nominal science operations will be dominated by the accelerometer transplant. This is supported by the correlation plots in Figure 4.4, which show decreasing similarity between the time series in areas where little signal, for example, the oceans or the Sahara desert, is expected. Fortunately, in large river basins the correlation remains high despite the combined effect of systematic data gaps and accelerometer transplant. When inspecting individual river basins (cf. Figure 4.5), it can be seen that the hydrological signal — for the most part — can however still be resolved on a reasonable quality level. The systematic data gaps introduced by only measuring in sunlight have a minor impact on the time series, while the accelerometer transplant does degrade the solutions in places.

4.3. Operational processing of daily gravity field solutions

Operational processing of GRACE quick-look data at TU Graz started on March 17 with the first available observations after the scheduled position switch of the spacecraft (Flechtner et al., 2017). The test run ended on June 29, with the last intersatellite measurements of the GRACE satellites before the decommissioning phase. During this period, a total of 105 daily gravity field solutions were computed in a fully automated manner.

The observations and background force models used for the test run were mostly consistent with the ITSG-Grace2016 processing (Mayer-Gürr et al., 2016), with two notable exceptions. AOD1B RL06 was used as atmosphere and ocean dealiasing product (as opposed to AOD1B RL05), and the Q/L version of the GRACE L1B was used (in contrast to L1B RL02). These changes were necessary to fulfill the 5-day latency required. Both L1B RL02 data and AOD1B RL05 have latencies far higher and were therefore

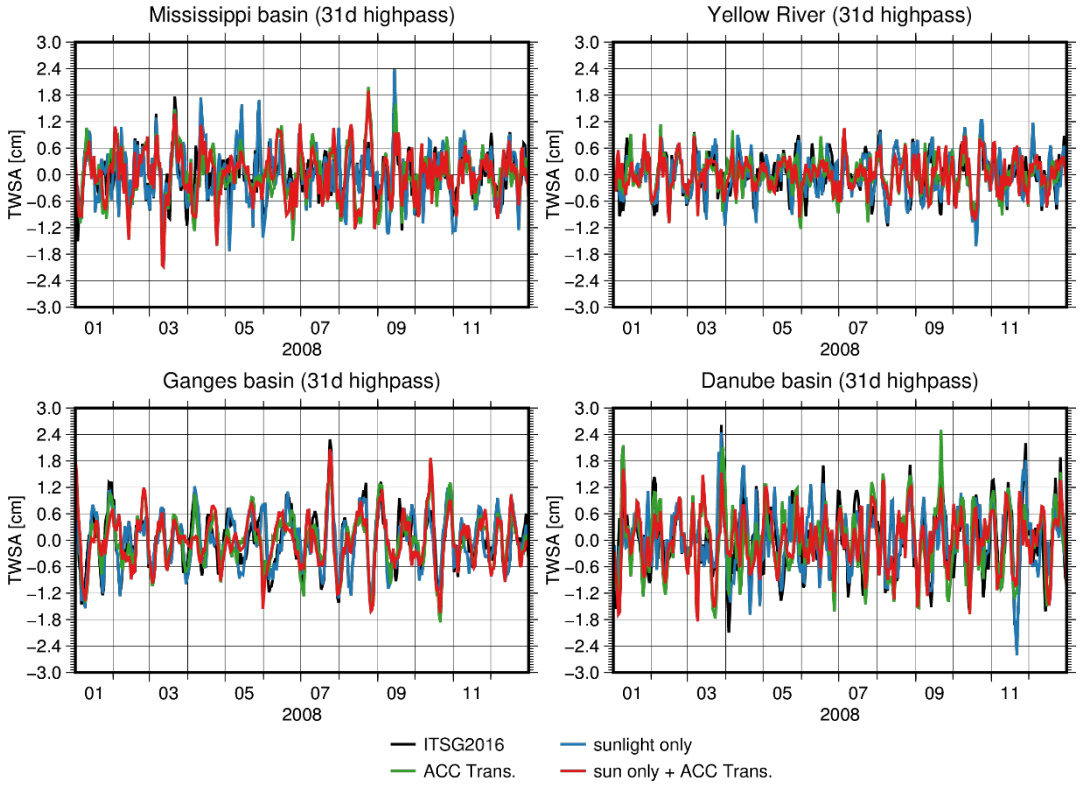

Figure 4.5.: Comparison of the impact of sunlight only and accelerometer transplant observations on catchment average time series.

Table 4.1.: Background force models used in the EGSIEM-NRT operation test run.

Force	Model
Earth's static gravity field, trend, and annual oscillations	GOCO05s[a]
Non-tidal atmosphere and ocean loading	AOD1B RL06[b]
Tidal effects from Moon, Sun, and planets	IERS2010[c]
JPL DE421 ephemerides[d]	
Atmospheric tides	van Dam and Ray (2010)
Ocean tides	EOT11a[e]
Solid Earth tides	IERS2010[c]
Pole tides	IERS2010[c]
Ocean pole tides	Desai (2002)
Non-conservative forces	measured by onboard accelerometer (L1B Q/L)
Relativistic corrections	IER2010[c]

[a]Mayer-Gürr and GOCO Team (2015), [b]Dobslaw et al. (2017), [c]Petit and Luzum (2010), [d]Folkner et al. (2009), [e]Savcenko and Bosch (2012)

unsuitable for operational purposes. For the same reason also the CODE rapid GPS orbits and clocks were used instead of the final version. A full list of background models is given in Table 4.1. GIA correction was performed using the model of A, Wahr, and Zhong (2012).

During the service run, infrastructure failures – an unplanned GRACE quick-look data server outage on May 21-22 - were handled in accordance with the predefined contingency plans and the software was able to recover automatically. In the week of May 15 to May 21, a hardware migration required a manual stop and restart of the software which however did not cause any delay in the gravity field computation. The number of available K-band observations was, as expected, strongly correlated with the orientation of the orbital plane to the sun. Starting in the middle of March with just above 40% of possible observations, the number of observations increased in April up to nearly full coverage on April 30. With increasing exposure to the sun due to the rising β' angle, full data coverage was reached in the middle of May. Data collection then slowly decreased throughout June back towards 50%. A key property for the stochastic model estimation is the length of the longest contiguous data segment, as it determines the spectral resolution of the estimated PSD (cf. Section 3.2.4). Since no measurements were collected in time spans where the satellites cross Earth's shadow, each 94 minute revolution would be split into two segments by a data gap for low β' angles. The evolution of the maximum contiguous data segment length can be seen in Figure 4.7. During phases where the maximum contiguous arc length was below 94 minutes, no once per revolution signal or its harmonics can be represented by the estimated PSD, as the frequency spacing is too coarse. Rather, once per revolution signals are smeared over neighboring frequencies due

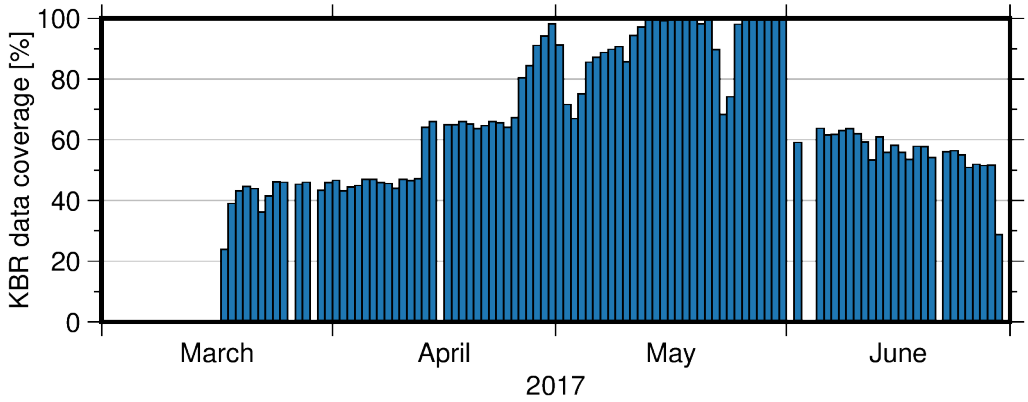

Figure 4.6.: Data coverage of K-band range rates with respect to a fully available observation set.

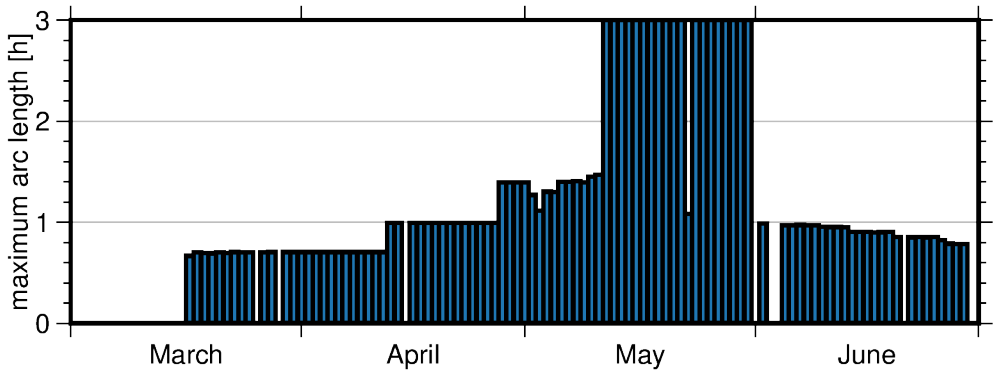

Figure 4.7.: Length of the longest contiguous data segment up to a maximum of 3 hours.

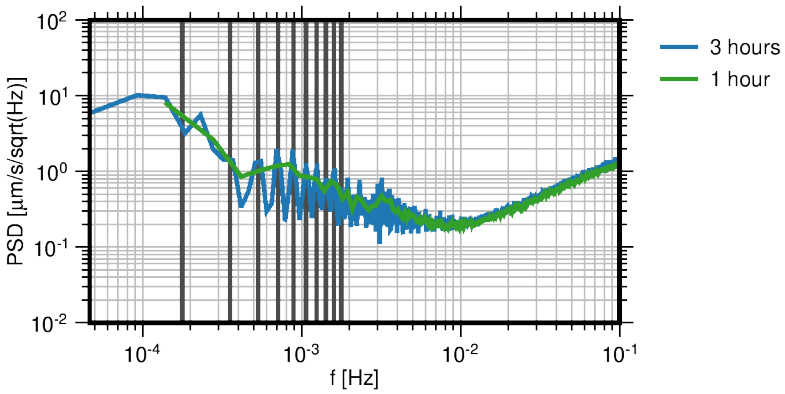

Figure 4.8.: Comparison of PSD estimates for different arc lengths. Multiples of the revolution period are depicted as vertical lines.

to the limited spectral resolution. This effect is exemplified in Figure 4.8, where two PSD estimates from identical range-rate residuals are compared. The only difference between the estimates is the chosen arc length of 1 and 3 hours respectively. As can be seen, the longer arc length allows the resolution of multiples-per-revolution signatures as opposed to the shorter arc length. There was only a very brief period from the middle to the end of May where continuous measurements were available. For most other days within the operational test run period the maximum arc length was at, or below, 1 hour.

Due to the long data gap before the start of the operational test run, the Kalman filter was initialized with $\mathbf{x}_{-1}^{+} = \mathbf{0}, \mathbf{x}_{-1}^{+} \sim \mathcal{N}(\mathbf{0}, \boldsymbol{\Sigma}_{\mathbf{w}}^{(0)})$ on March 16. The stochastic observation model for this initial period was taken from the last available full month, which was January 2017. This initial stochastic model was planned to be used until enough epochs for a stable re-estimation would be available. A first re-estimation for testing purposes was performed on March 23 based on the first 4 days of available data (March 17 to March 21). The results of this estimation were deemed reasonable and it was therefore decided to use this estimate, despite the limited amount of input data. The second re-estimation took place on March 26 which included 7 days of data, which was consistent with the estimate of March 23. After this initial phase, the determination of the stochastic model was scheduled weekly using the last 14 days of available data.

On March 29, the attitude of the spacecraft was changed by removing the pitch bias of the satellites. As a result, the pointing angle relative to the line of sight increased by approximately one degree. This resulted in a close agreement between the velocity vectors of the satellites and the $\pm\mathbf{x}$-axis of the satellite reference (body) frame. Since this also minimizes and homogenizes the cross section in flight direction between the satellites, the transplant of the accelerometer measurement on GRACE-A to GRACE-B, could be performed more easily (Gerard Kruizinga and Himanshu Save, personal communication, Flechtner et al., 2017). The drawback of this step was a higher impact of attitude noise on the ranging measurements, because the propagated attitude noise is proportional to the sine of the pointing angle. A schematic of the satellite before and after the pitch bias removal can be seen in Figure 4.9. The key here is that the range (or range-rate) between both satellites' KBR antenna phase center is measured, rather than the required distance

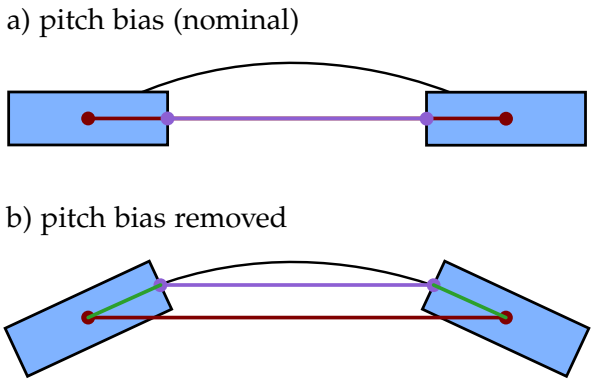

Figure 4.9.: Schematic representation of the relative orientation of the satellites during the mission period up to March 2017 (a) and during the last months (b).

(or distance change) between the satellites' center of mass. To correct for this discrepancy, a geometric correction based on the position of the KBR antenna phase centers has to be applied. The positions of these phase centers were determined in calibration procedures. Due to the large distance between the satellites, this antenna offset correction (AOC) can be applied by projecting the phase center vector onto the line of sight. For this projection, the attitude of the satellites is required, therefore the AOC not only depends on the antenna center positions, but also on star camera measurements and their respective errors. When reducing this correction to one dimension, as depicted in Figure 4.9, it can easily be seen that in this simplified setup, the AOC for ranges is given through

$$\rho_{\mathrm{AOC}} = \cos(\phi_A + \Delta\phi_A)p_A + \cos(\phi_B + \Delta\phi_B)p_B, \tag{4.1}$$

where $\phi_{A/B}$ is the pointing angle of the satellite, $\Delta\phi_{A/B}$ is the attitude error and $p_{A/B}$ is the distance between the center of mass and the antenna phase center. Applying covariance propagation to this expression and only considering attitude errors leads to

$$\sigma_{\rho_{\mathrm{AOC}}} = 2\sin(\phi_{A/B} + \Delta\phi_{A/B})p_{A/B} \cdot \sigma_{\Delta\phi_{A/B}}. \tag{4.2}$$

For simplicity it was assumed here that pointing angles, phase center offsets and attitude errors are identical for both satellites. This expression shows that a pointing angle increase of 1 degree raises the AOC magnitude by two orders of magnitude. Considering an attitude accuracy of 170 μrad (Inácio et al., 2015), the standard deviation of the AOC increases from $\approx$0.06 μm to $\approx$6 μm for ranges and from $\approx$0.02 $\mu m/s$ to $\approx$2 $\mu m/s$ for range rates. This means that the proposed precision of the GRACE K-band instrument of 0.2 $\mu m/s$ (Loomis, Nerem, & Luthcke, 2012) is already exceeded. This rough estimate of the change in noise characteristics could also be confirmed by the high-frequency content of the actual AOC values, as seen in Figure 4.10. A special characteristic of the GRACE satellite attitude is a systematic attitude variation with a frequency of about 3.3 mHz related to the control circuit of the magnetic torquers aboard the spacecraft (Bandikova, Flury, & Ko, 2012). As any attitude variations are also reflected in the AOC, a similar pattern is visible there as well. This pattern is significantly accentuated after the pitch bias removal, as can be seen in Figure 4.11. Since the estimation of the stochastic observation model depends on a longer time span of past epochs, this drastic change was

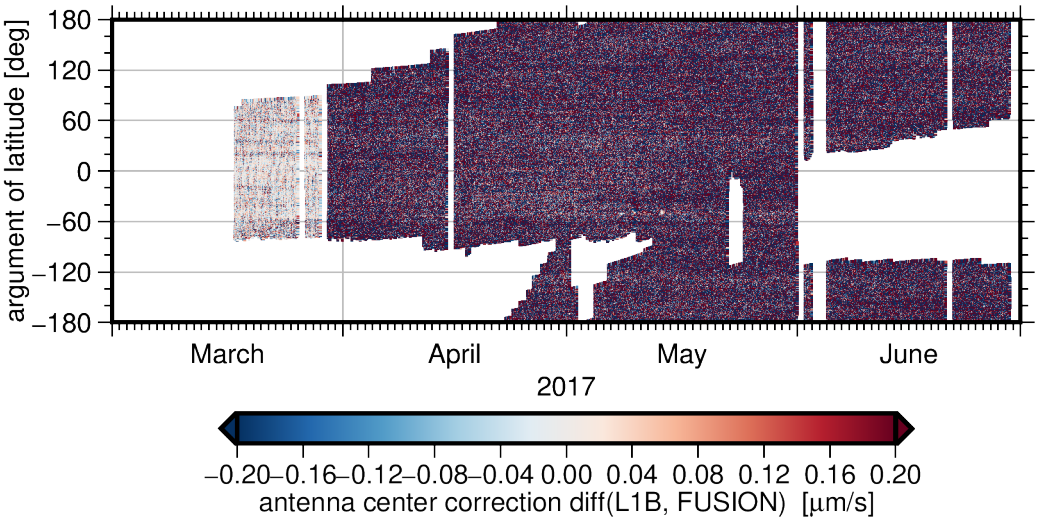

Figure 4.10.: Differences of the original GRACE L1B AOC with respect to the recomputed AOC using smoothed attitude data.

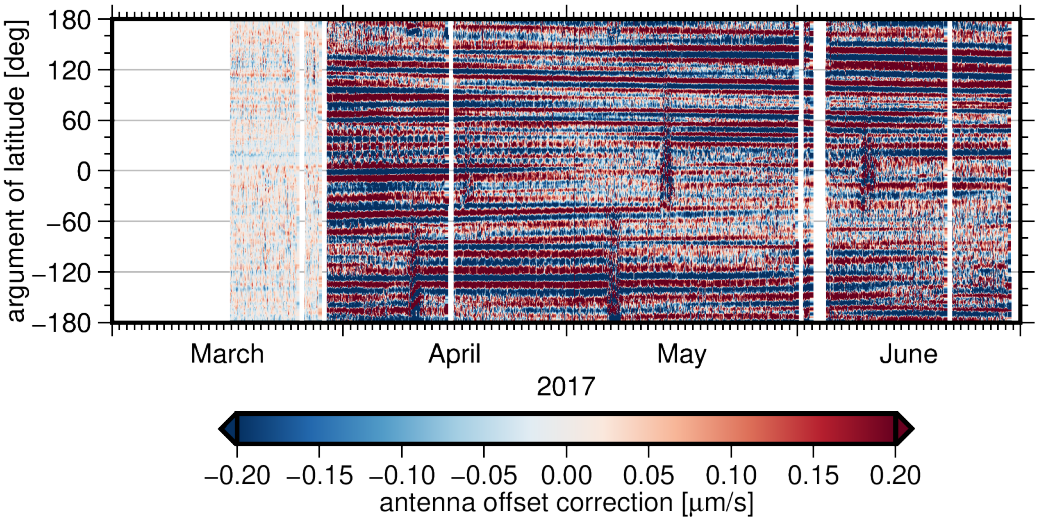

Figure 4.11.: Recomputed range rate AOC based on smoothed attitude data.

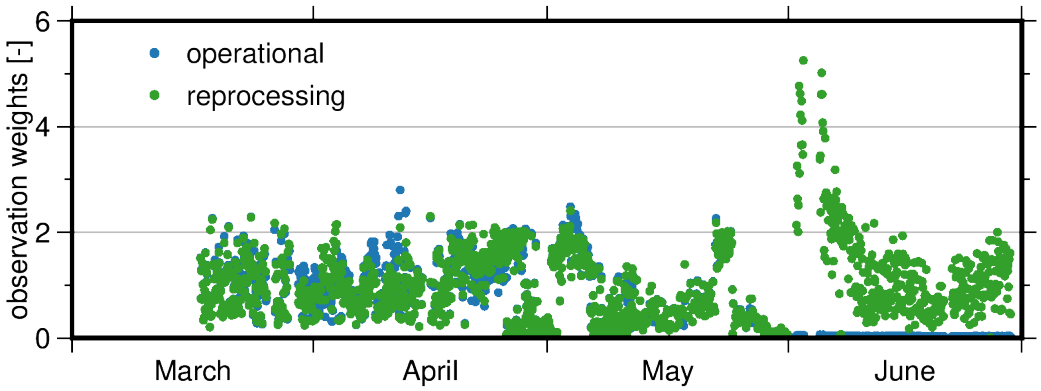

Figure 4.12.: Comparison of operational and reprocessed observation weights.

not immediately picked up in the estimated range-rate covariance function. The peak at $\approx$ 3.3 mHz was first visible in the estimated PSD on April 10, where a re-estimation of the stochastic model using data from April 1 to April 8 was performed. Prior to this date, the stochastic model estimates were dominated by data before March 29, which resulted in a poorly fitting covariance matrix for the observations between March 29 and April 8. In terms of solution quality however, the impact was largely mitigated by the Kalman filter constraints, thus geophysical signal could be reasonably recovered. While there is horizontal striping visible in the difference between predicted and updated state, similar to the artifacts described by Bandikova et al. (2012), the effect is small compared to the overall signal. For the remainder of April, a consistent observation quality was observed, with a single data gap on April 15. With increasing β' angle of the satellites' orbital plane and therefore increased exposure to sunlight, the accelerometer on GRACE-B was reactivated on May 2 and remained active until May 22. For the operational solutions however, it was decided to keep using the accelerometer transplant, as the pitch bias removal revealed that a sudden change in instrument noise behavior requires a certain amount of time to be represented in the stochastic model estimates.

Starting at the beginning of June, a decrease of the GRACE observation weight compared to the predicted state was observed. This resulted in a smaller contribution of the GRACE observations to the update state vector. The reason for this decreased weight possibly lies in a mismatch between the AOC used in the estimation of the stochastic observation model and the normal equation computation following a software configuration change on May 29. For the covariance function estimation, the recomputed AOC based on the smoothed attitude product obtained by the sensor fusion was used, while the determination of the observation weights was based on the original L1B AOC. Since the original L1B AOC exhibits higher noise in the mid- to short-wavelength part of the spectrum (cf. Figure 3.2, the range rate observations were downweighted during VCE. A reprocessing with consistent AOC yielded weights around 1, which is the expected value (cf. Figure 4.12). While using the wrong AOC data meant a degradation of the solution quality, it also showed that the developed approach is sensitive to a mismatch in data quality thus resulting in a robust solution.

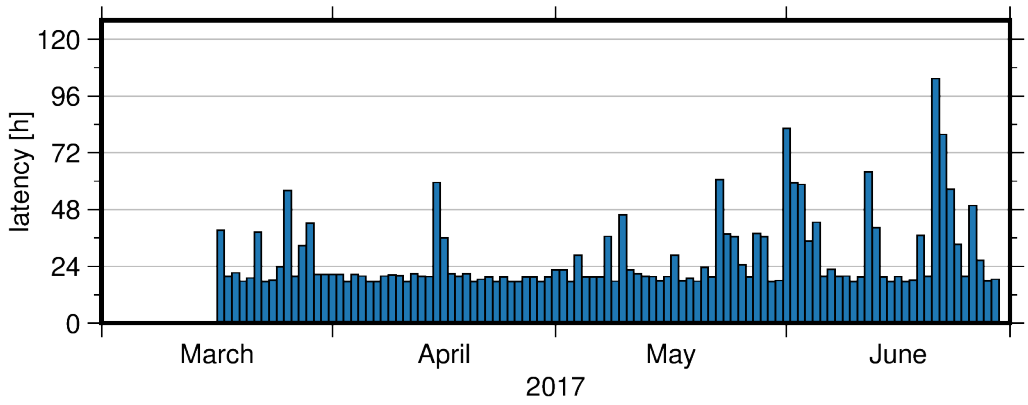

Figure 4.13.: Latency of the computed near real-time solutions from last measured epoch to upload.

4.4. Results and discussion

Throughout the service run, the latency of the gravity field solutions was tracked. Latency in this case was defined as the time span between the last measured epoch and the upload of the gridded solution. The daily latency of the solutions can be seen in Figure 4.13, which highlights that for most days the solution could be uploaded within 20 hours after the last measured epoch, with some periods exceeding two or even three days. These spikes were primarily caused by infrastructure failures, such as server and network outages (May 22, June 1 and June 20). As the employed Kalman filter approach introduces dependencies between consecutive epochs, the latency only gradually decreases after such events. Generally, the processing duration was low enough to fulfill the goal of five-day latency for the derived flood indicators. During the test run only 6 comparatively short data gaps occurred. This meant that over the 3.5 months 93% (98) of all solutions were flagged 'A' (significant GRACE contribution), 7 solutions were flagged 'B' (prediction). Quality category 'C' (no GRACE information in the last 4 days) was never used.

The daily processing schedule remained unaltered throughout the service test run except for a period after the pitch bias removal on March 29. During this period different parameters for the K-band ranging systems such as bias, drift and antenna offset corrections were tested to better account for the increased AOC magnitude and the resulting horizontal striping pattern in the gravity field estimates. Co-estimating antenna offset corrections showed promising results as the non-geophysical features decreased. Previous investigations have however shown that a) the x-component of the AOC is estimated systematically too short (Ellmer, 2018) and b) estimating new AOC values every day, which would be necessary to fit into the Kalman processing scheme, exhibit an extremely large scatter. Due to the large deviation of the estimates from historic values (cf. Chapter 5), it was decided to revert back to the original parametrization in order to preserve the consistency of the time series.

Kinematic orbit quality was very good throughout the operational test run, even though compared to the post-processing solutions, a few trade-offs had to be made. The CODE final clocks feature a densification to a sampling of 5 seconds, while the rapid products

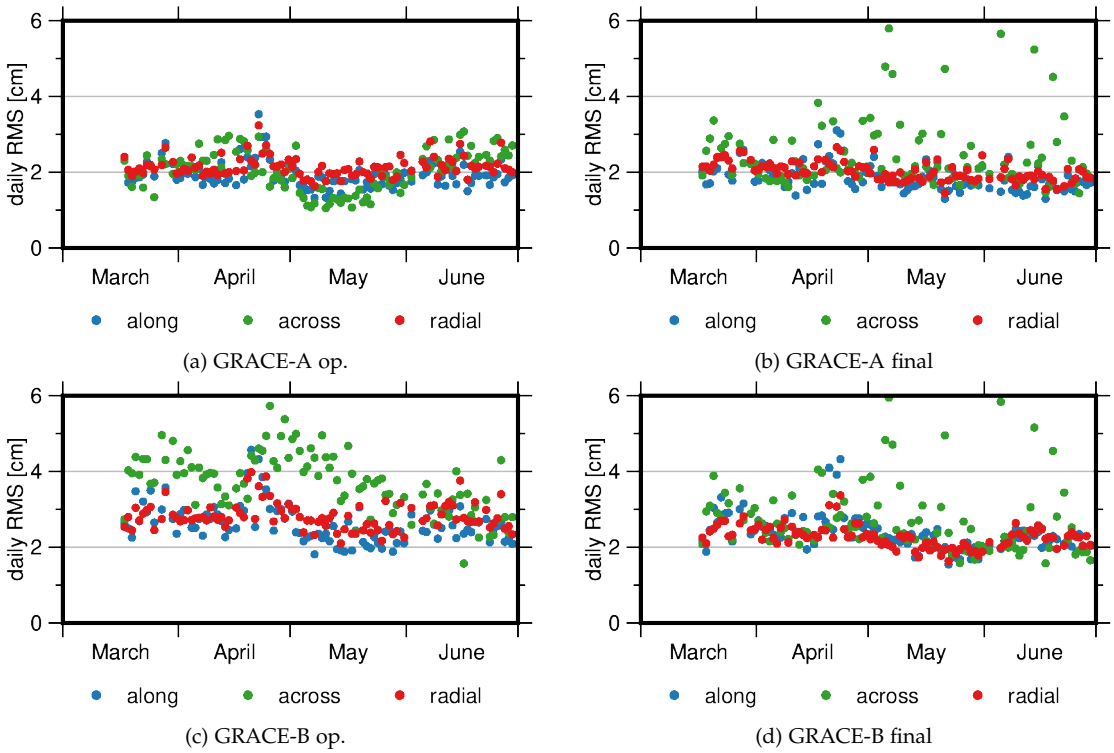

(a) GRACE-A op.

(b) GRACE-A final

(c) GRACE-B op.

(d) GRACE-B final

Figure 4.14.: Daily RMS values of the difference between kinematic orbit positions and a dynamic orbit. Large outliers (>20 cm) were removed and a 15 minute high-pass filter was applied.

only provide a clock estimate every 30 seconds. To avoid the interpolation of clocks, only GNSS receiver observations which coincide with the CODE rapid clocks were used. This effectively limited the sampling to 30 seconds, compared to 10 seconds in the standard L1B processing, where the L1B data rate is the limiting factor. The lower sampling rate has no impact on the gravity field recovery since there, the orbits are decimated to 300 seconds. However, Zehentner (2017) has shown that the sampling rate of the observations has an impact on the orbit quality. It is therefore very interesting to compare the kinematic orbits computed during the operational test run with orbits from a post-processing (final) solution. Figure 4.14 shows daily RMS values of differences between kinematic and dynamic orbit positions for both operational and final orbits. Before the RMS values were computed, epochs which deviate more than 20 cm (3D) from the dynamic orbit were excluded. Furthermore, a high-pass filter with a cutoff frequency of approximately 15 minutes was applied to accentuate the high-frequency noise in the kinematic orbit positions. For the final orbit positions, both satellites behave nearly identical which is consistent with the findings of Zehentner and Mayer-Gürr (2016). The scatter throughout the operational test run period shows little variations except for a few outliers in the cross-track component. In the operational solutions GRACE-A and GRACE-B behave differently. While GRACE-A exhibits a similar noise level in both operational and final solutions, the scatter in the GRACE-B orbits is slightly larger in the operational data set. However, except for the cross-track components in GRACE-B, both operational and final solutions are on the same quality level.

5. Reanalysis of near real-time solutions

After the conclusion of the operational test run, a reanalysis of the GRACE L1B Q/L was conducted. The motivation behind this reprocessing campaign was to gauge how the operational solutions perform compared to a tailored post-processing scheme. The main improvement compared to the operational solutions was expected to be that the varying instrument noise characteristics during the final GRACE mission phase can treated much more rigorously in post-processing. This primarily concerns the removal of the pitch bias on March 29, 2017 which drastically changed the K-band range rate data (see also chapter 4). The stochastic property estimation for the observables relied on comparatively long moving (14 - 30 days) data windows, during which stationarity was assumed. This assumption was definitely violated by the change in pointing angle, leading to a suboptimal covariance function estimate. Next to improved noise estimates, also post-processing algorithms such as the Kalman smoother can be applied to the data which should also increase the robustness of the daily solutions.

5.1. Tailored processing scheme

The reanalysis was conducted using the processing scheme of ITSG-Grace2016 (Ellmer, 2018; Klinger, 2018; Mayer-Gürr et al., 2016). The major difference compared to the operational processing lies in the availability of non-conservative force models for accelerometer pre-calibration (Klinger & Mayer-Gürr, 2016). Further, the knowledge of sudden changes of instrument behavior during the test run period, allows for the rigorous definition of data segments where stationary instrument noise can be assumed. For the time span of the operation test run, from March 17, 2017 to June 29, 2017, 4 segments with similar data characteristics could be identified. The major difference in data quality and availability stem from the pitch bias removal on March 29, 2017 and the activation of the accelerometer on GRACE-B on May 2, 2017. An overview on start and end dates, duration and primary data characteristics can be found in table 5.1. Figure 5.1 shows the estimated error spectra from the operational test run (light colors) compared to single reestimates using all data in the individual segments. Overall, a good agreement between operational and reanalysis can be observed. In segments 2 and 3 (Figures 5.1b and 5.1b), a large amount of energy can be observed in the frequency band around 3.3 mHz. This frequency band is associated with the dominant frequency of the magnetic torquer attitude control (Bandikova et al., 2012). The control circuit of the attitude control maps into the K-band measurements through the antenna offset correction (AOC) as discussed in chapter 4. The difference in this frequency band between operational and reanalyzed data can be explained through the varying parametrization in the course of

Table 5.1.: Segment of similar instrument noise characteristics during the operational NRT service test run.

Start	End	Duration [d]	Description
2017-03-17	2017-03-28	12	Pointing angle ≈ 0 degrees, accelerometer transplant
2017-03-29	2017-05-01	34	Pointing angle ≈ 1 degrees, accelerometer transplant
2017-05-02	2017-05-22	21	Pointing angle ≈ 1 degrees, GRACE-B accelerometer active
2017-05-23	2017-06-29	38	Pointing angle ≈ 1 degrees, accelerometer transplant

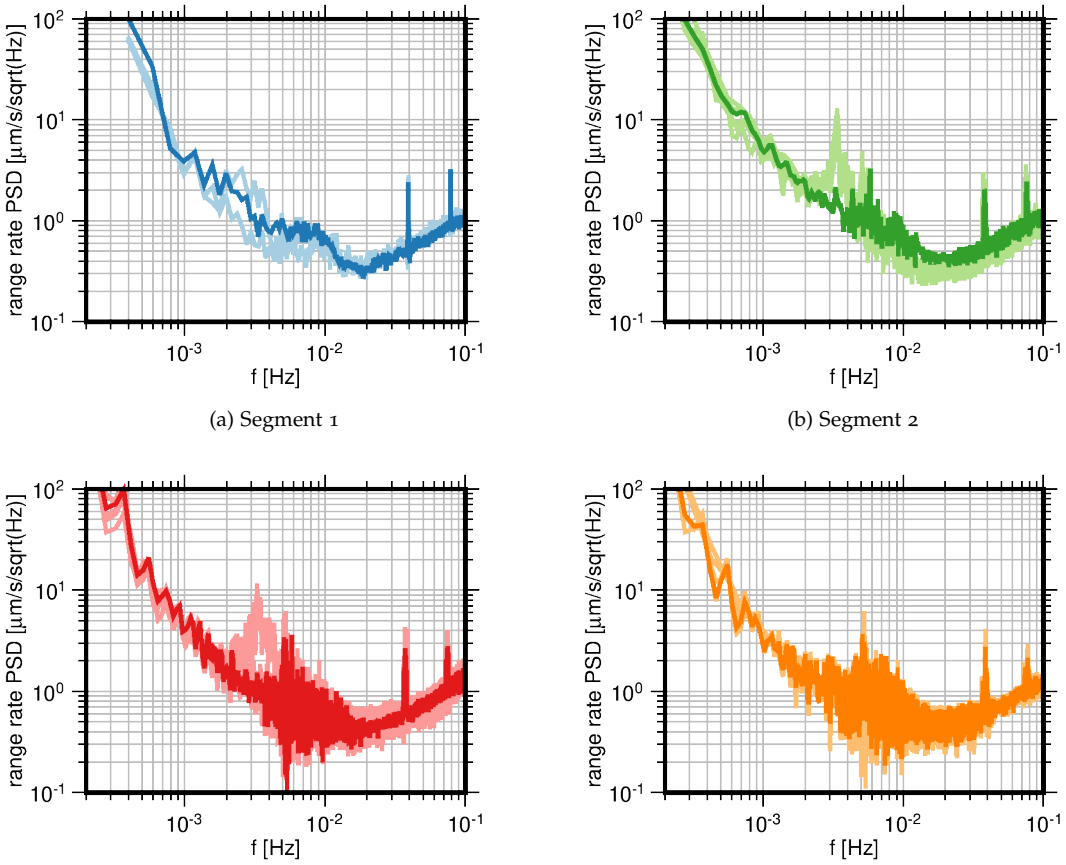

(a) Segment 1

(b) Segment 2

(c) Segment 3

(d) Segment 4

Figure 5.1.: Comparison of operational PSD estimates (light colors) with single re-estimates (dark colors) based on identical input data for each segment.

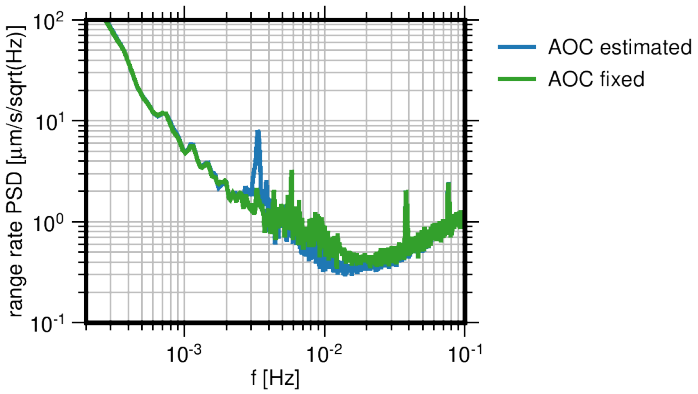

Figure 5.2.: Comparison of range rate PSDs for estimated and fixed antenna offset corrections (AOC).

the operational test run. As already mentioned in Section 4.4, experiments with different K-band parametrizations have been carried out after the pitch bias removal on March 29. In the course of these tests, the position of the K-band antenna center was also co-estimated with the moving-monthly solutions used to derive the stochastic observation model (cf. Chapter 3). There, all three components x, y, z in the satellite reference frame (SRF) of the antenna center were assumed to be unknown and set up as constant biases over the segment-wise monthly solution. The spike in the operational PSDs can be solely explained by these additional parameters. Figure 5.2 shows the range-rate PSD for segment 2, with and without estimated antenna center. As can be seen, estimating the antenna center position induces the aforementioned spike, the energy in the PSD however slightly decreases in the frequency band from 5 mHz to 20 mHz. While this can be seen as an improvement, the estimation of the AOC parameters is problematic. Figure 5.3 shows daily and segment-wise AOC estimates relative to the L1B product for the NRT time series. A large scatter of the estimates compared to historical data can be observed. Throughout the mission duration the estimates of the x- and y-component lie in the range of ± 1 mm with extremely low temporal variability (Kvas, Behzadpour, et al., 2019). This is in stark contrast to the estimates obtained for the period of operational test run, where both the estimates and the scatter are on the centimeter level. Additionally, extremely unrealistic values for the x-component are obtained. This systematically too short AOC estimate is discussed in detail in Ellmer (2018). These findings support the decision to not co-estimate the AOC during the operational service test run. Since the Kalman filter constraint removes a large part of the horizontal striping pattern, this was a reasonable trade-off. Figure 5.4 shows PSD estimates for each segment from data which went through the operational processing chain (light colors) and PSD estimates from reanalyzed data. As can be seen, for segments 1, 2, and 4 a good agreement is found. The large discrepancy in segment 3 can be fully attributed to the use of GRACE-B accelerometer measurement in the reanalysis as opposed to transplant data during the operational test run. These estimated error spectra are the basis of the reanalysis time series which represents the best daily gravity field estimates derived from the given L1B Q/L data. Since these solutions are derived in post-processing, also smoothed state estimates could be derived. Therefore not only forward, but also forward-backward filtered solutions are available. A thorough evaluation of the operational time series, the

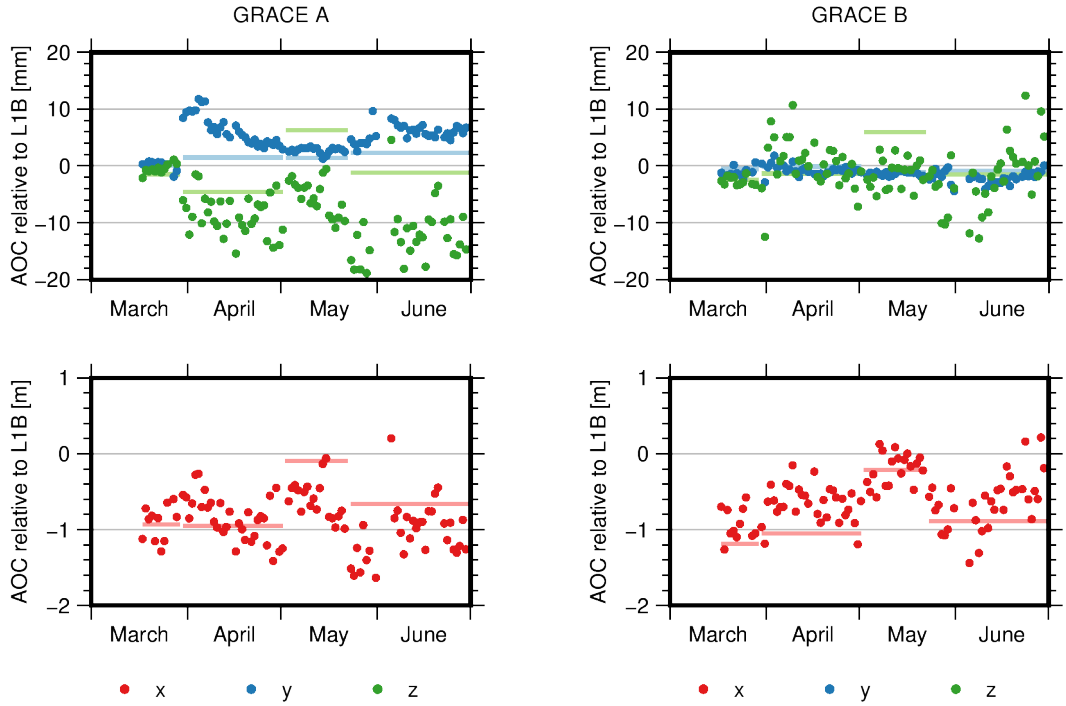

Figure 5.3.: Daily and segment-wise AOC estimates for GRACE A (left panel) and GRACE B (right panel) relative to L1B.

reanalysis, and ITSG-Grace2018 (Kvas, Behzadpour, et al., 2019; Mayer-Gürr et al., 2018), a state of the art daily post-processed solution, will be given in the next section.

5.2. Evaluation of the operational NRT solutions

The purpose of this section is to evaluate how the operational NRT solutions compare to a full post-processing chain. As reference serve the forward sweep of the reanalysis data set and the daily solutions of ITSG-Grace2018 (ITSG2018) which are derived using the least squares adjustment (2.44). For the operational and reanalysis solutions only the forward sweep, that is, the Kalman filter output, is considered. These time series are denoted forward-only (FO). While both the operational test run and the reanalysis are based on the same input data, ITSG-Grace2018 uses the L1B RL03 data set which features improvements in the attitude and K-band processing (JPL, 2018). Some background models and model parameters differ between ITSG-Grace2018 and the other two datasets, such as the definition of the mean pole (e.g., Wahr et al., 2015) and the ocean tide model. Given the setup of this comparison, which focuses on land areas and is based on a rather short time series, these differences play a minor role. Next to the differences in the background models, also conceptual differences within the processing chain, that is, smoothing compared to filtering, exist. As shown in Section 2.3.2, a smoothed solution conserves the phase of the input while the filter introduces a phase shift. Also, the noise level of the filtered and smoothed solutions are likely to differ.

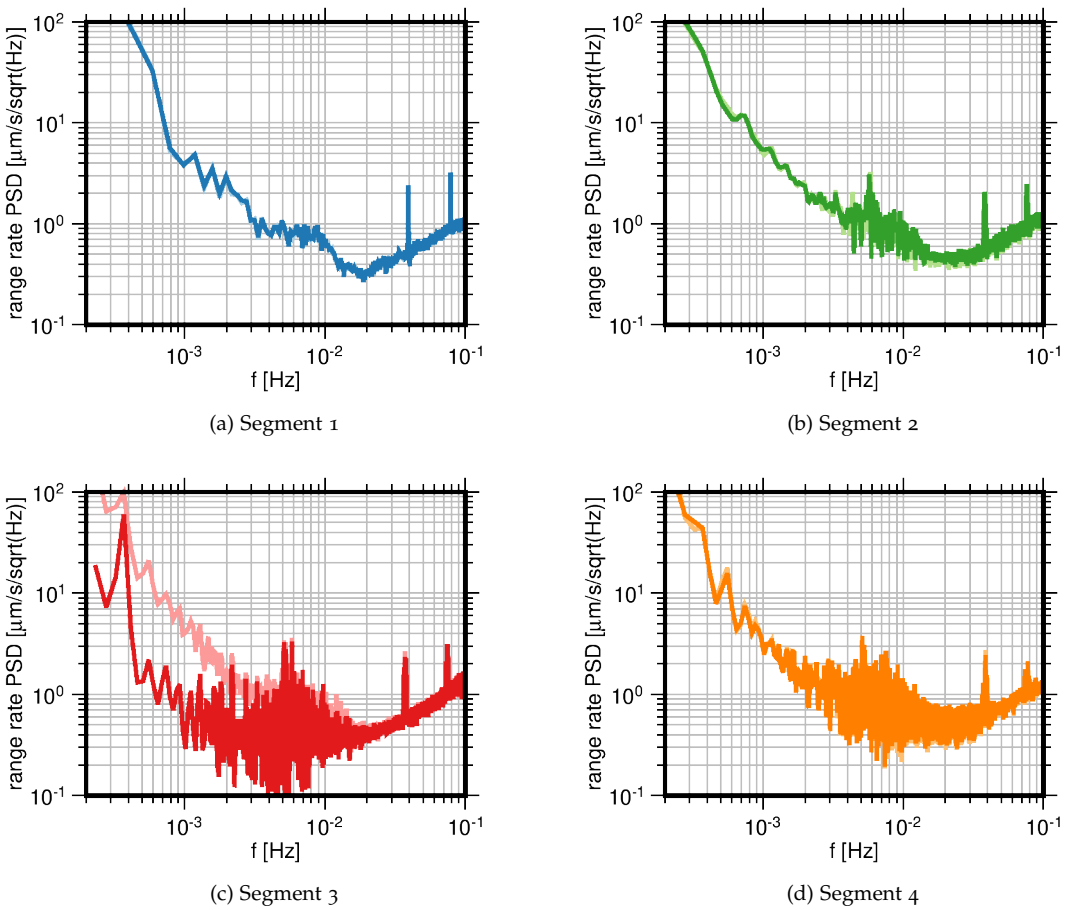

(a) Segment 1

(b) Segment 2

(c) Segment 3

(d) Segment 4

Figure 5.4.: Comparison of PSD estimates (light colors) based on operational pre-processing data with PSD estimates from reanalyzed data.

An initial qualitative comparison of the three time series is conducted by performing principal component analysis (PCA). First, the potential coefficients time series are propagated to space domain to obtain point-wise EWH time series. For reasons elaborated in section 2.4, a Reuter grid was chosen as point distribution. These time series are then interpreted as columns of a matrix which constitutes the input for the PCA. Since PCA is performed independently for each of the three data sets, a few considerations have to be made beforehand. First of all, for each of the data sets a different set of empirical orthogonal functions (EOF) and principal component (PC) time series is obtained. It is expected that these quantities will not differ too much since all time series should pick up the same geophysical signals. As the daily gravity field time series are implicitly filtered in space and time, these signals should dominate the solutions. Any deviations or anomalies are therefore expected to arise from processing errors or systematic effects. In Figure 5.5, the first 7 EOFs of the three time series are shown. As can be seen, EOF1 is nearly identical in all three data sets. For the following EOFs, a decrease in similarity can be observed. Operational and reanalysis show a rather good agreement up to EOF5, that is, the spatial patterns in major river basins are similar. Figure 5.6 shows the temporal evolution of the first 10 PCs. A rather good agreement of all solutions can be observed up to PC5, which constitutes 91% of the signal. For higher PCs, the similarity drops, which makes sense as also the corresponding EOFs differ. A striking feature is the sudden jump on May 2 in the reanalysis solution. This is a consequence of the use of the reactivated accelerometer measurement of GRACE-B compared to the transplant data (cf. also Figure 5.4), Due to the increase in measurement accuracy and the subsequent higher relative weight compared to the predicted state, the GRACE innovation results in a comparatively abrupt state change. The warmup phase of the filter during the first days after March 17 is also clearly visible. However, overall a general agreement between all three solutions can be observed. This is confirmed when looking at snapshots from each of the 4 defined segments, as shown in Figure 5.7. There, the spatial patterns on the continents are very consistent, even though different input data and processing chains are applied to the data.

A more quantitative analysis is performed by examining how much signal of the reanalysis and post-processing solution is explained by the operational Kalman filter estimates. This explained variance (EV) is defined as

$$EV = 1 - \frac{\sum_i (y_i - x_i)^2}{\sum_i y_i^2}. \tag{5.1}$$

In (5.1), the sample standard deviation of the difference between the reference time series y_i and the time series to be evaluated x_i is divided by the sample standard deviation of the reference. It is implied that all time series are centered, that is, the mean was estimated and reduced beforehand. For this comparison x_i, the operational time series, is fixed while the reference changes. In order to see the effect of the smoothing process, also the Kalman smoothed (forward-backward, FB) filtered reanalysis solution is considered. Figure 5.8 shows the explained variance of the reanalysis forward only and forward-backward solutions as well as the daily solutions of ITSG-Grace2018. A common feature of all solutions is that areas with low expected signal, for example, the Sahara desert, show zero to negative explained variance. This can be explained by the fact that these

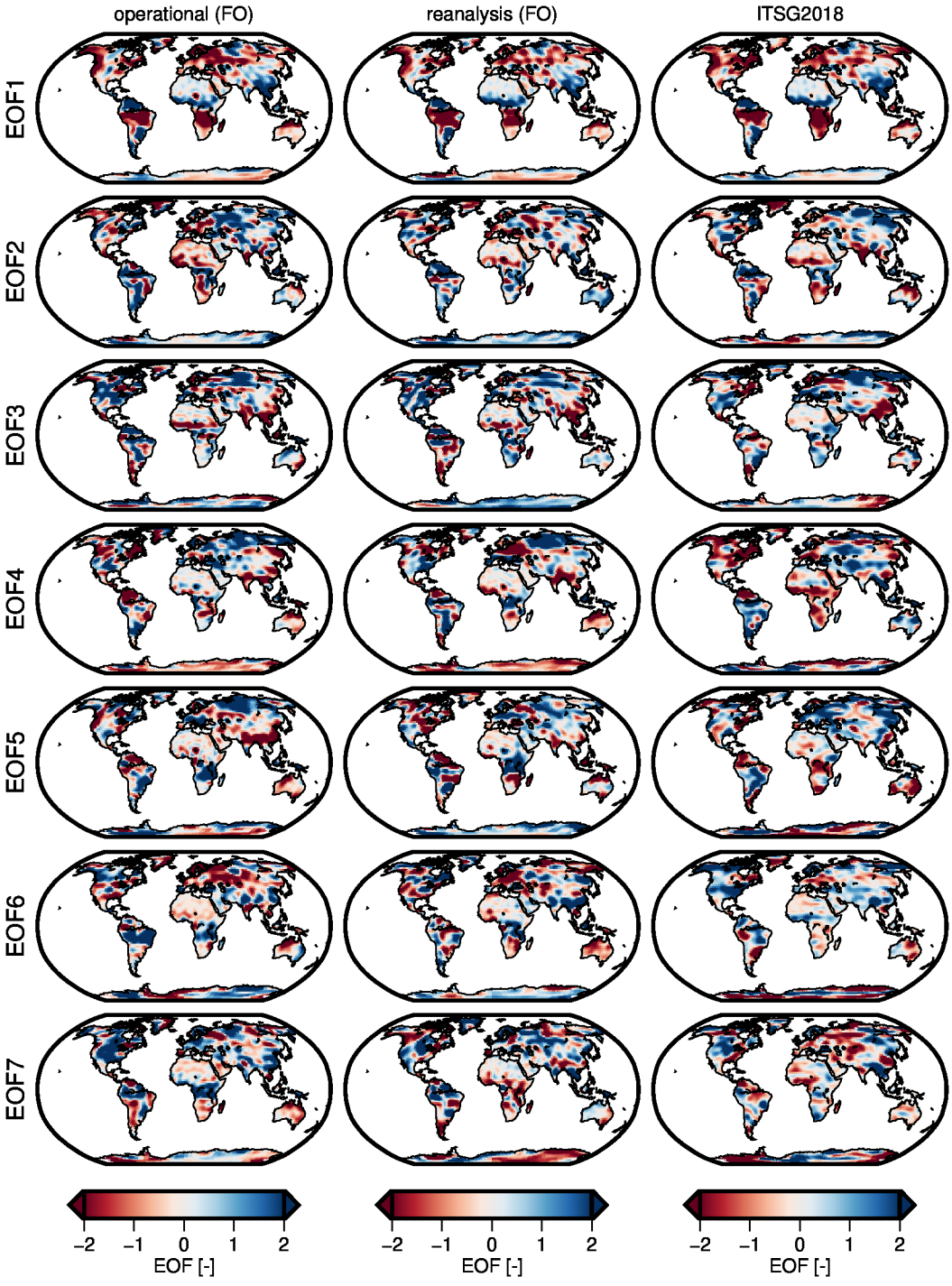

Figure 5.5.: Empirical orthogonal functions of operational, reanalysis, and a post-processing solutions.

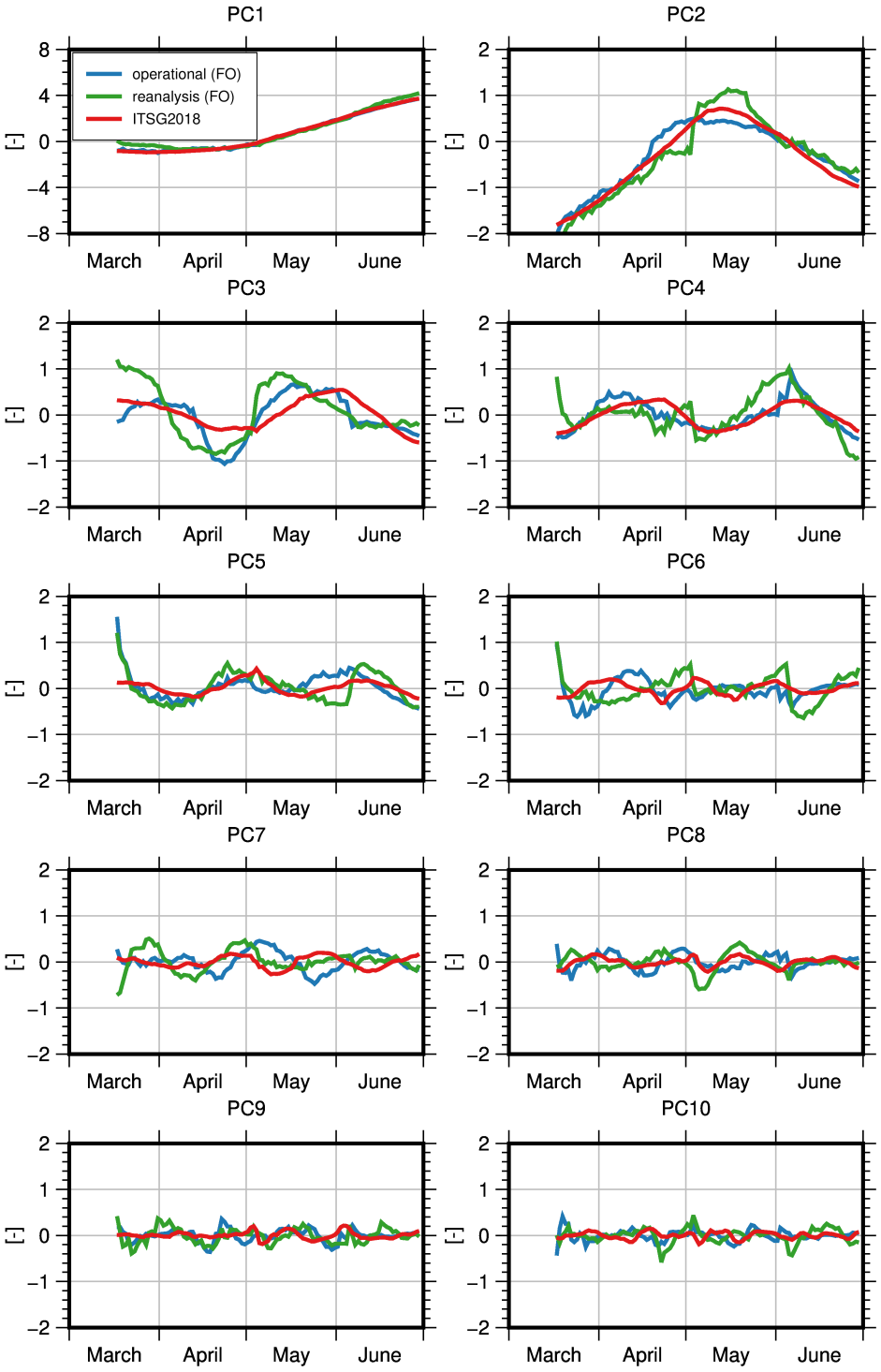

Figure 5.6.: Principal component time series of operational, reanalysis, and a post-processing solutions. Please note the different scale for PC1.

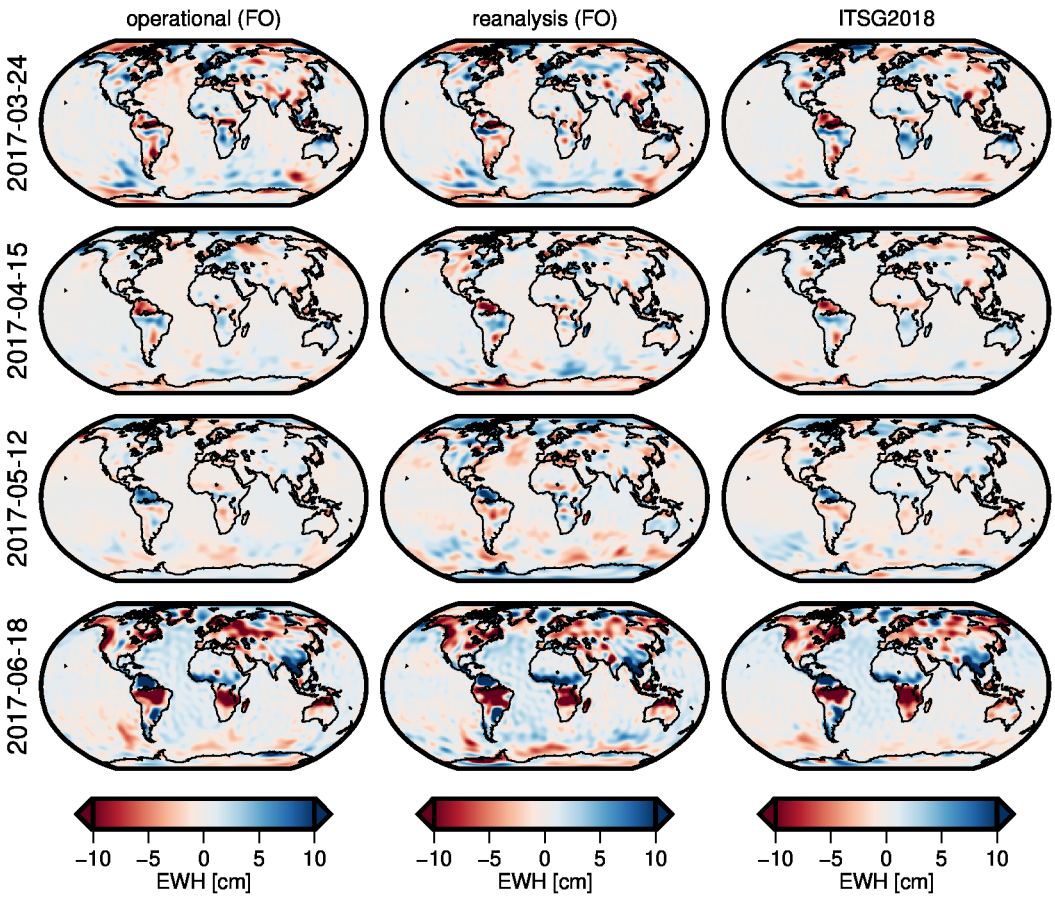

Figure 5.7.: Snapshots of operational, reanalysis, and a post-processing solutions for each segment.

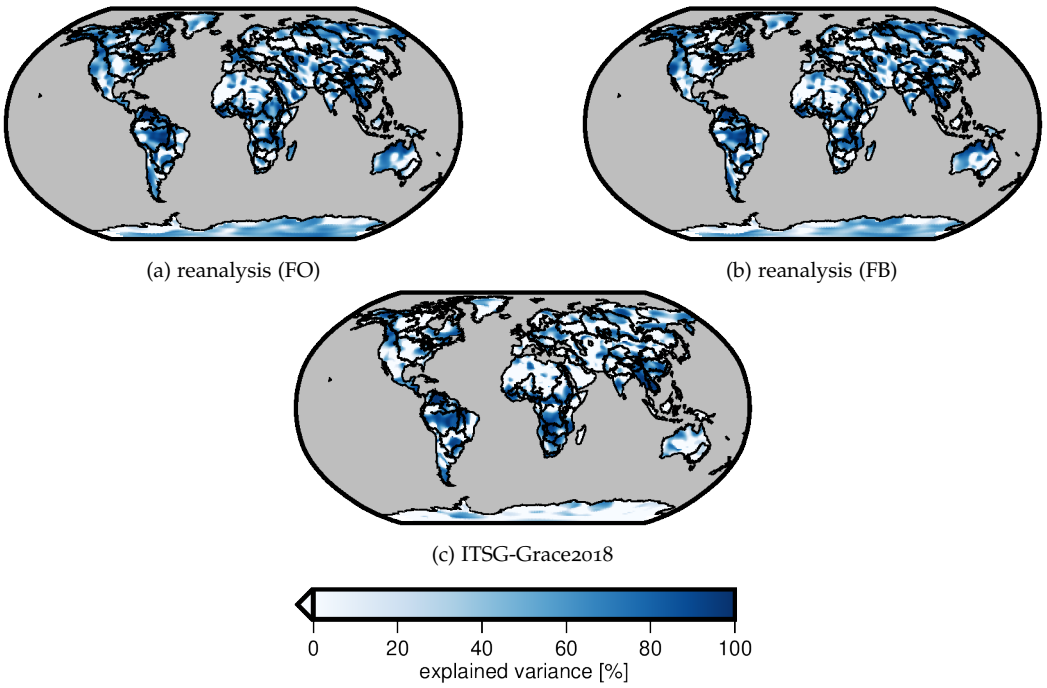

Figure 5.8.: Explained variance of operational (FO) with respect to the reanalysis forward-only and forward-backward solutions and the daily solutions of ITSG-Grace2018.

regions are dominated by observation noise. In regions with strong hydrological signals, for example, Southeast Asia, the Amazon basin or sub-Saharan Africa the solutions tend to agree very well. In Figure 5.9, the distribution of explained variance values of points within major river basins is shown. For all solutions, 80% of all points have a positive explained variance value. The operational time series compares very similar to both reanalysis time series, which was already evident for the spatial depiction in Figure 5.8. It is however surprising that the operational solutions also compare very well to ITSG-Grace2018, since the solutions differ in both the used GRACE observations (L1B RL02 Q/L compared to L1B RL03) as well as in the applied processing scheme.

Overall, both qualitative and quantitative analysis show that the operational solutions

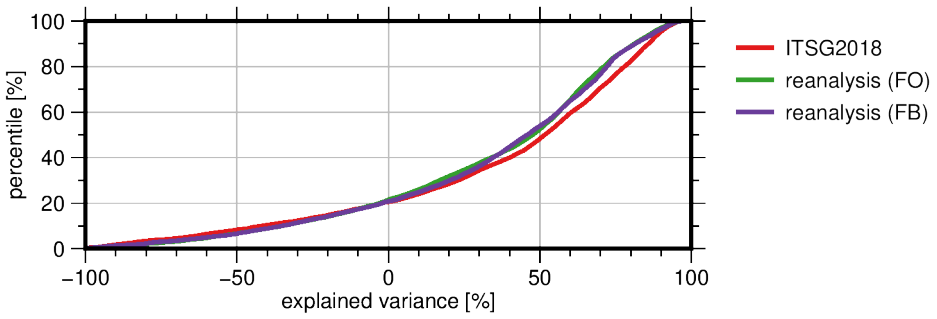

Figure 5.9.: Distribution of explained variance values of points within major river basins.

are comparable not only to the reanalysis but also a highly sophisticated post-processing solution. This implies that the overall solution quality was successfully transferred from post-processing to NRT using the approach presented here.

6. Conclusions and Outlook

In this thesis, a method for the determination of daily gravity field snapshots in near real-time (NRT) was developed. The processing scheme takes the already proven Kalman smoother post-processing approach by Kurtenbach et al. (2012) and transfers the methodology to NRT. This required some major adaptions of key points in the computation chain, due to the different structure of the input data, latency requirements, and lack of information from the future.

The first part of the thesis deals with the generalization of the Kalman smoother approach to vector autoregressive models of arbitrary orders was derived. While an increased model order allows for a better description of the spatio-temporal correlations introduced as process dynamic, vastly more data is required for a stable estimate of the model coefficients. To improve the quality of the derived constraints, geophysically motivated prior information was introduced into the derivation of the used autoregressive models, which led to a substantial improvement of both the stability of the model coefficients and the gravity field solution quality. Furthermore, it was shown that a constrained least squares adjustment can be formulated which yields the same state estimates as the smoothing algorithm. This enables the use of highly efficient and parallelized numerical linear algebra routines.

In the second part of this thesis the already well established Kalman smoother post-processing approach was adapted for near real-time applications. This required some major modifications of key points in the computation chain, due to the different structure of the input data, latency requirements, and lack of information from the future. The processing chain presented in this thesis is based on integrated variational equations, with the gravity field being represented as a series of spherical harmonic coefficients. The observational model makes use of intersatellite range rates and kinematic orbit positions. However, since the input are daily systems of normal equations, other gravity field recovery approaches or observables can be incorporated very easily.

The developed approach was tested using quick-look data from the GRACE mission within the framework of the EGSIEM NRT Service. In the period between March 17 2017 and June 30 2017, 105 daily gravity field solutions were computed in a fully automated manner. A key lesson learned during the operational test run was that the stationarity requirement for the instrument noise over at least a few days has to be critically reviewed for future applications. The operational test run revealed that the method used to estimate the stochastic observation model reacts suboptimally to sudden changes in the data characteristics. While the required stationarity assumption of the process is mostly justified for the majority of the GRACE observation period, the degrading satellite health in the final mission phase proved to be very challenging for the method. To get reliable

instrument noise estimates, a longer time span of measurements has to be accumulated. This is no issue for homogeneous data, however abrupt changes cannot be fully captured. During the operational test run the removal of the pitch bias between the satellites caused such an unforeseen change in data characteristics. The requirement to accumulate a longer batch of data meant that a proper estimate of the sensor error covariance function was only possible after a few days. For the transition period, only a badly fitting noise model was therefore available. Nevertheless, for periods where the stationarity assumption did hold, the operational estimates were nearly identical to tailored post-processing solutions. From an operational perspective, the test run was also a success. Except for a few epochs, a latency of less than 20 hours was achieved. The developed automation software was able to produce daily gravity field estimates autonomously. Furthermore, the implemented measures to ensure traceability, namely version control of the software and its configuration, storing intermediate results, and logging allowed to fully reproduce the time series. This was extremely useful for comparison with a reanalyzed daily gravity field time series, as the cause of occurred anomalies could be identified more easily.

In summary, it was shown that it is feasible to transfer post-processing methods for the determination of daily gravity field solutions to NRT. Despite the harsh conditions during the last months of the GRACE mission, a time series with reasonable quality could be computed. A reanalysis of the input data revealed that the operational solutions could indeed compete with a tailored post-processing scheme. With the launch of GRACE-FO, it will be possible to reactivate operational processing of NRT solutions with all lessons learned during the operational test run. Given the unique feature of satellite gravimetry compared to other remote sensing techniques, that is, the sensitivity to the whole water column including ground water, new complementary information for hydrological applications can be obtained. This in turn allows for a comprehensive monitoring of hydrological extreme events and can potentially contribute to forecasting systems.

Appendix

Appendix A.

Matrix inversion identities

In this chapter matrix identities for the inverse of a sum of matrices are presented. There derivation presented here is based on the LU and UL factorization of a 2x2 block matrix. In Henderson and Searle (1981), a comprehensive review of the origins and applications of the derived identities, as well as alternative derivations can be found.

If the first diagonal block of the 2x2 block matrix is invertible, then the decomposition

$$\begin{bmatrix} \mathbf{A} & \mathbf{B} \\ \mathbf{C} & \mathbf{D} \end{bmatrix} = \begin{bmatrix} \mathbf{I} & \\ \mathbf{L}_{21} & \mathbf{I} \end{bmatrix} \begin{bmatrix} \mathbf{U}_{11} & \mathbf{U}_{12} \\ & \mathbf{U}_{22} \end{bmatrix} = \begin{bmatrix} \mathbf{U}_{11} & \mathbf{U}_{12} \\ \mathbf{L}_{21}\mathbf{U}_{11} & \mathbf{L}_{21}\mathbf{U}_{12} + \mathbf{U}_{22} \end{bmatrix} \tag{A.1}$$

exists (e.g., Higham, 2002). The values of the individual blocks, with $\mathbf{U}_{11} = \mathbf{A}$, $\mathbf{U}_{12} = \mathbf{B}$, $\mathbf{U}_{22} = \mathbf{D} - \mathbf{C}\mathbf{A}^{-1}\mathbf{B}$, and $\mathbf{L}_{21} = \mathbf{C}\mathbf{A}^{-1}$ can then be easily computed. The inverse of (A.1) is given by

$$\begin{bmatrix} \mathbf{A} & \mathbf{B} \\ \mathbf{C} & \mathbf{D} \end{bmatrix}^{-1} = \begin{bmatrix} \mathbf{U}_{11} & \mathbf{U}_{12} \\ & \mathbf{U}_{22} \end{bmatrix}^{-1} \begin{bmatrix} \mathbf{I} & \\ \mathbf{L}_{21} & \mathbf{I} \end{bmatrix}^{-1}. \tag{A.2}$$

To determine the block inverse of the upper triangular matrix the system of equations

$$\begin{bmatrix} \mathbf{U}_{11} & \mathbf{U}_{12} \\ & \mathbf{U}_{22} \end{bmatrix} \begin{bmatrix} \mathbf{X}_{11} & \mathbf{X}_{12} \\ \mathbf{X}_{21} & \mathbf{X}_{22} \end{bmatrix} = \begin{bmatrix} \mathbf{U}_{11}\mathbf{X}_{11} + \mathbf{U}_{12}\mathbf{X}_{21} & \mathbf{U}_{11}\mathbf{X}_{12} + \mathbf{U}_{12}\mathbf{X}_{22} \\ \mathbf{U}_{22}\mathbf{X}_{21} & \mathbf{U}_{22}\mathbf{X}_{22} \end{bmatrix} = \begin{bmatrix} \mathbf{I} & \\ & \mathbf{I} \end{bmatrix} \tag{A.3}$$

can be considered. From there it follows that

$$\begin{bmatrix} \mathbf{U}_{11} & \mathbf{U}_{12} \\ & \mathbf{U}_{22} \end{bmatrix}^{-1} = \begin{bmatrix} \mathbf{U}_{11}^{-1} & -\mathbf{U}_{11}^{-1}\mathbf{U}_{12}\mathbf{U}_{22}^{-1} \\ & \mathbf{U}_{22}^{-1} \end{bmatrix}. \tag{A.4}$$

Equivalently, the inverse of the lower triangular matrix is given by

$$\begin{bmatrix} \mathbf{I} & \\ \mathbf{L}_{21} & \mathbf{I} \end{bmatrix}^{-1} = \begin{bmatrix} \mathbf{I} & \\ -\mathbf{L}_{21} & \mathbf{I} \end{bmatrix}, \tag{A.5}$$

which can be easily verified. Substituting both explicit inverses in (A.2) together with the expressions for the matrix blocks derived from (A.1) leads to

$$\begin{bmatrix} \mathbf{A} & \mathbf{B} \\ \mathbf{C} & \mathbf{D} \end{bmatrix}^{-1} = \begin{bmatrix} \mathbf{A}^{-1} + \mathbf{A}^{-1}\mathbf{B}(\mathbf{D} - \mathbf{C}\mathbf{A}^{-1}\mathbf{B})^{-1}\mathbf{C}\mathbf{A}^{-1} & -\mathbf{A}^{-1}\mathbf{B}(\mathbf{D} - \mathbf{C}\mathbf{A}^{-1}\mathbf{B})^{-1} \\ -(\mathbf{D} - \mathbf{C}\mathbf{A}^{-1}\mathbf{B})^{-1}\mathbf{C}\mathbf{A}^{-1} & (\mathbf{D} - \mathbf{C}\mathbf{A}^{-1}\mathbf{B})^{-1} \end{bmatrix}. \tag{A.6}$$

Similarly to the LU decomposition, a 2x2 block matrix can also be composed into the product of an upper unit triangular matrix and a lower triangular matrix, with

$$\begin{bmatrix} \mathbf{A} & \mathbf{B} \\ \mathbf{C} & \mathbf{D} \end{bmatrix} = \begin{bmatrix} \mathbf{I} & \mathbf{U}_{12} \\ & \mathbf{I} \end{bmatrix} \begin{bmatrix} \mathbf{L}_{11} & \\ \mathbf{L}_{21} & \mathbf{L}_{22} \end{bmatrix} = \begin{bmatrix} \mathbf{L}_{11} + \mathbf{U}_{12}\mathbf{L}_{22} & \mathbf{U}_{12}\mathbf{L}22 \\ \mathbf{L}_{21} & \mathbf{L}_{22} \end{bmatrix}, \tag{A.7}$$

if the last diagonal block $\mathbf{D}$ is invertible. Following the same procedure as for the LU decomposition, the inverse of the block matrix is found with

$$\begin{bmatrix} \mathbf{A} & \mathbf{B} \\ \mathbf{C} & \mathbf{D} \end{bmatrix}^{-1} = \begin{bmatrix} (\mathbf{A} - \mathbf{B}\mathbf{D}^{-1}\mathbf{C})^{-1} & -(\mathbf{A} - \mathbf{B}\mathbf{D}^{-1}\mathbf{C})^{-1}\mathbf{B}\mathbf{D}^{-1} \\ -\mathbf{D}^{-1}\mathbf{C}(\mathbf{A} - \mathbf{B}\mathbf{D}^{-1}\mathbf{C})^{-1} & \mathbf{D}^{-1} + \mathbf{D}^{-1}\mathbf{C}(\mathbf{A} - \mathbf{B}\mathbf{D}^{-1}\mathbf{C})^{-1}\mathbf{B}\mathbf{D}^{-1} \end{bmatrix}. \tag{A.8}$$

By relating (A.6) and (A.8), the two identities

$$(\mathbf{A} - \mathbf{B}\mathbf{D}^{-1}\mathbf{C})^{-1} = \mathbf{A}^{-1} + \mathbf{A}^{-1}\mathbf{B}(\mathbf{D} - \mathbf{C}\mathbf{A}^{-1}\mathbf{B})^{-1}\mathbf{C}\mathbf{A}^{-1} \tag{A.9}$$

and

$$-(\mathbf{A} - \mathbf{B}\mathbf{D}^{-1}\mathbf{C})^{-1}\mathbf{B}\mathbf{D}^{-1} = -\mathbf{A}^{-1}\mathbf{B}(\mathbf{D} - \mathbf{C}\mathbf{A}^{-1}\mathbf{B})^{-1} \tag{A.10}$$

are obtained. Substituting $\mathbf{D} = -\mathbf{E}^{-1}$ yields a cleaner form of (A.9) and (A.10), namely

$$(\mathbf{A} + \mathbf{B}\mathbf{E}\mathbf{C})^{-1} = \mathbf{A}^{-1} - \mathbf{A}^{-1}\mathbf{B}(\mathbf{E}^{-1} + \mathbf{C}\mathbf{A}^{-1}\mathbf{B})^{-1}\mathbf{C}\mathbf{A}^{-1} \tag{A.11}$$

and

$$(\mathbf{A} + \mathbf{B}\mathbf{E}\mathbf{C})^{-1}\mathbf{B}\mathbf{E} = \mathbf{A}^{-1}\mathbf{B}(\mathbf{E}^{-1} + \mathbf{C}\mathbf{A}^{-1}\mathbf{B})^{-1}, \tag{A.12}$$

which is the form derived by Woodbury (1950).

Appendix B.

Inverse of a block banded matrix

This chapter summarizes the findings of Asif and Moura (2005), who developed a computationally efficient inversion algorithm for positive definite, block banded matrices. A key feature of their approach is that the Cholesky factor $\mathbf{W}$ of is used, rather than the original matrix $\mathbf{N} = \mathbf{W}^T\mathbf{W}$. Since the system of normal equations (2.44) will typically be solved using forward and back substitution, $\mathbf{W}$ is already available, thus no additional computations have to be performed. In general, $\mathbf{W}$ will be computed in-place to avoid the use of additional memory. Furthermore, $\mathbf{W}$ shares the same sparsity structure as the upper triangle of $\mathbf{N}$. Thus, there are at most L non-zero superdiagonal blocks with L being the bandwidth of $\mathbf{N}$. The idea behind the algorithm relies on the same principles as the derivation of the matrix identities in the previous chapters. Namely, the matrices are partitioned into blocks and then a recursion scheme is determined. In the following computation scheme, two matrices are involved. The block partitioned Cholesky factor $\mathbf{W}$, with consisting of the blocks $\mathbf{W}_{ij}$, and the covariance matrix of the estimated parameters $\mathbf{\Sigma} = \mathbf{N}^{-1}$ consisting of the blocks $\mathbf{\Sigma}_{i,j}$, with $i, j \in \{1, \ldots, J\}$

The algorithm steps through the matrix backwards, starting with the last block row J. First, the $\min(L, J - i)$ off diagonal blocks of the current row i are updated with

$$\mathbf{\Sigma}_{ij} = -\sum_{k=i+1}^{\min(J,i+L)} (\mathbf{W}_{ii}^{-1}\mathbf{W}_{ik})\mathbf{\Sigma}_{kj}. \tag{B.1}$$

Then, the main diagonal of the matrix is computed through

$$\mathbf{\Sigma}_{ii} = (\mathbf{W}_{ii}^T\mathbf{W}_{ii})^{-1} - \sum_{k=i+1}^{\min(J,i+L)} \mathbf{\Sigma}_{ik}(\mathbf{W}_{ii}^{-1}\mathbf{W}_{ik})^T. \tag{B.2}$$

The recursion is initialized with

$$\mathbf{\Sigma}_{JJ} = (\mathbf{W}_{JJ}^T\mathbf{W}_{JJ})^{-1}. \tag{B.3}$$

References

A, G., Wahr, J., & Zhong, S. (2012, 11). Computations of the viscoelastic response of a 3-D compressible Earth to surface loading: an application to Glacial Isostatic Adjustment in Antarctica and Canada. *Geophysical Journal International*, *192*(2), 557-572. doi: 10.1093/gji/ggs030

Agee, E. M., Cornett, E., & Gleason, K. (2010, jul). An extended solar cycle 23 with deep minimum transition to cycle 24: Assessments and climatic ramifications. *Journal of Climate*, *23*(22), 6110–6114. doi: 10.1175/2010JCLI3831.1

Akaike, H. (1973). Block toeplitz matrix inversion. *SIAM Journal on Applied Mathematics*, *24*(2), 234–241.

Asif, A., & Moura, J. M. F. (2005, Feb). Block matrices with l-block-banded inverse: inversion algorithms. *IEEE Transactions on Signal Processing*, *53*(2), 630-642. doi: 10.1109/TSP.2004.840709

Bandikova, T., Flury, J., & Ko, U.-D. (2012). Characteristics and accuracies of the grace inter-satellite pointing. *Advances in Space Research*, *50*(1), 123 - 135. doi: https://doi.org/10.1016/j.asr.2012.03.011

Bandikova, T., McCullough, C., Kruizinga, G. L., Save, H., & Christophe, B. (2019). Grace accelerometer data transplant. *Advances in Space Research*, *64*(3), 623 - 644. doi: https://doi.org/10.1016/j.asr.2019.05.021

Bartlett, M. S. (1948). Smoothing Periodograms from Time-Series with Continuous Spectra. *Nature*, *161*(4096), 686–687. doi: 10.1038/161686a0

Bartlett, M. S. (1950, 06). PERIODOGRAM ANALYSIS AND CONTINUOUS SPECTRA. *Biometrika*, *37*(1-2), 1-16. doi: 10.1093/biomet/37.1-2.1

Bergmann-Wolf, I., Zhang, L., & Dobslaw, H. (2014). *Global Eustatic Sea-Level Variations for the Approximation of Geocenter Motion from Grace* (Vol. 4) (No. 1). doi: 10.2478/jogs-2014-0006

Bettadpur, S. (2009). *Recommendation for a-priori bias & scale parameters for level-1b acc data (version 2), grace tn-02* (Tech. Rep.). Retrieved from `ftp://isdcftp.gfz-potsdam.de/grace/DOCUMENTS/TECHNICAL_NOTES/TN-02_ACC_Calibration_v2.pdf`

Bettadpur, S. (2018). *Level-2 gravity field product user handbook* (Tech. Rep. No. 4). Austin, Texas: Center for Space Research, University of Texas at Austin.

Beutler, G., & Mervart, L. (2010). *Methods of celestial mechanics. Vol. 1: Physical, mathematical, and numerical principles*. Springer. (OCLC: 838311365)

Bizouard, C., Lambert, S., Gattano, C., Becker, O., & Richard, J.-Y. (2019, May 01). The iers eop 14c04 solution for earth orientation parameters consistent with itrf 2014. *Journal of Geodesy*, *93*(5), 621–633. doi: 10.1007/s00190-018-1186-3

Brockwell, P. J., & Davis, R. A. (2010). *Introduction to time series and forecasting (springer texts in statistics)*. Springer.

Carrère, L., & Lyard, F. (2003). Modeling the barotropic response of the global ocean to atmospheric wind and pressure forcing Comparisons with observations. *Geophysical Research Letters*, *30*(1275), 4. doi: 10.1029/2002GL016473

Carrere, L., Lyard, F., Cancet, M., & Guillot, A. (2015). FES 2014, a new tidal model on the global ocean with enhanced accuracy in shallow seas and in the Arctic region. In *Egu general assembly conference abstracts* (Vol. 17, p. 5481).

Carton, J. A., & Wahr, J. M. (1986, 01). Modelling the pole tide and its effect on the Earth's rotation. *Geophysical Journal International*, *84*(1), 121-137. Retrieved from `https://doi.org/10.1111/j.1365-246X.1986.tb04348.x` doi: 10.1111/j.1365-246X.1986.tb04348.x

Caspary, W., & Wichmann, K. (1994). *Lineare modelle*. R. Oldenburg München.

Chambers, D. P. (2006). Observing seasonal steric sea level variations with GRACE and satellite altimetry. *Journal of Geophysical Research: Oceans*, *111*. doi: 10.1029/2005JC002914

Chen, J. L., Wilson, C. R., & Tapley, B. D. (2010). The 2009 exceptional Amazon flood and interannual terrestrial water storage change observed by GRACE. *Water Resources Research*, *46*(12). doi: 10.1029/2010WR009383

Dach, R., Schaer, S., Arnold, D., Prange, L., Sidorov, D., Stebler, P., ... Jäggi, A. (2018). *CODE final product series for the IGS.* doi: http://dx.doi.org/10.7892/boris.75876.3

Desai, S. D. (2002). Observing the pole tide with satellite altimetry. *Journal of Geophysical Research*, *107*(C11). doi: 10.1029/2001JC001224

Dick, W. R., & Richter, B. (2004). The international earth rotation and reference systems service (iers). In A. Heck (Ed.), *Organizations and strategies in astronomy: Volume 5* (pp. 159–168). Dordrecht: Springer Netherlands. doi: 10.1007/978-1-4020-2571-6_8

Dill, R., & Dobslaw, H. (2013). Numerical simulations of global-scale high-resolution hydrological crustal deformations. *Journal of Geophysical Research: Solid Earth*, *118*(9), 5008-5017. doi: 10.1002/jgrb.50353

Dill, R., Dobslaw, H., & Thomas, M. (2017). Current status of GFZ's operational Earth System model GFZESM. In *Geophysical research abstracts.* Vienna. (Presented at the EGU General Assembly 2017)

Dobslaw, H., Bergmann-Wolf, I., Dill, R., Forootan, E., Klemann, V., Kusche, J., & Sasgen, I. (2015, May). The updated ESA Earth System Model for future gravity mission simulation studies. *Journal of Geodesy*, *89*(5), 505–513. doi: 10.1007/s00190-014-0787-8

Dobslaw, H., Bergmann-Wolf, I., Dill, R., Poropat, L., Thomas, M., Dahle, C., ... Flechtner, F. (2017). A new high-resolution model of non-tidal atmosphere and ocean mass variability for de-aliasing of satellite gravity observations: AOD1B RL06. *Geophysical Journal International*, *211*(1), 263-269. doi: 10.1093/gji/ggx302

Dobslaw, H., Bergmann-Wolf, I., Forootan, E., Dahle, C., Mayer-Gürr, T., Kusche, J., & Flechtner, F. (2016, May 01). Modeling of present-day atmosphere and ocean non-tidal de-aliasing errors for future gravity mission simulations. *Journal of Geodesy*, *90*(5), 423–436. doi: 10.1007/s00190-015-0884-3

Ellmer, M. (2018). *Contributions to GRACE gravity field recovery: Improvements in dynamic orbit integration stochastic modelling of the antenna offset correction, and co-estimation of satellite orientations* (Doctoral dissertation, Graz University of Technology). doi: 10.3217/978-3-85125-646-8

Fan, J., Liao, Y., & Liu, H. (2016). An overview of the estimation of large covariance and precision matrices. *The Econometrics Journal*, *19*(1), C1–C32. doi: 10.1111/ectj.12061

Flechtner, F., Bettadpur, S., Kruizinga, G., Dahle, C., & Tapley, B. (2016a, 11). *GRACE Science Data System Monthly Report March 2017* (Tech. Rep.). GRACE Science Data System. Retrieved from ftp://isdcftp.gfz-potsdam.de/grace/DOCUMENTS/NEWSLETTER/2017/GRACE_SDS_NL_1611.pdf

Flechtner, F., Bettadpur, S., Kruizinga, G., Dahle, C., & Tapley, B. (2016b, 9). *GRACE Science Data System Monthly Report March 2017* (Tech. Rep.). GRACE Science Data System. Retrieved from ftp://isdcftp.gfz-potsdam.de/grace/DOCUMENTS/NEWSLETTER/2017/GRACE_SDS_NL_1609.pdf

Flechtner, F., Bettadpur, S., Kruizinga, G., Dahle, C., & Tapley, B. (2017, 3). *GRACE Science Data System Monthly Report March 2017* (Tech. Rep.). GRACE Science Data System. Retrieved from ftp://isdcftp.gfz-potsdam.de/grace/DOCUMENTS/NEWSLETTER/2017/GRACE_SDS_NL_1703.pdf

Flury, J., Bettadpur, S., & Tapley, B. D. (2008). Precise accelerometry onboard the GRACE gravity field satellite mission. *Advances in Space Research*, *42*(8), 1414–1423. doi: https://doi.org/10.1016/j.asr.2008.05.004

Folkner, W., Williams, J., Boggs, D., Park, R., & Kuchynka, P. (2009). *The Planetary and Lunar Ephemeris DE421* (The Interplanetary Network Progress Report No. 42-178). Jet Propulsion Laboratory, Pasadena, California. Retrieved from http://ipnpr.jpl.nasa.gov/progress_report/42-178/178C.pdf

Frommknecht, B., Fackler, U., & Flury, J. (2006). Integrated Sensor Analysis GRACE. In J. Flury, R. Rummel, C. Reigber, M. Rothacher, G. Boedecker, & U. Schreiber (Eds.), *Observation of the earth system from space* (pp. 99–113). Berlin, Heidelberg: Springer Berlin Heidelberg. doi: 10.1007/3-540-29522-4_8

Gelb, A. (1974). *Applied optimal estimation. written by technical staff, the analytic sciences corporation. edited by arthur gelb, etc* -. Massachusetts: M.I.T. Press.

Golub, G. H., & Loan, C. F. V. (1996). *Matrix computations (3rd ed.)*. Johns Hopkins University Press.

Gouweleeuw, B., Kvas, A., Gruber, C., Gain, A., Mayer-Gürr, T., Flechtner, F., & Güntner, A. (2018, 5 9). Daily grace gravity field solutions track major flood events in the ganges–brahmaputra delta. *Hydrology and Earth System Sciences*, *22*, 2867–2880. doi: 10.5194/hess-22-2867-2018

Gruber, C., & Gouweleeuw, B. (2019, 01). Short-latency monitoring of continental, ocean- and atmospheric mass variations using GRACE intersatellite accelerations. *Geophysical Journal International*, *217*(1), 714-728. doi: 10.1093/gji/ggz042

Han, S. C., Jekeli, C., & Shum, C. K. (2004). Time-variable aliasing effects of ocean tides, atmosphere, and continental water mass on monthly mean GRACE gravity field. *Journal of Geophysical Research: Solid Earth*, *109*(4). doi: 10.1029/2003JB002501

Heiskanen, W., & Moritz, H. (1967). *Physical geodesy*. W. H. Freeman.

Henderson, H. V., & Searle, S. R. (1981). On deriving the inverse of a sum of matrices. *SIAM Review*, *23*(1), 53–60.

Higham, N. J. (2002). *Accuracy and stability of numerical algorithms*. SIAM: Society for Industrial and Applied Mathematics.

Horwath, M., Lemoine, J. M., Biancale, R., & Bourgogne, S. (2011). Improved GRACE science results after adjustment of geometric biases in the Level-1B K-band ranging

data. *Journal of Geodesy*, *85*(1), 23–38. doi: 10.1007/s00190-010-0414-2

Huber, P. J., & Ronchetti, E. M. (2009). *Robust statistics* (2nd ed.). P John Wiley & Sons.

Igs quality of service fact sheet (Tech. Rep.). (2013). Pasadena, California: International GNSS Service (IGS).

Inácio, P., Ditmar, P., Klees, R., & Farahani, H. H. (2015, jun). Analysis of star camera errors in GRACE data and their impact on monthly gravity field models. *Journal of Geodesy*, *89*(6), 551–571. doi: 10.1007/s00190-015-0797-1

Jackson, D. D. (1972). Interpretation of inaccurate, insufficient and inconsistent data. *Geophysical Journal of the Royal Astronomical Society*, *28*(2), 97-109. doi: 10.1111/j.1365-246X.1972.tb06115.x

JPL. (2018). *GRACE LEVEL 1B JPL RELEASE 3.0*. PO.DAAC. CA, USA. doi: http://dx.doi.org/10.5067/GRJPL-L1B03

Jäggi, A., Weigelt, M., Flechtner, F., Güntner, A., Mayer-Gürr, T., Martinis, S., ... Shabanloui, A. (2019, 05). European Gravity Service for Improved Emergency Management (EGSIEM)—from concept to implementation. *Geophysical Journal International*, *218*(3), 1572-1590. doi: 10.1093/gji/ggz238

Kalman, R. E. (1960). A new approach to linear filtering and prediction problems. *Transactions of the ASME–Journal of Basic Engineering*, *82*(Series D), 35–45.

Klinger, B. (2018). *A contribution to GRACE time-variable gravity field recovery: Improved Level-1B data pre-processing methodologies* (Dissertation). Graz University of Technology.

Klinger, B., & Mayer-Gürr, T. (2016). The role of accelerometer data calibration within GRACE gravity field recovery: Results from ITSG-Grace2016. *Advances in Space Research*, *58*(9), 1597-1609. doi: 10.1016/j.asr.2016.08.007

Koch, K.-R. (2004). *Parameterschätzung und hypothesentests in linearen modellen*. Retrieved from `http://www.geod.uni-bonn.de`

Koch, K.-R., & Kusche, J. (2002, may). Regularization of geopotential determination from satellite data by variance components. *Journal of Geodesy*, *76*(5), 259–268. doi: 10.1007/s00190-002-0245-x

Kurtenbach, E. (2011). *Entwicklung eines kalman-filters zur bestimmung kurzzeitiger variationen des erdschwerefeldes aus daten der satellitenmission GRACE* (Dissertation). Retrieved from `http://nbn-resolving.de/urn:nbn:de:hbz:5N-25739`

Kurtenbach, E., Eicker, A., Mayer-Gürr, T., Holschneider, M., Hayn, M., Fuhrmann, M., & Kusche, J. (2012). Improved daily GRACE gravity field solutions using a Kalman smoother. *Journal of Geodynamics*, *59-60*, 39–48. doi: https://doi.org/10.1016/j.jog.2012.02.006

Kurtenbach, E., Mayer-Gürr, T., & Eicker, A. (2009). Deriving daily snapshots of the Earth's gravity field from GRACE LIB data using Kalman filtering. *Geophysical Research Letters*, *36*(17). doi: 10.1029/2009GL039564

Kvas, A., Behzadpour, S., Ellmer, M., Klinger, B., Strasser, S., Zehentner, N., & Mayer-Gürr, T. (2019). Itsg-grace2018: Overview and evaluation of a new grace-only gravity field time series. *Journal of Geophysical Research: Solid Earth*. doi: 10.1029/2019JB017415

Kvas, A., Brockmann, J. M., Krauss, S., Gruber, T., Schubert, T., Meyer, U., ... Pail, R. (2019). The combined satellite-only gravity field model GOCO06s (in preparation). *Journal of Geodesy*.

Loomis, B. D., Nerem, R. S., & Luthcke, S. B. (2012, may). Simulation study of a follow-on gravity mission to GRACE. *Journal of Geodesy*, *86*(5), 319–335. doi:

10.1007/s00190-011-0521-8

Lütkepohl, H. (2005). *New introduction to multiple time series analysis* (Vol. 1). doi: 10.1007/978-3-540-27752-1

Mayer-Gürr, T. (2006). *Gravitationsfeldbestimmung aus der analyse kurzer bahnbögen am beispiel der satellitenmissionen CHAMP und GRACE* (Dissertation). Retrieved from `https://www.igg.uni-bonn.de/de/publikationen/bestand-nach-standorten/sr-09-mayer-gurr.pdf`

Mayer-Gürr, T., Behzadpour, S., Ellmer, M., Kvas, A., Klinger, B., & Zehentner, N. (2016). *ITSG-Grace2016 - Monthly and Daily Gravity Field Solutions from GRACE.* (Dataset) doi: 10.5880/icgem.2016.007

Mayer-Gürr, T., Behzadpur, S., Ellmer, M., Kvas, A., Klinger, B., Strasser, S., & Zehentner, N. (2018). *ITSG-Grace2018 - Monthly and Daily Gravity Field Solutions from GRACE.* (Dataset) doi: 10.5880/icgem.2018.003

Mayer-Gürr, T., & GOCO Team. (2015). *The combined satellite gravity field model GOCO05s.* Vienna. (Presented at the EGU General Assembly 2015, Abstract EGU2015-12364)

Mayer-Gürr, T., Kurtenbach, E., & Eicker, A. (2010, 5 5). ITG-Grace2010: the new GRACE gravity field release computed in Bonn.. (EGU General Assembly 2012 ; Conference date: 23-04-2012 Through 27-04-2012)

Mayer-Gürr, T., Zehentner, N., Klinger, B., & Kvas, A. (2014, 9 29). ITSG-Grace2014: a new GRACE gravity field release computed in Graz.. (GRACE Science Team Meeting 2014 ; Conference date: 29-09-2014 Through 01-10-2014)

Meyer, U., Jäggi, A., & Beutler, G. (2012). The Impact of Attitude Control on GRACE Accelerometry and Orbits. In S. Kenyon, M. C. Pacino, & U. Marti (Eds.), *Geodesy for planet earth* (pp. 139–146). Berlin, Heidelberg: Springer Berlin Heidelberg.

Meyer, U., Jäggi, A., Jean, Y., & Beutler, G. (2016). AIUB-RL02: an improved time-series of monthly gravity fields from GRACE data. *Geophysical Journal International*, *205*(2), 1196–1207. doi: 10.1093/gji/ggw081

Montenbruck, O., & Gill, E. (2000). *Satellite Orbits*. Springer-Verlag Berlin Heidelberg New York.

Montenbruck, O., Hauschild, A., & Steigenberger, P. (2014). Differential code bias estimation using multi-gnss observations and global ionosphere maps. *Navigation*, *61*(3), 191-201. doi: 10.1002/navi.64

Neumaier, A., & Schneider, T. (2001, March). Estimation of parameters and eigenmodes of multivariate autoregressive models. *ACM Trans. Math. Softw.*, *27*(1), 27–57. doi: 10.1145/382043.382304

Panet, I., Bonvalot, S., Narteau, C., Remy, D., & Lemoine, J.-M. (2018). Migrating pattern of deformation prior to the Tohoku-Oki earthquake revealed by GRACE data. *Nature Geoscience*, *11*(5), 367–373. doi: 10.1038/s41561-018-0099-3

Pearson, K. (1901). LIII. On lines and planes of closest fit to systems of points in space. *The London, Edinburgh, and Dublin Philosophical Magazine and Journal of Science*, *2*(11), 559–572. doi: 10.1080/14786440109462720

Peterseim, N. (2014). *Twangs – high-frequency disturbing signals in the 10 hz accelerometer data of the grace satellites* (Dissertation). Technical University Munich, Munich.

Petit, G., & Luzum, B. (Eds.). (2010). *IERS Conventions (2010)*. Frankfurt am Main: Verlag des Bundesamts für Kartographie und Geodäsie.

Pisarenko, V. F. (1973). The Retrieval of Harmonics from a Covariance Func-

tion. *Geophysical Journal of the Royal Astronomical Society*, *33*(3), 347–366. doi: 10.1111/j.1365-246X.1973.tb03424.x

Rao, K. R., & Yip, P. (Eds.). (2000). *The transform and data compression handbook*. Boca Raton, FL, USA: CRC Press, Inc.

Rauch, H. E., Striebel, C. T., & Tung, F. (1965, aug). Maximum likelihood estimates of linear dynamic systems. *AIAA Journal*, *3*(8), 1445–1450. doi: 10.2514/3.3166

Reuter, R. (1982). *Über integralformeln der einheitssphäre und harmonische splinefunktionen* (Dissertation). RWTH Aachen.

Rietbroek, R., Brunnabend, S.-E., Dahle, C., Kusche, J., Flechtner, F., Schröter, J., & Timmermann, R. (2009). Changes in total ocean mass derived from GRACE, GPS, and ocean modeling with weekly resolution. *Journal of Geophysical Research: Oceans*, *114*(C11). doi: 10.1029/2009JC005449

Roman, S. (2007). *Advanced linear algebra (graduate texts in mathematics, vol. 135)*. Springer.

Sakumura, C., Bettadpur, S., Save, H., & McCullough, C. (2016). High-frequency terrestrial water storage signal capture via a regularized sliding window mascon product from GRACE. *Journal of Geophysical Research: Solid Earth*, *121*(5), 4014–4030. doi: 10.1002/2016JB012843

Saltzmann, M. (1993). *Least squares filtering and testing for geodetic navigation applications*. Retrieved from `http://resolver.tudelft.nl/uuid:f2e6e431-3ba4-4073-9f04-54340459873f`

Savcenko, R., & Bosch, W. (2012). *EOT11A - Empirical Ocean Tide Model from Multi-Mission Satellite Altimetry*. Retrieved from `https://doi.org/10.1594/PANGAEA.834232`. (Deutsches Geodätisches Forschungsinstitut (DGFI), München)

Save, H. V., Bettadpur, S. V., & Tapley, B. D. (2006, December). Single Accelerometer Gravity Solutions for GRACE. *AGU Fall Meeting Abstracts*, G13A-0026.

Schmid, R., Steigenberger, P., Gendt, G., Ge, M., & Rothacher, M. (2007, Dec 01). Generation of a consistent absolute phase-center correction model for gps receiver and satellite antennas. *Journal of Geodesy*, *81*(12), 781–798. doi: 10.1007/s00190-007-0148-y

Seidelmann, P. K. (1982, May). 1980 IAU theory of nutation: The final report of the IAU working group on nutation. *Celestial Mechanics*, *27*(1), 79–106. doi: 10.1007/bf01228952

Simon, D. (2006). *Optimal state estimation: Kalman, h infinity, and nonlinear approaches*. Wiley-Interscience.

Stoica, P., & Moses, R. L. (2005). *Introduction to spectral analysis*. Prentice Hall, Upper Saddle River, New Jersey.

Sun, Y., Ditmar, P., & Riva, R. (2016). Observed changes in the Earth's dynamic oblateness from GRACE data and geophysical models. *Journal of Geodesy*, *90*(1), 81–89. doi: 10.1007/s00190-015-0852-y

Swenson, S., Chambers, D., & Wahr, J. (2008). Estimating geocenter variations from a combination of GRACE and ocean model output. *Journal of Geophysical Research: Solid Earth*, *113*(8), 1–12. doi: 10.1029/2007JB005338

Tapley, B. D., Bettadpur, S., Watkins, M., & Reigber, C. (2004). The gravity recovery and climate experiment: Mission overview and early results. *Geophysical Research Letters*, *31*(9). doi: 10.1029/2004GL019920

Tapley, B. D., Flechtner, F., Watkins, M., & Bettadpur, S. (2015). *GRACE Mission: Status and Prospects*. Retrieved from `http://www2.csr.utexas.edu/grace/GSTM/2017/`

proceedings.html (Presented at the GRACE Science Team Meeting 2015)

Teunissen, P. J., & Montenbruck, O. (Eds.). (2017). *Springer handbook of global navigation satellite systems*. Springer International Publishing. doi: 10.1007/978-3-319-42928-1

Touboul, P., Foulon, B., Rodrigues, M., & Marque, J. P. (2004). In orbit nano-g measurements, lessons for future space missions. *Aerospace Science and Technology*, *8*(5), 431–441. doi: https://doi.org/10.1016/j.ast.2004.01.006

van Dam, T., & Ray, R. D. (2010). *S1 and S2 Atmospheric Tide Loading Effects for Geodetic Applications.* Retrieved from http://geophy.uni.lu/ggfc-atmosphere/tide-loading-calculator.html

Velicogna, I. (2009). Increasing rates of ice mass loss from the Greenland and Antarctic ice sheets revealed by GRACE. *Geophysical Research Letters*, *36*(19). doi: 10.1029/2009GL040222

Verhaegen, M., & Van Dooren, P. (1986, October). Numerical aspects of different kalman filter implementations. *IEEE Transactions on Automatic Control*, *31*(10), 907-917. doi: 10.1109/TAC.1986.1104128

Wahr, J., Molenaar, M., & Bryan, F. (1998). Time variability of the Earth's gravity field: Hydrological and oceanic effects and their possible detection using GRACE. *Journal of Geophysical Research: Solid Earth*, *103*(B12), 30205–30229. doi: 10.1029/98JB02844

Wahr, J., Nerem, R. S., & Bettadpur, S. V. (2015). The pole tide and its effect on GRACE time-variable gravity measurements: Implications for estimates of surface mass variations. *Journal of Geophysical Research: Solid Earth*, *120*(6), 4597–4615. doi: 10.1002/2015JB011986

Wei, W. W. (2006). *Time series analysis* (2nd ed.). Addison-Wesley.

Weigelt, M., Sneeuw, N., Schrama, E. J., & Visser, P. N. (2013). An improved sampling rule for mapping geopotential functions of a planet from a near polar orbit. *Journal of Geodesy*, *87*(2), 127–142. doi: 10.1007/s00190-012-0585-0

Welch, P. (1967, June). The use of fast fourier transform for the estimation of power spectra: A method based on time averaging over short, modified periodograms. *IEEE Transactions on Audio and Electroacoustics*, *15*(2), 70-73. doi: 10.1109/TAU.1967.1161901

Woodbury, M. A. (1950). *Inverting modified matrices* (P. University, Ed.). Princeton, NJ: Department of Statistics, Princeton University.

Wouters, B., Gardner, A. S., & Moholdt, G. (2019). Global Glacier Mass Loss During the GRACE Satellite Mission (2002-2016). *Frontiers in Earth Science*, *7*, 96. doi: 10.3389/feart.2019.00096

Zehentner, N. (2017). *Kinematic orbit positioning applying the raw observation approach to observe time variable gravity* (Dissertation). Graz University of Technology.

Zehentner, N., & Mayer-Gürr, T. (2016). Precise orbit determination based on raw GPS measurements. *Journal of Geodesy*, *90*(3), 275–286. doi: 10.1007/s00190-015-0872-7

Zenner, L., Bergmann-Wolf, I., Dobslaw, H., Gruber, T., Güntner, A., Wattenbach, M., ... Dill, R. (2014, nov). Comparison of Daily GRACE Gravity Field and Numerical Water Storage Models for De-aliasing of Satellite Gravimetry Observations. *Surveys in Geophysics*, *35*(6), 1251–1266. doi: 10.1007/s10712-014-9295-x

Acronyms

AC analysis center.
ACC accelerometer.
ACV antenna center variations.
ANTEX Antenna Exchange Format.
AOC antenna offset correction.
ASCII American Standard Code for Information Interchange.

CHAMP Challenging Minisatellite Payload.
CODE Center for Orbit Determination in Europe.
CSR Center of Space Research at the University of Texas.

DCB differential code bias.
DLR German Aerospace Center.

ECMWF European Centre for Medium-Range Weather Forecasts.
EGSIEM European Gravity Service for Improved Emergency Management.
EOF empirical orthogonal functions.
EOP Earth Orientation Parameter.
ESA European Space Agency.
ESM Earth System Model.
ESSP Earth System Science Pathfinder.
EWH equivalent water height.

FTP File Transfer Protocol.

GFZ German Research Centre for Geosciences.
GFZESM GFZ operational Earth System Model.
GIA glacial isostatic adjustment.
GNSS global navigation satellite system.
GOCE Gravity field and steady-state Ocean Circulation Explorer.
GPS Global Positioning System.
GRACE Gravity Recovery and Climate Experiment.
GRACE-FO GRACE Follow-On.

IDFT inverse discrete Fourier transform.
IERS International Earth Rotation and Reference Systems Service.
IGS International GNSS Service.
ISDC Information System and Data Center for geoscientific data.
ITSG Institute of Geodesy, Working Group Theoretical Geodesy and Satellite Geodesy.

JPL Jet Propulsion Laboratory.

KBR K-band ranging instrument.

LOS line-of-sight.
LRI laser ranging interferometer.

ML maximum likelihood.

NASA National Aeronautics and Space Administration.
NRT near real-time.

PC principal component.
PCA principal component analysis.
PPP precise point positioning.
PRN pseudorandom noise number.
PSD power spectral density.

RMS root mean square.
RTS Rauch-Tung-Striebel.

SCA star camera assembly.
SOE sequence of events.
SRF satellite reference frame.
SSL Space Systems/Loral.
SV ID space vehicle identifier.

TWSA total water storage anomalies.

VAR vector-autoregressive.
VCE variance component estimation.
VLBI very long baseline interferometry.

XML Extensible Markup Language.

YW Yule-Walker.

ZKI Center for Satellite based Crisis Information.

List of Figures

List of Tables